Investigating the frictional properties of organic matter and pore structure of organic-rich shales with atomic force microscopy and scanning electron microscopy

by

Farnood Sobhbidari

Dissertation

Submitted in partial fulfillment of the requirements

for the degree of Doctor of Philosophy at

The University of Texas at Arlington

December 2022

Arlington, Texas

Supervising Committee:

Qinhong Hu, Ph.D. (Supervising Professor)

Arne Winguth, Ph.D.

Erika La Plante, Ph.D.

Nathan D. Brown, Ph.D.

Xinbao Yu, Ph.D.

Jiechao Jiang, Ph.D.

Abstract

Investigating the frictional properties of organic matter and pore structure of
organic-rich shales with atomic force microscopy and scanning electron
microscopy

Farnood Sobhbidari, Ph.D

The University of Texas at Arlington, 2022

Supervising Professor: Qinhong Hu

Understanding geomechanical properties of shales, such as stiffness properties and fracture
toughness, is important in different areas of petroleum industry-related activities including
fracturing efficiency, petroleum flow to the wellbores, and induced seismicity. Nanoscale to
microscale experiments on shale samples require a much smaller sample compared to macroscale
experiments. This is a major advantage because irregularly-shaped drill cuttings from shales can
be used for experimental analyses, such as nanoindentation or atomic force microscopy (AFM).
However, a characterization of mechanical properties at the nano- to micro-scale is a relatively
new addition to classical geomechanical experiments on shales, and there is still a lack of both
fundamental knowledge and standard procedures for conducting experiments at this scale. The
frictional behavior is one of the important mechanical properties of organic matter (OM) which is
still not investigated. The first half of this dissertation is focused on understanding the standard
procedures for conducting the experiments in nanoscale and investigating the frictional properties.
For this research I examine the mineralogy of the surface of shale samples using scanning electron
microscopy (SEM) with energy dispersive spectroscopy (EDS), and measuring the friction force

and Young's modulus of OM using AFM. Samples from Bakken shale formation has been used for this project.

The second half of this dissertation is focused on understanding the structure and geometry of pore spaces. Because hydrocarbon is accumulated mainly in the pore spaces of shale, coal, and tight sandstone reservoirs, it is highly crucial to understand the morphology of the pore spaces. For this research I applied SEM imaging and image processing and compared their results with these from AFM imaging of the pore structure. Samples from Bossier shale and Haynesville shale formations has been used for this project. Overall, this dissertation will help to understand the standard procedures of mechanical characterization and the frictional behavior of OM in nanoscale, and determine the 3D structure of pore spaces, of organic-rich shales.

iv

ACKNOWLEDGMENTS

Dedication

This dissertation is dedicated to my parents, my sister, and her husband. Their unfailing support,

encouragement, and love have sustained me throughout my life specially my PhD studies.

Table of Contents

Table of Figures

List of Tables

Chapter 2

Chapter 1: Introduction

Shales (or mudrocks) are the source rock for hydrocarbons in "shale play reservoirs" and are also the caprock in most conventional reservoir. One of the difficulties facing petroleum development in mudrock reservoirs has been the accurate assessment of the host rock's mechanical properties. These properties influence vital reservoir aspects such as borehole stability, fracturing behavior, yield strength and elastic moduli (Dewhurst et al., 2011; Fam et al., 2003), affecting not only fracturing efficiency, but also the petroleum flow to the wellbores. Consequently, an adequate knowledge of the mechanical properties of shales is crucial to the sustainable development of unconventional reservoirs. Shales are among the most complex geological materials, as their composition varies through both time and space and at different scales, from nano- to macro-scopic dimensions (Ilgen et al., 2017). This heterogeneity leads to anisotropy and a range of macroscopic behaviors. Shale is composed from two distinguishable media, inorganic and organic matters, at grain sizes less than 63 μm.

Traditionally, a mechanical characterization of rock has been conducted using uniaxial or triaxial compression tests (Kumar et al., 2017), and laboratory tests or logging tools provide sonic and density data with which to obtain the elastic properties, including Young's modulus and Poisson's ratio (Eissa & Kazi, 1988; Sone & Zoback, 2013). Because of the existing instability of chemical and mechanical properties of shale formations, obtaining a core stable enough to perform traditional geomechanical experiments can be difficult and costly (Liu et al., 2016). However, progress in nanomechanics and nanotechnology has made it possible to investigate the *in situ* mechanical properties of shales at the nano- to micro-scale by nanoindentation using a small sample volume (Liu et al., 2016; Slim et al., 2019; Ulm & Abousleiman, 2006) or PeakForce

QNM^{TM} method (Eliyahu et al., 2015). PeakForce QNM^{TM} is the force mapping mode of atomic force microscopy (AFM). The creep behavior of shale samples at the nanoscale has been studied by gridded nanoindentation (Liu et al., 2018a; Slim et al., 2019) and modulus mapping (Liu et al., 2018b). The possibility of using viscoelastic rheological models to model the creep behavior of shale samples at the nanoscale was also the subject of some previous research (Liu et al., 2018a; Shi et al., 2020). Emmanuel et al. (2016a) extended the previous research of Eliyahu et al. (2015) to investigate the possible impact of thermal maturation on the mechanical properties of OM within shales. Emmanuel et al. (2016b) investigated the potential impact of *in situ* temperature on the mechanical behavior of the OM using PeakForce QNM^{TM} method.

Recent measurements by nanoindentation or AFM on the shale provide evidence of a significant difference in stiffness properties of different composing minerals of shale (Eliyahu et al., 2015; Zhao et al., 2019). Among all the composing parts of shale, OM has the weakest mechanical properties (Eliyahu et al., 2015; Zhao et al., 2019). Although mechanical characterization of OM within shale in nanoscale has been recently the focus of much research, the friction behavior of OM is still unclear. The simulation of mechanical behavior of OM in the nanoscale using molecular simulation has been the subject of some researches. In these papers the failure envelope of kerogen, fracture toughness, and surface energy density of kerogen were the focus of the simulations (Wu and Firoozabadi, 2020a; b).

Another important aspect of unconventional resources is about understanding the structure and geometry of pore spaces. Hydrocarbon is accumulated mainly in the pore spaces of shale, coal, and tight sandstone reservoirs (Clarkson, et al., 2012; Ilgen et al., 2017; Ju et al., 2017), and many works have been conducted to determine and classify pore structure, pore volume ranges, pore surface variation, and other factors (Groen et al., 2003; Li et al., 2014; Zhou et al., 2016; Zhu et

al., 2018). The main methods generally include low temperature nitrogen adsorption (LT-NA) (Chen et al., 2016; Ju et al., 2018; Lu et al., 2004), carbon dioxide adsorption (Chen et al., 2017; Liu, Zhang, Choi, et al., 2018), mercury intrusion porosimetry (MIP) (Cao et al., 2015; Hu et al., 2017; Tao et al., 2018), saturation or imbibition (Kibria et al., 2018; Wang et al., 2021), nuclear magnetic resonance (NMR) (Li et al., 2015), optical microscopy (Li et al., 2017), X-ray computed tomography (X-ray CT) (Cai et al., 2018; Li, Tang, Elsworth, et al., 2014), focused ion beam-scanning electron microscopy (FIB-SEM) (Zhou et al., 2018), and small angle neutron scattering (SANS) and ultra-small angle scattering (USANS) methods (Clarkson et al., 2012; 2013, Zhang et al., 2019). Most of these methods provide either two to three dimensional characterization of the pore structure or a distribution of pore sizes (Ougier-Simonin et al., 2016). Some of the disadvantages of these methods are as follows: 1) The three-dimensional pore reconstruction methods (X-ray CT, FIB-SEM) are very expensive; and 2) the fluid intrusion methods (LT-NA and MIP) may damage the structure of samples and have different measuring ranges (Zhu et al., 2017). Therefore, it is highly crucial to combine different methods to characterize the pore structure and surfaces (Li et al., 2019).

Atomic force microscopy (AFM) can measure the surface topography and mechanical properties such as Young's modulus and other structural properties (Zhang et al., 2012). AFM has been a popular instrument in many fields including material science (Beuwer et al., 2016; Kim et al., 2018; Li et al., 2016), molecular biology (Dufrêne et al., 2017; Guo et al., 2004; Li et al., 2017; Rief et al., 1997), and electrochemistry (Ghorbal et al., 2013; Zhang et al., 2012). AFM has also been used in studies to image the surface topography of super-fine and pulverized coal grains (Liu et al., 2010), the nanopore development and surface roughness of naturally matured coal (Jiao et al., 2018), the efficiency and correctness of Threshold and Watershed methods were investigated

on the recorded AFM images of surface topography on coal and shale samples (Zhao et al., 2019). AFM and LT-NA were used to characterize the surface property and pore structure of shales, and the double-threshold discrete integration method was introduced to measure the porosity (Chen et al., 2021). AFM can record an image of pore structures in 3D without destroying the sample, so the samples can be used for experimental measurements with other methods (Rief et al., 1997). Considering these advantages, there are a few published research about using AFM in understanding the pore structures of shales (Javadpour et al., 2012; Zhao et al., 2019).

In this work, both AFM and SEM were used to identify pores and their geometrical properties. Statistical analyses were conducted on the pore geometrical properties. In addition, the obtained data from AFM and SEM were compared with the results from other methods to verify the recorded pore geometrical properties from AFM and SEM.

Chapter 2:

Literature review

Most of this chapter was published in the following article:

Recent advances in the mechanical characterization of shales at nano-to micro-scales: A review

Farnood Sobhbidari[1], Qinhong Hu[1*]

[1]Department of Earth and Environmental Sciences, The University of Texas at Arlington, 500 Yates Street, Arlington, TX 76019, USA

Published at:

Mechanics of Materials

[*]Corresponding author: maxhu@uta.edu

2.1 Mechanical characterization of OM-rich shales in nanoscale to macroscale

Given recent advancements in measureing the mechanical properties of OM-rich shales from the nanoscale to microscale, and the lack of detailed review on these advancements, we compile and review here relevant studies to identify non-traditional methods for the mechanical characterization of shale at these very small scales. Three main methods to identify the mechanical properties in the nanoscale are as follows: 1) Gridded nanoindentation, 2) Modulus mapping, and 3) Atomic Force Microscopy.

2.1.1 Application of nanoindentation-based methods

The nanoindentation method is used to measure mechanical properties such as stiffness and hardness of materials at the nano-to micro-scale. Nanoindentation has been used in material science research on various materials such as fibers, thin films, concrete, and bones (Ago et al., 2013; Constantinides et al., 2006; Schwiedrzik et al., 2014). Table 2.1a represents the experimental properties of nanoindentation testing (gridded-nanoindentation and modulus mapping) applications by different researchers to investigate the mechanical behavior of OM-rich shales. Limitations in their experimental techniques are specifically mentioned; Table 2.1b is just the continuation of Table 2.1a.

2.1.1.1 Gridded nanoindentation

Ulm and Abousleiman (2006) investigated a possible connection between the mineralogy of clay particles and their mechanical properties. Shale specimens were cored in three perpendicular directions. The sample's roughness was measured using AFM (described in Chapter 3), and the mineral compositions of samples were determined using X-ray diffraction (XRD) measurements. The authors calculated the clay packing density (η) by measuring the total porosity

(φ) of the shale cuttings (Eq. 11 in Ulm and Abousleiman, 2006). The authors then compared the results from gridded nanoindentation with the results of the dynamic ultra-pulse-velocity (UPV) measurements of the overall composite stiffness of shales.

Comparison between results from gridded nanoindentation and UPV measurements showed four important reasons for anisotropy of shales at the macroscopic scale (Ulm and Abousleiman, 2006): (1) one order-of-magnitude difference between the previously measured stiffness values of clay minerals and the measured elasticity content of the clay fabric at the scale of hundreds of nanometer to millimeters, 2) the identification of the relationship between the characteristic stiffness and packing density for scales beyond a few hundreds of nanometers (the observation scale), these relationships are insensitive to the varying mineralogy of the tested shale samples, (3) a clay packing density of $\eta \sim 0.5$ as a percolation threshold of the elasticity of the clay composite (the matrix in the shales is composed of the clay composite), and (4) a direct correlation between the clay packing density and the degree of anisotropy.

Table 2.1a. Experimental properties of nanoindentation-based testing on organic-rich shales

Experimental Properties	Ulm and Abousleiman (2006)	Bennett et al. (2015)	Wilkinson et al. (2015)	Abousleiman et al. (2016)	Liu et al. (2016)
Shale & locations	n/a	Woodford, USA	Bakken, USA	Woodford, USA	Bakken, USA
Coring depths (m)	n/a	33-60	Sample 1: 2195, Sample 2: 2134	n/a	n/a
Coring Orientation to bedding	n/a	Parallel and Perpendicular	n/a	n/a	Parallel
Shape and no. of samples	Cylindrical, 3	n/a	2	n/a	Irregular, 4
Avg. sample dimensions (cm)	n/a	n/a	n/a	1	n/a
Sample thickness (mm)	5-10	n/a	n/a	4	n/a
Sample surface roughness (μm)	0.09	n/a	Sample 1: 0.01, Sample 2: 0.002	n/a	n/a
Indenter tip diameter (nm)	n/a	n/a	Tip 1: 1180, Tip 2: 170	5000 and 10000	n/a
Depth of penetration (μm)	0.2-0.3	0.2, 1, 3, and 5	n/a	n/a	n/a
Maximum peak load (μN)	236-266	n/a	-	n/a	n/a

Quasistatic force[1] (μN)	-	-	2 for both samples	-	-
Dynamic force[1] (μN)	-	-	Sample 1: 1, Sample 2: 0.5 With frequency of 200 Hz	-	-
Hold time for peak load (sec)	n/a	60	n/a	n/a	n/a
Time to load (sec)	n/a	n/a	n/a	n/a	n/a
Assumed sample Poisson's ratio	n/a	n/a	n/a	n/a	n/a
Loading rate: (nm/sec) for displacement controlled mode, ($\mu N/sec$) for force controlled mode	n/a	n/a	n/a	15 (nm/sec)	20
Grit sizes used	n/a	400, 600, 1500	n/a	Up to 4000 and 1 μm diamond grit	600 to 1200 and 5, 3, and 1 μm diamond grit
Porosity (%)	Sample 1: 37.3, Sample 2: 23.7, Sample 3: 13.9	n/a	n/a	n/a (16-19)	n/a
Avg. TOC (wt %)	n/a	n/a	Sample 1: 16, Sample 1: 14	n/a	n/a

Dominant minerals	Clay minerals	n/a	n/a	Quartz and Clay minerals (Illite)	Quartz, Feldspar and Clay minerals
Temperature conditions (°C)	n/a	n/a	n/a	n/a	Ambient
Impact on geomechanical properties	Anisotropy, Clay packing density	Anisotropy	Polishing	Impact of OM on tensile strength	Mineral content, and Porosity
Remarks	First application of gridded nanoindentation	Comparison with FEM simulations, study of mechanical properties of both single mineral phase and composite phase	First application of modulus mapping	Experiment setup was positioned inside SEM	Measuring fracture toughness from nanoindentation
limitations		Not consider the geochemical characterization of OM and characterizing OM types (kerogen, bitumen, etc.)	Neglecting the impact of anisotropy	Not consider the possible impact of different OM types on tensile strength	Neglecting the impact of anisotropy

Quasistatic force and dynamic force are related to modulus mapping (Nano-DMA)

Table 2.1b. Experimental properties of nanoindentation-based testing on organic-rich shales

Experimental Properties	Zargari et al. (2016)	Liu et al. (2018a)	Liu et al. (2018)	Slim et al. (2019)	Zhao et al. (2019)	Shi et al. (2020)
Shale & locations	Bakken, USA	Bakken, USA	Bakken, USA	Marcellus, Haynesville, Antrim, Barnett and Woodford, in USA	Yanchang, China	Longmaxi, China
Coring depths (m)	n/a	n/a	n/a	Woodford sample is an outcrop	n/a	n/a
Coring Orientation to bedding	n/a	Perpendicular	Perpendicular	Parallel and Perpendicular	Parallel and Perpendicular	n/a
Shape and no. of samples	Cubic, 4	Irregular, n/a	Irregular, 4	n/a	Cube, 7	2
Avg. sample dimensions (cm)	1	n/a	n/a	n/a	1	0.5-1
Sample thickness (mm)	10	n/a	n/a	5-15	5	n/a
Sample surface roughness (μm)	n/a	<0.2	n/a	0.030-0.150	<0.1	<0.07
Indenter tip diameter (nm)	160	n/a	n/a	n/a	n/a	n/a

Depth of penetration (μm)	n/a	n/a	n/a	n/a	Microindentation: 4	n/a
Maximum peak load (μN)	-	-	n/a	4800	Nanoindentation 3000 for minerals, 1000 for OM	350000
Quasistatic force[1] (μN)	2	n/a	-	-	2	-
Dynamic force[1] (μN)	1 with frequency of 200 Hz	n/a	-	-	1	-
Hold time for peak load (sec)	n/a	60	5 to 180	180	2	0, 15, 60, 120, and 220
Time to load (sec)	n/a	n/a	n/a	10	10	n/a
Assumed sample Poisson's ratio	n/a	n/a	n/a	n/a	n/a	0.25
Loading rate: (nm/sec) for displacement controlled mode, ($\mu N/sec$) for force controlled mode	n/a	n/a	n/a	480 ($\mu N/sec$) Force-controlled nanoindentation	300 ($\mu N/sec$) for minerals, 100 ($\mu N/sec$) for OM Force-controlled nanoindentation	n/a

Grit sizes used	n/a	n/a	80 to 1200	400, oil-based diamond suspension, aluminum oxide abrasive disks (grain size between 9 and 1 μm)	n/a	600 to 1200, and diamond polisher with grain sizes of 5, 3 and 1 μm
Porosity (%)	3.7 to 6.9	n/a	n/a	Marcellus: 5.9-8.4, Haynesville: 6-7.6, Antrim: 8.8, Barnett: 7.3, Woodford: 12.6	n/a	n/a
Avg. TOC (wt %)	7.9 to 21.7	n/a	n/a	Marcellus: 0.5-8.18, Haynesville: 2.6-3.3, Antrim: 9.6, Barnett: 12.2, Woodford: 4.2	8.68 to 13.27	2.37-6.51
Dominant minerals	n/a	n/a	Quartz, feldspar, and clay minerals	Quartz and clay minerals	Quartz, feldspar, and clay minerals	Quartz and clay minerals
Temperature conditions (°C)	Ambient	n/a	n/a	Ambient	n/a	Ambient
Impact on geomechanical properties	Maturity, Porosity	Mineral content	Creep time, mineral content	Anisotropy, mineral content, OM	Anisotropy, mineral content,	Creep time, Creep rheological models
Remarks		Nano-DMA can investigate creep		Wide variety of samples	Comparison between gridded nanoindentation and modulus mapping	Compare three different rheological models

| Limitations | Neglecting the impact of anisotropy | Not consider the geochemical characterization of OM and characterizing OM types, Neglecting the impact of anisotropy | Not consider the geochemical characterization of OM and characterizing OM types, Neglecting the impact of anisotropy | Characterizing OM types | Not consider the geochemical characterization of OM and characterizing OM types | Not consider the geochemical characterization of OM and characterizing OM types, Neglecting the impact of anisotropy |

Quasistatic force and dynamic force are related to modulus mapping (Nano-DMA)

Bennett et al. (2015) coupled nanoindentation experiments with high-resolution imaging techniques and simulated the heterogeneous scaled nanoindentation experiments using nonlinear finite element modeling (FEM). The indentation depth in these experiments were from 200 nm to 5 µm. The shallow indentation measured the homogeneous regions that contained a single mineral phase, while the larger indentations measured a composite deformation behavior. The specimens were made from the same sample, but the cutting direction was in two formats: bedding plane normal (BPN) and bedding plane parallel (BPP). The existing anisotropy of material properties was measured by conducting nanoindentations in directions both normal to the bedding plane (BPN) and parallel to it (BPP). Bennet et al. (2015) observed a significant creep in addition to plastic deformation in their nanoindentation experiments, so they applied a viscoplastic creep material for their FEM simulations. This constitutive model was specifically isotropic linear elasticity and a modified Drucker-Prager/Cap plasticity, and it was combined with the consolidation hardening and creep. This constitutive model provides an inelastic hardening mechanism to model the plastic compaction such as the consolidation of geological materials (Resende and Martin, 1985). For more information about this constitutive model readers are referred to Resende and Martin (1985) as well as Liu and Borja (2013). The actual data from the nanoindentation experiments were used to calibrate the Drucker-Prager/Cap plasticity and consolidation creep material parameters. To understand the difference between the constitutive model parameters derived from BPN and BPP experiments, a triaxial compression test was simulated using those calibrated parameters.

From the above investigation approaches, Bennett et al. (2015) found three main mechanical phases, namely quartz-feldspar-pyrite (QFP), clays, and OM, from the shallow depth (200 nm) nanoindentation experiments. The FEM simulations of the triaxial compression test

revealed anisotropic behavior of shale, that corresponds to the difference between the BPP and BPN calibrated constitutive model properties in the ductile stress-strain response. According to the authors, FEM simulations based on the completely isotropic material model showed that development of a finite strain anisotropic material model is necessary for shale at the nano- to micro-scales.

Abousleiman et al. (2016) focused on the failure analysis of OM-rich shales, and the possible impact of OM on the tensile and compressional strength at the nano- to micro-scales. They milled four micro-beams and three micro-pillars for their indentation experiments, and these samples were manufactured using the S.G. Roberts method (Di Maio & Roberts, 2005; Frazer et al., 2015). All the nanoindentation experiments were conducted inside a high-resolution SEM instrument, to provide a simultaneous monitoring of the indentation experiments until failure. The indenter tip was placed at the end of the free side of the micro-beams (Figure 2.1), and the indentation experiments on the micro pillars were conducted to model the conventional unconfined compressional test at the nanoscale (Figure 2.1). Moreover, a numerical simulation of the same experimental configurations was constructed to theoretically investigate the observed failure behaviors. The indentation experiments in Abousleiman et al. (2016) showed that the OM "glues together" other components of the shale, and it has a high modulus of toughness. In the work of Abousleiman et al. (2016), the OM-rich shales were directly loaded under tensile forces, but the classical macroscale experiments of tensile behavior did not measure or isolate the tensile strength directly.

Liu et al. (2018b) continued research by Liu et al. (2018a) and focused on the application of gridded nanoindentation (Constantinides et al., 2006) to understand the creep behavior of OM-rich shales. The holding phase of the nanoindentation was set to be 20s, 50s, 100s, and 180s. To

find the best creep curve that fits the recorded data (indentation depth vs. creep time), Burger's model was applied. This is one of several rheological models for investigating the creep behavior (Ashraf and Tian, 2016; Cornet, 2015). The impact of various existing minerals on the creep behavior and mechanical properties (Young's modulus, hardness, and fracture toughness) was studied using bivariate plots from partial least-squares regression (PLS) (Table 6 in Liu et al., 2018b). Based on this analysis, it was found that a change in the clays content has the greatest effect on the mechanical properties. The increase in clay minerals content leads to an increase in changes to the Young's modulus and hardness, but the change of fracture toughness is reduced. They applied the energy analysis method (Cheng et al., 2002; Liu et al., 2016) to calculate the fracture toughness value for each sample. It was shown that as the creep time increases, the fracture toughness decreases.
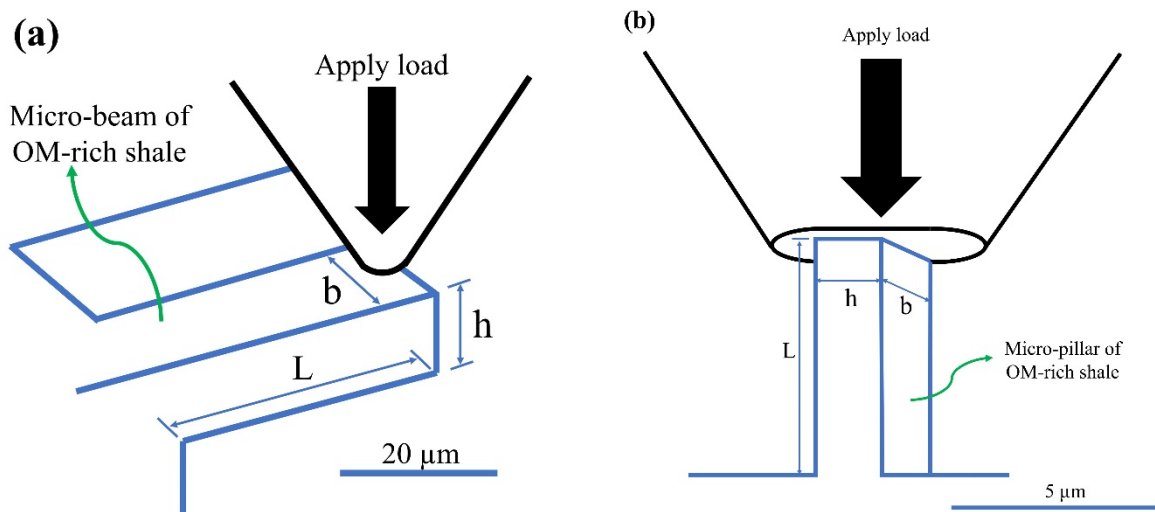
Figure 2.1. Schematic of the nanoindenter applying a load on (a) micro-beam and (b) micro-pillar of OM-rich shales, with nanoindenter positioned at the end of the micro-beam (a) or on top of the micro-pillar (b).

Slim et al. (2019) investigated the potential effect of OM on the creep behavior of a source rock using both experimental and modeling methods. A wide variety of shales in the US, including Marcellus, Haynesville, Antrim, Barnett, and Woodford, was investigated. Based on the data from Rock-Eval pyrolysis, Haynesville shale samples are mature (vitrinite reflectance equivalent of 2.5%), but Woodford, Barnett, and Antrim Shale samples are immature source rocks. Moreover, the Marcellus Shale samples are overmature source rocks (vitrinite reflectance equivalent of 3%). A mechanical test and chemical analysis were also conducted on pyrobitumen-rich samples to understand the creep properties of mature OM. A grid indentation technique (Constantinides et al., 2006; Ulm et al., 2007) was applied, given the heterogeneity of the shale samples. Slim et al. (2019) identified four mechanical phases within the shale sample and reported that these mechanical phases are based on the similarity in mechanical strength or stiffness properties. The shale components whose mechanical strength or stiffness properties are in the same range, and are also categorized in the same mechanical phase. The four mechanical phases are: 1) OM-rich phase, 2) a porous OM phase with inorganic impurities, 3) a mixed phase (containing pyrite), and 4) an inclusion (quartz) phase (Figures 5-6 in Slim et al. 2019). Of these four identified phases, the highly porous organic-rich phase has the lowest values of M, H, and C, and an inclusion phase has the highest values of M, H, and C (Figures 5 in Slim et al., 2019). M and H are indentation modulus and indentation hardness, respectively. C is the contact creep modulus (Vandamme and Ulm, 2013) (more detailed information about C is referred to Vandamme & Ulm, 2013). The OM makes the greatest contribution to the creep behavior of the shale, but the inorganic phases surrounding OM reduce the creep rate. A comparison of the results from micro-indentation tests with first-order creep homogenization modeling shows that two asymptotes exist for the relevant creep rate of OM-rich shales: (1) a continuous matrix of immature OM with rigid clay inclusions defines the

lower end-member; (2) a self-consistent pattern representing mature disordered systems defines an upper end-member.

Zhao et al. (2019) investigated compositional heterogeneity and anisotropy of shales using the mechanical characterization method (nanoindentation and modulus mapping) at three (mineral, core, and well) scales. Seven terrestrial shale samples from the Yanchang formation in China were chosen. Nanoindentation and modulus mapping were applied to investigate the compositional heterogeneity and anisotropy, respectively, at the mineral scale. The Young's modulus and hardness of non-clay minerals were determined by nanoindentation; to study anisotropy, the mechanical properties of clays in two directions were measured with modulus mapping. Micro-indentation was performed to verify the prediction of the upscaling method, which was proposed to predict the macroscopic characteristics of organic-rich shale from the mineral scale properties. Both micro-indentation and nanoindentation were based on the same theories, and the difference was just in the scale of these experiments. The upscaling method was based on both the Mori-Tanaka and Self-Consistent schemes. The well scale mechanical characterization was based on the Brittleness Index (BI), newly proposed by Zhao et al. (2019) which is a function of the mineral composition, and its application to interpretation of well logs.

Shi et al. (2020) conducted gridded nanoindentations on 6×6 grids of the nanoindentation map with 15 μm as the distance between two neighboring nanoindentations. They chose two shale samples from the upper Ordovician to Silurian Longmaxi black shale, Sichuan Basin, China for gridded nanoindentation experiments. The holding phase of the nanoindentation was set to 0 s, 15 s, 60 s, 120 s, and 220 s. Shi et al. (2020) used three different viscoelastic rheological models, namely the i) three-element Voigt, ii) Burgers, and iii) two-dashpot Kelvin models. These three models were fitted with the depth-time curve during the nanoindentation holding phase. Detailed

explanation and formulation of these three rheological models are referred to Cornet (2015), Ashraf and Tian (2016), and Shi et al. (2020).

2.1.1.2 Modulus mapping application

Wilkinson et al. (2015) introduced an elastic modulus mapping technique, using spatially continuous dynamic nanoindentation. Two shale samples from the Bakken Formation in the Williston Basin, North Dakota were used. The samples were sectioned and polished using a focused gallium ion beam. These two samples were polished differently to investigate the impact of sample preparation on the resultant stiffness data and mechanical characterization of samples by dynamic nanoindentation.

The modulus map, surface topography and displacement amplitude of each sample were presented in Wilkinson et al. (2015). There are two important issues with the modulus maps: (1) The ion tracks are presented as the change of modulus within a relatively mineralogically homogeneous region. Moreover, the surface height is changed drastically because the softer material can be removed to a greater extent than the harder minerals; these local changes in topography can lead to an under- or over-estimation of contact area between the sample surface and the tip; and (2) The displacement amplitude in the stiff minerals (mainly pyrite) can be lower than the detection limit of the instrument. Therefore, the system counts them as noise which can result in erroneous values for the modulus. Comparison of the results of both shale samples shows that the sample preparation (polishing method) has a direct impact on the recorded modulus maps. The importance of this research lies in its investigation of the possible effect of large surface height variations, and low displacement amplitudes on the results of modulus mapping.

Using a coupled method of nano-DMA and gridded nanoindentation, Liu et al. (2018a) concentrated on the time-dependent mechanical behavior of shales. Based on the recorded complex modulus and hardness values, they selected three points on the gridded nanoindentation area to represent soft minerals, minerals with medium strength, and hard minerals, respectively. Based on the plotted creep displacement vs. time for these three points (Figure 8 in Liu et al., 2018a), the displacement in all selected points abruptly increased at the beginning of the creep and then slowed down. Furthermore, this figure showed that the material with a greater hardness and more complex modulus has the lower creep displacement.

Liu et al. (2018a) also measured the average value of creep displacements, loss modulus, storage modulus and hardness in the entire nanoindentation area. These average values were measured for each time (during the creep experiment) to understand the overall creep behavior in the entire gridded areas. Average creep displacement has the same behavior through time at three selected points. The curve fitting analyses on creep displacement, loss modulus, storage modulus and hardness showed a logarithmic pattern. The groups of soft and hard minerals are distinguishable from the resultant histogram of storage modulus map from the deconvolution method. The calculated volumetric fraction of soft minerals increased throughout the creep experiment (see Table 6 in Liu et al., 2018a), but the fraction of hard minerals decreased as times passed. These authors provided two possible scenarios for this behavior: i) the impact of dislocation creep; and ii) the movement of hard minerals under the soft minerals close to the sample surface.

2.1.1.3. Summary of applying nanoindentation-based methods onto OM-rich shales

Ulm and Abousleiman (2006) found the linear relationship between the measured indentation modulus (for both nanoindentation normal to the bedding planes and parallel to the

bedding planes) and clay packing density for clay packing densities greater than 0.5. The difference between measured indentation modulus for nanoindentations normal to the bedding planes and nanoindentations parallel to the bedding planes becomes larger when the clay packing density approaches 1. These findings shows that the main source of existing anisotropy of shale elasticity parameters is related to the depositional structure of the clay grains. The capability of nanoindentation to measure the fracture toughness in OM-rich shales was studied by Liu et al. (2016). Their main focus was to find the relationship between the measured Young's modulus and fracture toughness. It is possible to investigate the capability of nanoindentation on measuring the fracture toughness of OM, which is the most compliant compound of OM-rich shales comparing to other constituent minerals of shales.

The impact of bedding on the stiffness measurements and its anisotropy was studied by Bennett et al. (2015), Li et al. (2019), and Slim et al. (2019). Table 2.2 shows the results of measured mechanical properties of nanoindentations at two different depths (200 nm and 1 µm) from Bennett et al. (2015). Both the effective modulus (E_S) and indentation hardness (H) of the QFP are higher when measured parallel with the bedding planes than the normal to the bedding planes. For clays and O/C (composite of organic and clays) matrices, the effective modulus parallel with the bedding plane is higher than that normal to the bedding planes, but the indentation hardness normal to the bedding is higher than that parallel with the bedding plane. It is important to mention that Bennet et al. (2015) observed four constituent compounds in their shale samples including clay particles, QFP, OM, and O/C. In the O/C compound the clay particles and organic matter were mixed without forming a supporting skeleton with inter-granular contacts. The OM has the highest anisotropy ratio, while clays and QFP are second and third, respectively. Slim et al. (2019) found that the creep rate of source rocks is mostly isotropic while their elastic properties

show anisotropic behavior. According to Slim et al. (2019), isotropic constituents, pores, and OM are the important parameters in the isotropic creep behavior of organic-rich shales.

Table 2.2. Results of nanoindentations in two different depth (200 nm and 1 μm) from Bennett et al. (2015). The specimen was made from the same sample, but the cutting direction was in two directions: bedding plane normal (BPN) and bedding plane parallel (BPP). $K_{(.)}$ is the anisotropy ratio of the mechanical property (.), which can be E_S (effective modulus), H (hardness).

	BPN	BPP	$K_{(.)} \left(K_{(.)} := \frac{(.)_{BPP}}{(.)_{BPN}} \right)$		BPN	BPP	$K_{(.)} \left(K_{(.)} := \frac{(.)_{BPP}}{(.)_{BPN}} \right)$
			Indentation depth = 200 nm				
QFP				Clays			
E_S (GPa)	32.750	38.114	1.16	E_S (GPa)	20.373	25.865	1.27
H (GPa)	4.515	4.815	1.07	H (GPa)	1.801	1.592	0.88
	Indentation depth = 200 nm				Indentation depth = 1 μm		
Organic matter				O/C matrix			
E_S (GPa)	8.780	6.503	0.74	E_S (GPa)	12.392	18.545	1.50
H (GPa)	0.449	0.278	0.62	H (GPa)	0.604	0.592	0.98

The impact of OM maturity on the stiffness measurements using modulus mapping was studied by Zargari et al. (2016). They found that as OM maturity increased, the moduli of the kerogen were lower. It was mentioned that OM with higher maturity has an abundant nano porosity and concluded that the intraparticle OM porosity has a crucial impact on its modulus.

Shi et al. (2020) investigated the creep behavior of OM-rich shales using gridded nanoindentation coupled with three rheological models of creep. A creep time constant was

derived from each of the rheological models, and the regression precision of these three models for shale creep was compared. Even though the two-dashpot Kelvin model had the highest standard deviation, it provided better regression results than the three-element Voigt and Burgers models. As Slim et al. (2019) found that the OM has the greatest contribution to the creep behavior of the shale, it is important to investigate the creep behavior of OM more in detail such as investigating whether or not different types of OM have different creep behavior or not, or investigate the relationship between the maturity and creep behavior of OM. Reviewing most of the published research about the application of nanoindentation in the mechanical characterization of OM-rich shales showed that most of them are lacking in identifying the types of OM (kerogen, bitumen, etc.), and finding the possible relationship between the OM type and mechanical properties such as Young's modulus and creep rate is difficult. Due to the small scale of the indentation depth, a gridded nanoindentation is not capable of identifying the possible impact of some internal structures of OM-rich shales, such as natural fractures and large pores. Therefore, to understand the possible impact of natural fractures and large pores, it is necessary to combine gridded nanoindentation with a good upscaling method to find the homogenized values of mechanical properties (Young's modulus, hardness, etc.). Moreover, it is necessary to compare the upscaled mechanical properties with the results of conventional rock mechanics tests on the same type of samples.

2.1.2 Application of AFM-based methods

Table 3 lists a summary of literature studies for AFM work in shales by focusing on mechanical characterization in the nanoscale. Eliyahu et al. (2015) used the new AFM method (PeakForce QNM^{TM}, as described above) to map the modulus values of three samples from an

Upper Jurassic source rock in the USA. The TOC of their samples ranged from 0.5 to 4.5 wt.%, and their thermal maturity was very high (vitrinite reflectance ~2.1 %R_o).

The scan area was changed from $5 \, \mu m \times 5 \, \mu m$ to $50 \, \mu m \times 50 \, \mu m$, and the values of modulus exhibited the same pattern and distribution in all of these different scan sizes, and clays and quartz grains had modulus values of approximately 30 GPa and 60 GPa, respectively. Furthermore, the map at highest resolution showed that the modulus values of the OM was in the range 0-25 GPa; more importantly, there were two distinct peaks in the distribution of the modulus values for the OM. This led to the conclusion that the OM probably constitutes two distinct types.

Table 2.3. Experimental properties of AFM-based testing on organic-rich shales

Experimental properties	Eliyahu et al. (2015)	Emmanuel et al. (2016a)	Emmanuel et al. (2016b)	Li et al. (2018b)
Shale & locations	n/a	n/a	n/a	Bakken, USA
Coring depths (m)	n/a	n/a	n/a	2500-3300
Coring Orientation to bedding	n/a	n/a	n/a	Parallel
Shape and no. of samples	n/a, 3	n/a, 6	n/a, 2	n/a, 4
Avg. sample dimensions (cm)	n/a	n/a	n/a	n/a
Sample thickness (mm)	n/a	n/a	n/a	n/a
Sample surface roughness (μm)	n/a	n/a	n/a	0.340
AFM probe tip diameter (nm)	40	8-12	8-12	n/a
Probe normal spring constant ($N\,m^{-1}$)	650	200	200	200

Assumed sample Poisson's ratio	0.3	0.4	0.4	0.2-0.5
Grit sizes used	n/a	n/a	n/a	1200 and 3000
Porosity (%)	4.7-10.9	n/a	n/a	n/a
Avg. TOC (wt %)	0.52-4.56	0.76-11.21	3.23-6.42	9.04-16.3
Dominant minerals	Quartz, Clay Minerals	Quartz, carbonate Minerals	Quartz, carbonate Minerals	Quartz, clay Minerals
Temperature (°C)	Ambient	Ambient	25-225	n/a
Impact on geomechanical properties	Poisson's ratio	Thermal maturity	Temperature	Poisson's ratio, Thermal maturity
Remarks	First application of PeakForce QNM™ on OM-rich shales		Impact of reservoir temperature on stiffness of OM (both kerogen and bitumen)	
Limitations	Neglecting the impact of anisotropy, Characterizing OM types (kerogen, bitumen, etc.)	Neglecting the impact of anisotropy	Neglecting the impact of anisotropy	Neglecting the impact of anisotropy, Characterizing OM types (kerogen, bitumen, etc.)

Emmanuel et al. (2016a) investigated the impact of thermal maturation on mechanical properties (stiffness) of OM at the nanoscale, using six OM-rich shale samples with three different levels of thermal maturity ($\%R_o = 0.40, 0.82, 1.25$) (Table 1 in Emmanuel et al., 2016a), which corresponds to immature to early dry gas window. The samples were from a Cretaceous carbonate-rich source rock from the southern USA. The bulk mineralogy and OM chemical properties were evaluated by standard point-count methods used in organic petrology, Rock-Eval pyrolysis, and XRD. After polishing the samples, an Environmental Scanning Electron Microscopy (ESEM) was used to identify areas tcontaining an OM particle. Based on the morphological criterion that was introduced by Loucks and Reed (2014), bitumen is the OM that existed inside the fossil body-cavities, or the OM that existed within the voids that had been partially surrounded by mineral cementation. Moreover, the other type of OM was identified as kerogen. Emmanuel et al. (2016a) used Loucks and Reed (2014) morphological criteria to differentiate between different types of OM. AFM scans were conducted using the PeakForce QNM^{TM} method to map the stiffness of the areas of interest (Eliyahu et al., 2015). Finally, the energy dispersive spectroscopy (EDS) detector was used to image and map the chemical elements of the sample surface. Emmanuel et al. (2016a) assumed the Poisson's ratio value of 0.4 for organic matter. The Young's modulus of kerogen was found to be in the range of 3.2-29.9 GPa (Table 2 in Emmanuel et al., 2016a), which was in good agreement with the results in previously published papers such as Kumar (2012) and Eliyahu et al. (2015). The measured reduced moduli of bitumen did not have the same trend as the reduced moduli of kerogen as function of maturity, and it was relatively uniform from low to high maturity. The average measured reduced modulus of bitumen at medium and high maturity levels are 8.7 GPa, and 9.8 GPa, respectively, in a good agreement with the published values of Young's modulus values for bitumen of 5-10 GPa (Eliyahu et al., 2015; Zargari et al., 2013).

Yang et al. (2017) introduced an application of AFM-based infrared spectroscopy (AFM-IR) to measure the mechanical and chemical heterogeneity of OM in shale at the nanoscale. AFM-IR is a novel technique in life and materials sciences, and it generates both chemical mapping and mechanical stiffness mapping at nanoscale, in addition to the surface topography image from AFM (Dazzi et al., 2010, 2012; Khanikaev et al., 2016; Qin et al., 2016). The work of Yang et al. (2017) was the first application of AFM-IR to the nanoscale characterization of shales. A series of different samples were prepared with different maturities using laboratory hydrous pyrolysis, and these samples were subjected to the same AFM-IR analyses to understand the possible effect of maturation on mechanical and chemical properties of OM.

AFM-IR works as follows: an AFM probe is placed in contact with an area of interest on a surface. The tip radius should be smaller than 25 nm. At the same time, the area is irradiated with a tunable IR laser (Dazzi et al., 2012). The sample thermally expands as a result of conversion of the energy of absorbed photons to heat. This expansion happens when the laser wavelength reaches the infrared absorption spectrum of the sample. This thermal expansion makes the AFM cantilever oscillate. The oscillation amplitude is a direct function of the local IR absorption coefficient at the IR wavelength where the sample starts to irradiate. As the cantilever and tip stay in contact with the sample surface, the contact resonance (CR) frequency of the sample and AFM cantilever is directly related to the sample's mechanical modulus (Dazzi et al., 2010, 2012; Dazzi & Prater, 2017). This relationship between the CR frequency and sample stiffness, which comes from the connection between the AFM cantilever oscillation amplitude and frequency, allows the mapping of IR absorption and stiffness simultaneously at a fixed laser wavelength.

Yang et al. (2017) analyzed a distribution of measured CR frequencies on different types of organic macerals (inertinite, solid bitumen, and tasmanite). These macerals were also identified

in stiffness images. Figure 3 and Table 2 in Yang et al. (2017) provide information on these constituents' mechanical properties. According to this table, the average CR frequency of inertinite is 182.1 kHz ± 1.7 kHz, and the resulting average CR frequencies of solid bitumen and tasmanite are 178.8 kHz ± 3.6 kHz and 177.2 kHz ± 4.3 kHz, respectively. The spatial resolution of mechanical and chemical maps of the macerals from AFM-IR method are orders-of-magnitude smaller than the regular diffraction-limited IR microscopy (Yang et al., 2017). Combined geochemical and geomechanical analyses of macerals also demonstrated that the mechanical properties of macerals, mainly their stiffness, are a function of their chemical composition. The maceral enriched in aromatic carbon (inertinite) is relatively stronger and has a relatively higher mechanical stiffness than bitumen or tasmanite.

Li et al. (2018b) used PeakForce QNM^{TM} to measure the mechanical property (mainly stiffness) of the OM-rich shales within shale samples from Bakken formation. They found three distinct mechanical phases including a) a soft phase with a modulus of $< 25 GPa$, b) a medium strength phase (modulus of $25 - 50\ GPa$), which is an intergranular matrix phase, c) a stiff phase, which is inorganic and mainly isolated grains with a stiffness of $50 - 100\ GPa$.

Poisson's ratio is highly important to the measurement of Young's modulus in the PeakForce QNM^{TM} method. There are little data on the Poisson's ratio of OM (Ahmadov, 2011; Eliyahu et al., 2015); therefore, the possible effect of a change in Poisson's ratio (0.2-0.5) on the Young's modulus was studied in Li et al. (2018b). They found that a change in Poisson's ratio can lead to 4-25% difference between Young's modulus and reduced modulus values, and this is in agreement with the finding of Eliyahu et al. (2015), who noted an uncertainty of up to 12% in the calculated Young's modulus of OM.

Tian et al. (2018) coupled X-ray photoelectron spectroscopy (XPS), Fourier transform infrared spectroscopy (FTIR) and AFM to understand the relationship between the chemical composition and adhesion force of OM. The measured adhesion forces of OM within the lacustrine and marine shale samples were $100.86 \pm 5\,\mu N$ and $94.28 \pm 4.7\,\mu N$, respectively. Their measurements showed that the OM in both continental shales and marine shales has a significantly higher adhesion force compared to inorganic components within the shale. They did not observe a significant change in the measured adhesion force when the preloading force was changed. Based on their results from XPS and FTIR, they suggested that the C=C and C=O bonds are the reasons for the large dipole on the OM surface. Tian et al. (2019) extended the work of Tian et al. (2018) to clay minerals in the shale and compared the adhesion force and the existing chemical bonds in kerogen and clay minerals. The results from FTIR and XPS analysis of kerogen and clay minerals showed that the chemical bonds on the kerogen surface were O−H, C−C, C−O, pyrrolic, while the chemical bonds on the surface of illite were mainly Si−O and Al−O. The adhesion forces of other minerals such as calcite, montmorillonite and muscovite were $23.8 \pm 11.8, 33.7 \pm 6.28,$ and $105.1 \pm 9.1\,nN$, respectively. Tian et al. (2020) treated the surface of shales with carbonic acid and investigated the impact of this treatment on the mechanical properties using SEM/EDS, AFM and nanoindentation. The measured adhesion force of the nanoindentation experiments revealed that the carbonic acid treatment made the samples more ductile, because the brittle carbonate minerals were highly prone to an acidic treatment.

Figure 2.2 shows the experimentally measured Young's modulus for different components of shale from published research (Simmons and Wang, 1971; Castagna et al., 1985; Han et al., 1986; Wang et al., 2001; Mavko et al., 2009; Kumar et al., 2012; Eliyahu et al., 2015; Wilkinson et al., 2015; Khatibi et al., 2018). Most of these measurements were conducted at the nanoscale to

microscale using nanoindentation or AFM. It is clear from Figure 6 that OM is the least stiff component in shales ($< 30 GPa$) and the pyrite is the most rigid constituent ($> 250\ GPa$).

2.1.2.1. Summary of application of AFM-based methods on OM-rich shales

AFM's capability to measure the mechanical properties of OM-rich shales has been the subject of several papers (Eliyahu et al., 2015; Emmanuel et al., 2016a, 2016b; Yang et al., 2017; Li et al., 2018b). It was shown that this mode of AFM can map the measured reduced modulus, then the map of measured reduced modulus was compared with the chemical spectral analyses of the scanned surfaces from SEM/EDS. Therefore, it is possible to use AFM-based nanomechanical characterization of shale to classify OM-rich shales based on stiffness measurements. Even though the impact of maturity on the stiffness and mechanical strength of OM was the subject of some AFM-based and nanoindentation-based publications, it is still unclear from this work whether the increase in maturity results in an increase or decrease in the stiffness of OM.
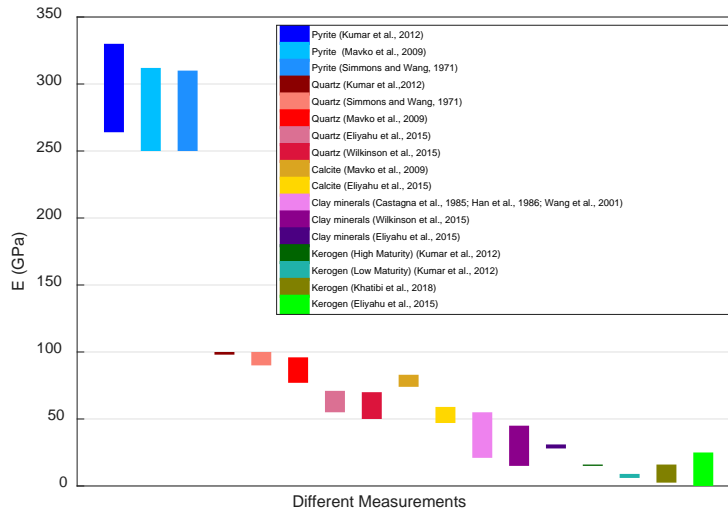

Figure 2.2. Young's modulus of important constituent minerals in OM-rich shales

32

The impact of OM maturity on the stiffness measurements using the AFM-based method has been studied by Eichmann et al., 2016a; 2018). Figure 2.3 shows the measured reduced elastic modulus for OM at different maturity levels from Emmanuel et al. (2016a) and Zargari et al. (2016), which was based on modulus mapping. There is a large difference between the results of these two previous papers. The moduli of OM increased from the sample with the lowest maturity to the sample with the higher maturity, and it stayed almost constant when the maturity increased further (Emmanuel et al., 2016a). As a result of maturation, the proportion of aromatic compounds increased, and the weight percentage of aliphatic $C - H$ bonds decreased. These chemical alterations led to an increase in kerogen density, and Emmanuel et al. (2016a) concluded that as the elastic modulus of synthetic organic polymers are highly and directly correlated with density, and they expected the same behavior for kerogen. Eichmann et al. (2018) measured the modulus of OM-rich shale samples using the PeakForce QNM^{TM} method. The samples had different thermal maturities from immature to overmature, but they did not observe a specific correlation between the maturity level and the elastic modulus of OM. Yang et al. (2017) showed that AFM-IR is capable of chemically mapping different types of OM within the OM-rich shales, but this method is not capable of measuring the mechanical properties quantitatively. Therefore, it is worthwhile to combine the stiffness measurement using AFM (PeakForce QNM^{TM}) with the AFM-IR to find the relationship between the types of OM and stiffness.

2.1.3. Comparison between nanoscale mechanical experimental methods

Overall, three nanoscale mechanical experimental methods have been applied to measure the mechanical properties of shales in the nano- to micro-scale. Two of them are nanoindentation-based method (gridded-nanoindentation and modulus mapping) and the other one is an AFM-based

method (PeakForce QNM^{TM}). Table 2.4 includes a summary of advantages and limitations of these three methods.
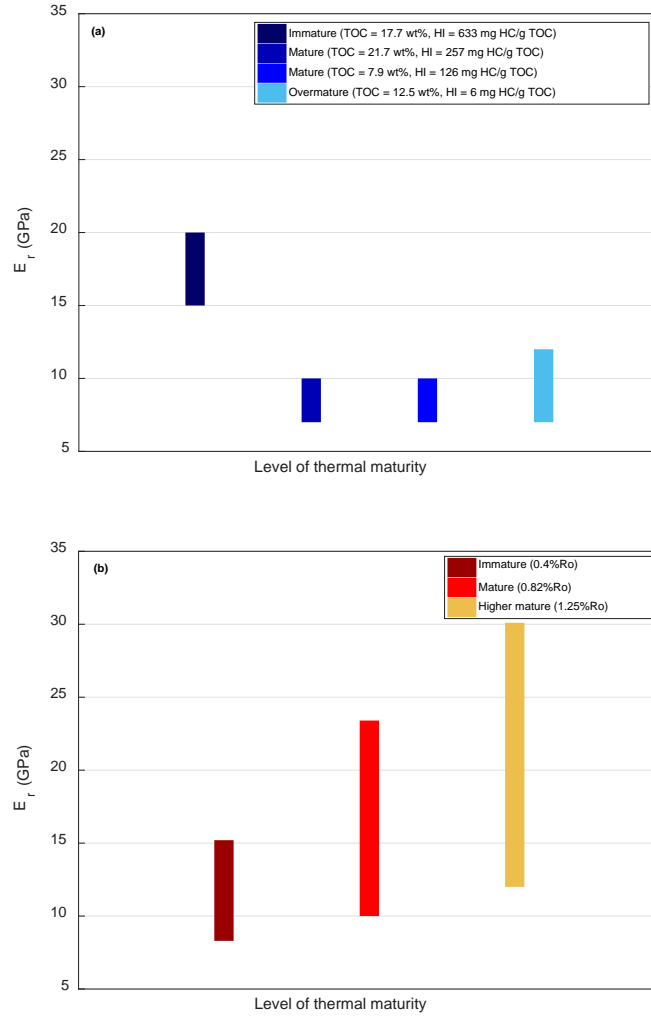
Figure 2.3. Reduced elastic modulus of kerogen at different maturity levels: (a) the results from Zargari et al. (2013), and (b) the results from Emmanuel et al. (2016a).

Table 2.4. The summary of advantages and limitations of each nanoscale mechanical characterization methods

Nanoscale mechanical characterization methods	Advantages	Limitations
Gridded Nanoindentation	Compatible for measuring both elastic and plastic properties	Finding the accurate indentation depth and spacing of the pattern for gridded-nanoindentation and are crucial to measure the moduli of the single component (i.e., a distinct mineral)
Modulus Mapping	Measuring the contact force, reduced modulus, the tip's amplitude, and the phase difference in the form of two dimensional (2D) images. This makes possible to easily compare these 2D images with the EDS elemental maps and recorded SEM images.	The modulus mapping is based on an assumption that the indenter tip has a specific shape such as a spherical shape, and the measured storage modulus is highly affected by the radius of contact.
PeakForce QNM^{TM} (AFM-based)	Measuring the reduced modulus continuously on the surface of sample. This makes possible to easily compare the measured reduced modulus data with the EDS elemental maps and recorded SEM images.	It applies a lower force and measures the elasticity modulus, and this makes hard to measure the creep properties with this method

2.1.3.1 Comparison between the gridded nanoindentation and modulus mapping techniques

According to Ulm and Abousleiman (2006), the main assumption of the gridded-nanoindentation method is that the two component materials have a distinguishable difference in their mechanical properties. Therefore, for complex materials such as shale that consists of more than two components, designing the pattern for gridded-nanoindentation is crucial to measure the moduli of the single component or phase (i.e., a distinct mineral), instead of measuring the moduli of the mixture of different minerals. However, the real contact force, the phase difference, and the amplitude of the tip are mapped directly in the whole area of interest in the modulus mapping method. Consequently, the reduced modulus is mapped in the whole area of interest. This capability of modulus mapping makes it possible to compare the recorded reduced modulus maps with the recorded SEM images of the same area.

For the complex materials such as shale, it is necessary to combine the gridded nanoindentation with statistical methods, such as deconvolution techniques or multivariate clustering techniques, to construct a histogram of each mechanical property over the nanoindentation area. The mean and standard deviation of the measured indentation modulus and hardness for each mechanical phase are crucial statistical parameters. Moreover, the probability that one set of recorded measurements (indentation modulus and hardness) belongs to a specific mechanical phase is the main basis for the algorithm to determine different mechanical phase. Therefore, the level of uncertainty for the measured indentation modulus and hardness for each mechanical phase are important in the accuracy of combined gridded nanoindentation with statistical methods.

In relation to investigating the creep behavior, a quasi-static nanoindentation creep test can provide modulus and hardness of the sample at the end of the creep test (maximum indentation depth), but it is important to understand how a sample behaves during the test. In the modulus mapping based on the nano-DMA method, the average value of the quasi-static force is kept constant, but it fluctuates a little because of the need to measure the contact stiffness continuously. The modulus is calculated at the start of the holding stage, and this is used to measure the contact area continuously. This allows an accurate and continuous calculation of the average penetration depth and contact pressure over time. Therefore, modulus mapping based on the nano-DMA method is capable of investigating the creep behavior during the test, unlike gridded nanoindentation.

The contact area is calculated differently in nanoindentation and modulus mapping. According to Oliver and Pharr (2004), the projected contact area in nanoindentation is determined from the area function (Eq. 23 in Oliver and Pharr, 2004). However, the modulus mapping assumes that the indenter tip has a spherical shape. Therefore, the contact area in the modulus mapping has a spherical shape, and the storage modulus is highly affected by the radius of contact. This difference in the way contact area is measured causes a difference in the accuracy between these two methods, and the nanoindentation method is more accurate for modulus measurement than modulus mapping (Zhao et al., 2019). The relationship between the size of the contact area and the resolution of nanoindentation and modulus mapping was studied by Zhao et al. (2019). In the modulus mapping method, the measured contact radius for organic matter and the stiff minerals is approximately 40 nm and 10 nm, respectively, and the estimated contact areas are smaller than $7.85 \times 10^3 \; nm^2$ (Zhao et al., 2019). A nanoindentation test was conducted on quartz in the same test area that modulus mapping was conducted. Zhao et al. (2019) measured the contact area of

indentation using the area function and estimated it to be $3.75 \times 10^5 \ nm^2$. The contact area of the nanoindentation method on the softer constituents is most likely larger than for quartz. Therefore, the measured reduced modulus in the modulus mapping method has a higher lateral resolution compared to measured indentation modulus in the nanoindentation method.

2.1.3.2. Comparison between the grided nanoindentation and AFM-based techniques

The PeakForce QNM^{TM} method has advantages and disadvantages compared to the gridded nanoindentation method. The main advantage of this method is that it provides a continuous measurement of the modulus for the different mechanical phases on the surface of shale samples, whereas gridded nanoindentation is based on a grid of nanoindentations over the specific area of the shale sample (i.e., the area of interest). Each indentation is made with a specific spatial distance from the other indentations. It is possible to compare the resulting modulus map from AFM-based methods (PeakForce QNM^{TM} and other similar methods) with the EDS elemental maps. This comparison is straightforward and can be used to determine the mineralogy of each mechanical phase (Eliyahu et al., 2015). The results from gridded nanoindentation and deconvolution methods are also comparable to the EDS elemental maps, but this comparison is not straightforward because the final product of gridded nanoindentation techniques is not a modulus map. The resulting deformation on the sample surface in the PeakForce QNM^{TM} method is approximately 5-20 nm (Eliyahu et al., 2015; Emmanuel et al., 2016a; Li et al., 2018a), but nanoindentation-based methods induce deformations usually at the scale of hundreds of nanometers, and in some cases up to micrometers (Deirieh et al., 2012; Ulm & Abousleiman, 2006). PeakForce QNM^{TM} is a non-destructive method because a relatively low force is applied to the sample surface (Li et al., 2018a;

Zeng et al., 2018). It is worth mentioning that other kinds of the AFM force mapping methods which apply a relatively low force are also non-destructive.

2.1.3.3. Comparison between modulus mapping and AFM-based techniques

Both the modulus mapping based on Nano-DMA and second mode of AFM force mapping methods, such as PeakForce QNM^{TM}, provide a modulus map of the sample surface, but there is a difference between the type of modulus that these two methods are measuring. The nano-DMA method applies a higher force, and as a result it measures the viscoelastic behavior of the sample. However, the methods based on the second mode of AFM force mapping apply a lower force and measure the elasticity modulus (Young's modulus) of the sample. The nano-DMA and gridded nanoindentation methods can be utilized to measure the creep behavior of the shales at the nanoscale (Liu et al., 2018a; Slim et al., 2019), while it is not easy to apply the second mode of AFM force mapping methods to investigate creep behavior.

2.2. Pore structure characterization methods

Conventionally petrophysical methods use a quantitative assessment of rock properties to characterize reservoirs for their hydrocarbon potential (Anovitz and Cole, 2015). One important information needed is whether pores (and not uncommonly fractures) are interconnected and how are they interconnected. These information leads to conclusions that how pores control the accumulation and migration of fluids (water, oil, and gas). The key properties of interest in petrophysical methods are lithology (e.g., grain fabric, mineralogy), porosity, permeability, water saturation, and density. The measurement methods are classified into three broad categories, (a) on core or crushed rock, (b) within the borehole using well logging tools, and (c) seismic methods. This review just focuses on the methods that are applied on core or crushed rocks. The methods in

this category can be divided into direct measurements on solids and indirect methods via imaging of a rock chip or core.

2.2.1 Direct methods

There are several methods to directly measure rock porosity: (1) saturation or imbibition, (2) buoyancy, (3) gas expansion (He porosimetry), (4) gas adsorption (BET) and (5) mercury intrusion porosimetry (MIP) (e.g., Clarkson et al., 2012; Hu et al., 2017; Kibria et al., 2018; Sondergeld et al., 2010). All these methods only measure the connected porosity of the samples as a fluid is used to be only accessible to sample surface-connected pores.

Saturation or imbibition: Imbibition is a capillary-force-controlled process during which a non-wetting fluid is displaced by a wetting fluid because of capillary pressure effect (Gao and Hu, 2016). The product of driving force and conductivity determines the rate of imbibition (Hu et al., 2001). Normally fluids such as dichloromethane or toluene have been used in the past, but more recently many researchers tried to make the experimental conditions more similar to reservoir conditions. Therefore, fluids such as brine have been used more recently. Handy (1960) introduced an equation to quantitatively describe the imbibition process in a water-air system. In this system, imbibition occurs vertically upward with negligible upward gravitational force. Applying Handy (1960) equation results in different imbibition slopes depending on how well interconnected the pore system is. A plot of cumulative imbibition mass/height vs. imbibition time on log-log scale shows Fickian diffusion-type behavior. Hu et al. (2012) reported three types of slopes for imbibition of different rocks in a log-log scale (0.5, 0.26, and 0.26 transitioning to 0.5) without assuming the existence of pore connectivity. Theoretical studies based on the percolation theory suggest that higher-slope values show that a pore system is well connected, while lower- slope values are a representation of low pore connectivity (Hu et al., 2012; Hunt et al., 2014).

Buoyancy: It is the force which applies upward by a fluid in opposition to the weight of a fully or partially immersed object. The buoyancy and saturation methods have slight differences. In the saturation method, the dry weight was determined first, then the rock sample was saturated with a wetting fluid with known density. The bulk volume of the saturated sample was calculated next. However, in buoyancy method, the saturated sample is suspended in a bath of the fluid, which is same as the saturating fluid, using a cradle to suspend the saturated sample. The actual weight of the suspended sample and cradle in the fluid is $(W_{sus} + W_{crad})$; therefore, the weight of the cradle (W_{crad}) is required. Moreover, W_{sus} is the weight of the suspended saturated sample (Anovitz and Cole, 2015).

Gas expansion methods: They are designed based on Boyle's law, and helium (He) porosimetry is the most well-known gas expansion method. These methods are classified as the most accurate techniques to measure effective porosity in lithologies such as sandstone and low permeable rocks as well. Helium has been used more in gas expansion methods comparing to other gases because its small molecules can penetrate small pores quickly, and due to its inertness, it does not adsorb on rock surfaces such as CO_2 or H_2O may do. Moreover, helium can be classified as an ideal gas usually for the employed experimental conditions (temperatures and pressures). Also due to high diffusivity of helium, it can be highly useful gas for determining porosity of low permeable rocks (Anovitz and Cole, 2015).

In this method, a dry core (or crushed rock) with a known bulk volume (V_{bulk}) is placed in a container with a known volume (V_a). This container is connected to the other container with a known volume (V_b), which is evacuated. Helium gas is released into the first container with a specified pressure (P_1) that is typically around 100 psi. This amount of He gas is then released to the second chamber and allowed to equilibrate throughout both containers. The He gas then

diffuses through the pores of the sample, which results in decrease of the pressure to a new stable level (P_2). Then the ideal gas law is employed to calculate the volume of the pores (Anovitz and Cole, 2015).

Gas adsorption methods: Adsorption is simply the adhesion of molecules, ions or atoms from a dissolved solid, liquid or gas to a surface. Low-pressure gas adsorption is usually used to measure the pore volume and surface area of geological materials. In low pressure adsorption experiments, the phase behavior is below the critical point of the fluid used; therefore, capillary condensation becomes important which leads to important information about pore structure, surface area and pore size (Anovitz and Cole, 2015).

Mercury intrusion porosimetry (MIP): While small angle neutron scattering (SANS) method provide information about both accessible and inaccessible porosity indiscriminately, fluid invasion techniques such as MIP is only capable of measuring pore systems connected to the boundaries of a sample end. Consequently, it provides a complementary information about the total volume and size distribution of edge-accessible porosity. MIP can characterize the pore throat size distributions in porous media from the micron scale to the nano scale. Moreover, the data from MIP measurement are indicative of various characteristics of the pore space and is employed to characterize a various physical property of the solid material as well (Anovitz and Cole, 2015). Applications of MIP can be divided into three main categories: 1) information gained using a special or multiple methods, such as pore cavity to pore throat size ratio, material permeability and fractal dimensions, and distribution of pore cavities associated with a pore throat size; 2) information gained from volume and mass measurements only, material volume and density, percent porosity and percent porosity filled, and interstitial void volume; 3) information obtained from Washburn's equation, pore volume distribution by pore area, number of pores, and pore size

(Webb and Orr, 1997; Webb, 2001, Anovitz and Cole, 2015). Mercury is the best example of non-wetting phase. Consequently, it cannot enter pores due to capillary action, and it can just access interconnected pores.

2.2.2 Imaging methods

It is possible to apply a broad range of direct imaging methods to explore the nature of porosity and its possible relationship with minerals in rock materials. The imaging methods includes scanning electron microscopy (SEM) with energy dispersive X-ray spectroscopy (EDX), focused ion beam-SEM (FIB-SEM), transmission electron microscopy (TEM), nuclear magnetic resonance imaging (NMRI), Atomic Force Microscopy, and X-ray tomography (Anovitz and Cole, 2015).

Scanning electron microscopy (SEM): Using SEM and EDX instruments, it is possible to look down into the pores, identify the minerals within the rock samples and understand the distribution of these minerals within the pores (Anovitz and Cole, 2015). In the SEM, the interactions of electron beam with the sample generates various signals as the SEM scanned the sample surface in the raster pattern. Consequently, the image is produced by recording those various signals (Huang et al., 2013). The end goal of pore structure characterization is usually focused on understanding both the topography and composition of pore structure. One main consideration in using SEM and EDX is the surface roughness and quality of polishing. Low quality of polishing leads to creation of artificial pores and fractures that causes an inaccurate accounting of true porosity. It is common to have an artificial pore at the contact between resilient phases such as feldspar/quartz and soft phases such as clays. To solve this issue, argon-ion milling is used to gently polish the surface to preserve true mineral texture (Erdman and Drenzek, 2013).

Focused Ion Beam-SEM (FIB-SEM): In this method, a series of sectioning and imaging is conducted to produce a sequence of SEM images. This technique leads to a 3D visualization of the minerals, pores, and structure of samples. Using these generated 3D images, it is possible to calculate pore-size distribution, porosity, permeability, and kerogen volume percentage (e.g., Heath et al., 2011; Curtis et al., 2012; Huang et al., 2013; Han et al., 2022).

Although FIB-SEM is popular and useful for 3D visualization, it has some limitations such as the sample area is extremely small. Consequently, results from FIB-SEM imaging may not be representative of the sample (Silin and Kneafsey, 2012). The FIB milling process, when specially conducts at high beam currents, can make to various form of artificial porosity. Moreover, small cracks can be generated because of machining. Therefore, it is necessary to investigate the nature of these cracks such as the existence of clay particles inside the fractures and their origins (Anovitz and Cole, 2015).

2.2.3. Scattering Techniques

The instrument geometry and data acquisition scheme (e.g., pinhole, Bonse-Hart, spin-echo, time-of-flight etc.) or the type of radiation (X-ray or light, neutron) employed are two ways of classifying the scattering techniques (Anovitz and Cole, 2015). Neutrons are particles with low level of interacting forces between them, so they are ideal for nondestructive testing of large sample volumes (Zhang et al., 2019). Neutron scattering provides an information for the structure of both connected and isolated pores, but fluid invasion methods such as MIP, helium pycnometry, and low-pressure adsorption just measure the connected pores (e.g., Clarkson et al., 2012, 2013; Melnichenko, 2016; Zhang et al., 2019).

Chapter 3:

Methods

3.1. Sample preparation

Shale samples for the mechanical characterization in nanoscale are from the lower section of Bakken Formation (Anyanwu, 2015). The samples were cut into small cubes with each side of roughly 1.0 cm. Then it was polished with sandpapers with grit sizes of 180, 400, 800, and 1200. After polishing with sandpaper, it was polished with Argon Ion Polishing (IM4000 Plus manufactured by Hitachi) to make a smoother surface. The process of polishing with Argon Ion Polishing is as follows: The sample was polished in the flat mode at 4 kV and angle of 85° for 2-3 hours. This method produces a highly smooth surface free from artifacts, which are common in mechanical polishing of shales (Loucks et al., 2009). Shale samples for investigating the pore structure are from the Bossier and Haynesville Formations (Wang, 2019). The samples were cut into approximately $10 \, mm \times 10 \, mm \times 5 \, mm$ sections for fine polishing and milling.

3.2. Scanning electron microscopy

The SEM with EDS has been used to identify different minerals and pore spaces in the shale samples. For the pore structure analysis, the SEM images were taken by Hitachi S-4800 II FE-SEM. For the nanomechanical characterization of shales, the SEM images were taken by Hitachi S-3000N variable pressure SEM, which has an integrated EDS system. Using EDS, it is possible to identify OM within organic-rich shales.

3.3. Atomic Force Microscopy (AFM)

Nanomechanical characterization and pore structure analyses were conducted using the Asylum Research Cypher-ES AFM (Oxford Instruments). AFM was introduced for the first time by Binnig et al. (1982), and the scanning-tunneling microscopy (STM) was precursor to current version of AFM. Binnig et al. (1986) extended STM applications to scan surfaces other than

conductive and semiconductive materials, and this resulted in the invention of AFM (see Figure 3.1 for a general schematic).
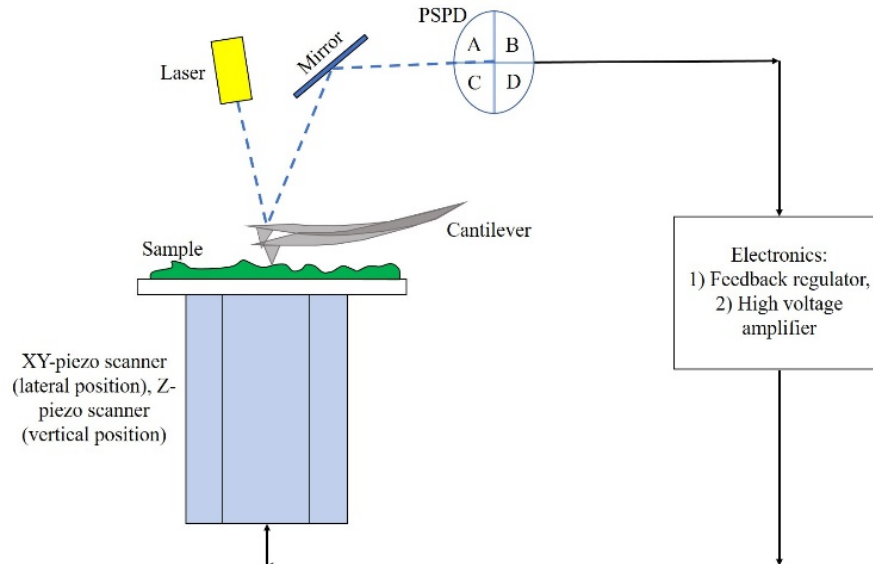

Figure 3.1. General schematic of a typical AFM. A reflected laser from the cantilever is detected by the quadrant photodiode (PSPD), and a signal is transmitted to the data acquisition equipment.

The tip was mounted on a cantilever spring, and the monitoring system controlled the cantilever deflection corresponding to the tip/surface forces (Binnig et al., 1986). As the tip/surface interaction forces are a function of gap width, the AFM feedback loop can keep the gap between tip and surface constant using vertical tip displacement compensating for cantilever deflection.

In AFM analyses, a flexible cantilever acts as a spring while it is scanning a sample or substrate. This makes possible to determine the net force between a coating at the tip of the cantilever and a substrate or a sample. The arm of cantilever is bended as a result of local repulsive and attractive forces between the tip and sample. A deflection of the cantilever is optically detected and converted into an electrical signal (The laser, mirror, and PSPD, which is Position-Sensitive Photo Detector, parts in Figure 3.1). The electrical signal is used to determine the force vs distance

curve using Hook's law (Figure 3.2). A focused laser beam is reflected from the end of the cantilever onto PSPD. Based on the optical lever principle, a small deflection of the cantilever is converted to a large deflection in the location of the reflected signal in a PSPD.
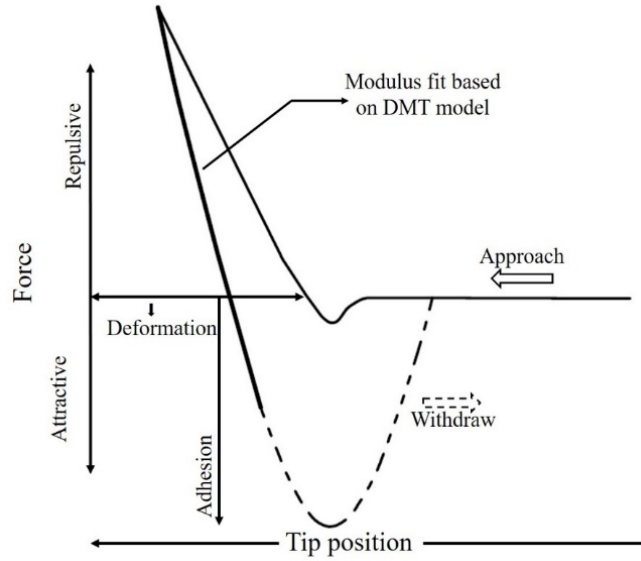

Figure 3.2. Schematic of a generated force-distance curve for a single tapping of AFM.

Hertz (1882) provided the first satisfactory analysis of stress at the contact between two elastic solids. Hertz assumed that the contact between two solids has no adhesion. Considering a contact between a rigid sphere with a radius R and an elastic half-space (figure 3.3a), according to Hertz theory of contact mechanics, the contact radius a is related to the applied load F, the radius of rigid sphere R, and the elastic properties of both materials

$$a^3 = \left(\frac{3FR}{4E^*}\right) \tag{3.1}$$

where E^* is the combined modulus of the rigid sphere and an elastic half-space given by

$$\frac{1}{E^*} = \frac{(1 - v_1^2)}{E_1} + \frac{(1 - v_2^2)}{E_2} \tag{3.2}$$

In Equation 3.2, E_1 and v_1 are the elastic modulus and Poisson's ratio of the rigid sphere, and E_2 and v_2 are the elastic modulus and Poisson's ratio of the elastic half-space.

According to Hertz the penetration depth d is related to contact radius and rigid sphere radius R as $d = \frac{a^2}{R}$, which results in

$$d = \left(\frac{9F^2}{16RE^{*2}}\right)^{1/3}$$
(3.3)

The maximum pressure p_0 is related to the applied load F and contact radius as $p_0 = \frac{3F}{2\pi a^2}$, which results in

$$p_0 = \left(\frac{6FE^{*2}}{\pi^3 R^2}\right)^{1/3}$$
(3.4)

Considering a contact between a rigid cylinder with flat end and an elastic half-space (figure 3.3b), the relationship between the penetration depth d, applied load F, and the radius of rigid cylinder R, is given by

$$F = 2RE^*d$$
(3.5)
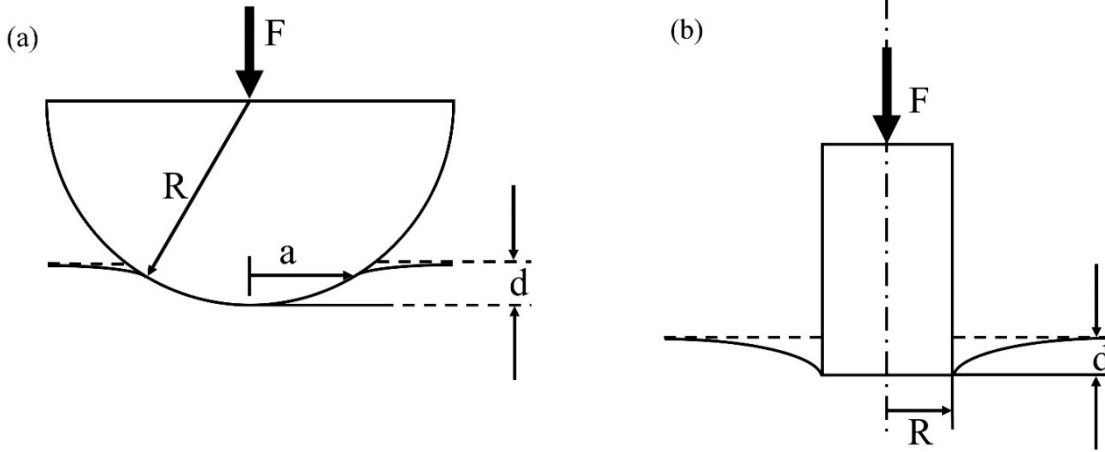
Figure 3.3. (a) Contact of a rigid sphere with an elastic half-space and (b) contact between a rigid cylinder and an elastic half-space

According to Oliver-Pharr model (1992), for all axisymmetric indenter, there exist a constant relationship between the elastic contact stiffness, S, the projected are of contact, A, and the reduced or indentation modulus, E^*:

$$E^* = \frac{\sqrt{\pi}}{2} \frac{S}{\sqrt{A}} \tag{3.6}$$

where S is an elastic contact stiffness (or unloading indentation stiffness) is defined as the slope of the upper part of the unloading curve. The projected area of contact, A, is simply calculated from the radius of the contact, a,

$$A = \pi a^2 \tag{3.7}$$

Based on Oliver-Pharr contact model, the radius of contact, a, is computed as follows:

$$a = \sqrt{2h_c R - h_c^2} \tag{3.8}$$

In this Equation, h_c is the contact depth, which is computed from the Oliver-Pharr model,

$$h_c = h - \varepsilon \frac{F}{S} \tag{3.9}$$

where h is the total measured displacement into the sample, and ε is a geometric constant, with values of 0.72, 0.75, and 1 for the conical indenter, paraboloid of revolution and the flat punch, respectively. It is clear from both Hertz model and Oliver-Pharr model that contact radius is calculated by nominal radius of indenter tip, contact depth, and applied load.

One of the most crucial steps in many AFM applications is choosing a suitable AFM probe for accurate measurements. The AFM probe with a given cantilever spring constant, can measure the limited range of Young's modulus. The AFM probe for Force-Distance (F-D) curve experiments is PPP-NCLR which is manufactured by Nanosensors. The average normal stiffness of PPP-NCLR probe is 48 N/m which is suitable for measuring the stiffness of OM. In F-D curve experiment protocols, the deflection sensitivity of the probe was determined by ramping onto a stiff Silicon sample ($E = 150\ GPa$) after every laser alignment. A PMMA sample was used as a reference to keep track of tip shape and radius (49.5 nm).

Figure 3.4 shows schematic of the mechanism of LFM. The scan direction in LFM is perpendicular to the length of probe cantilever (figure 3.4a). The relative lateral displacement (D) between the holder and sample is increased at a constant rate. The normal load F_n is kept constant by a feedback loop, and the resulting lateral force from the relative lateral displacement, F_L is measured (Figure 3.4b).
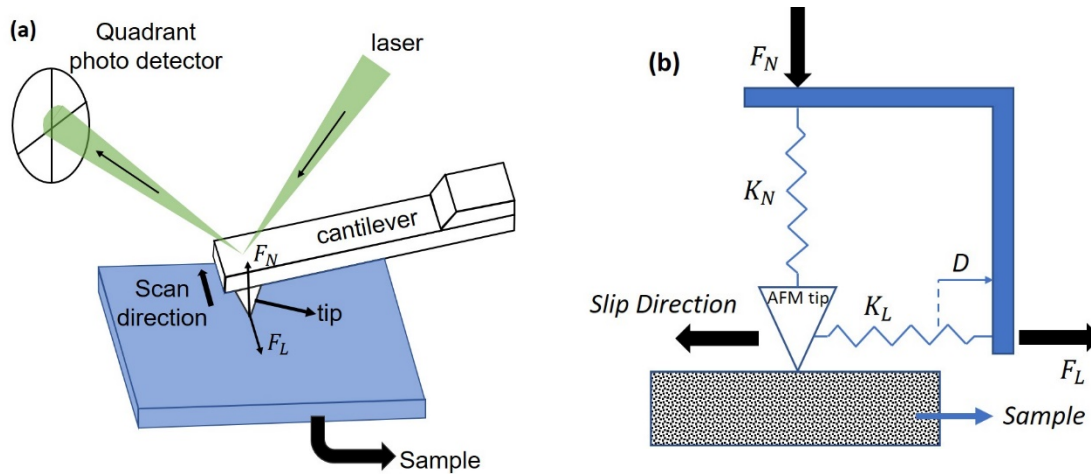
Figure 3.4. (a) A schematic of the mechanism of LFM. (b) The relative lateral displacement (D) between the holder and sample increases at a constant rate. The normal load F_n is kept constant by a feedback loop, and the resulting lateral force from the relative lateral displacement, F_L is measured.

Contact mode was used, and CSC38A probes manufactured by MikorMasch and PPP-LFMR probes manufactured by Nanosensors have been used for lateral force microscopy (LFM) experiments. The average normal stiffness of CSC38A and PPP-LFMR probes are 0.09 N/m and 0.2 N/m, respectively. The lateral force calibration was conducted based on the wedge method (Ogletree et al., 1996; Varenberg et al., 2003), which returned a conversion factor of $299.14 \pm 56.56 \; {}^{nN}/_V$ for CSC38A and $703.99 \pm 11.77 \; {}^{nN}/_V$ for PPP-LFMR probe. Figure 3.5 presents the calculated lateral force calibration parameters for one scan line.

In the wedge method, the standard sample of TGF11 manufactured by MikroMasch has been scanned and the lateral force signal recorded. When plotting the lateral force signal vs. the shear displacement for both the trace and retrace scan directions, a friction loop results (Figure.

3.5). The values of W and Δ are calculated as the following (Varenberg et al., 2003):

$$W = \frac{T_u - T_d}{2} \tag{3.10}$$

$$\Delta = \frac{T_u + T_d}{2} \tag{3.11}$$

where T is the recorded lateral signal in Volts, W is the half-width of the friction loop, and Δ is the offset of the friction loop. The indexes of u and d are related to the uphill (trace) and downhill (retrace) movement of the cantilever tip, respectively.
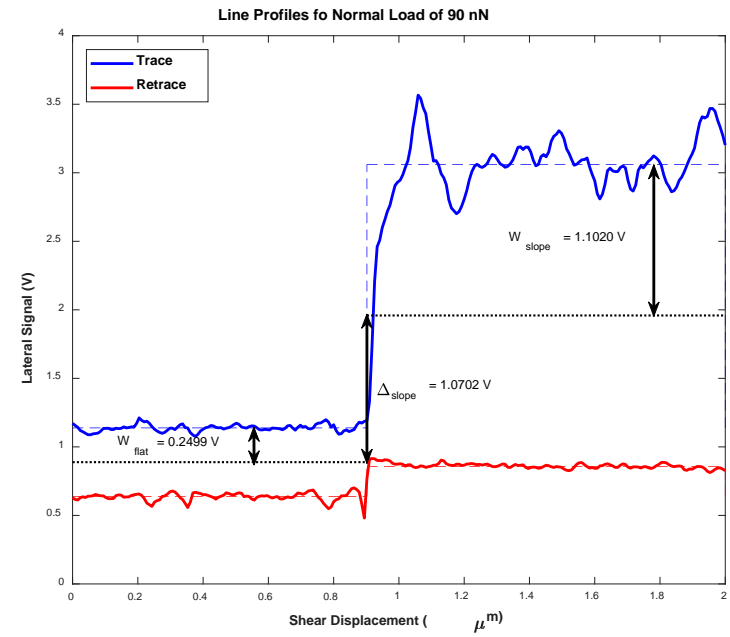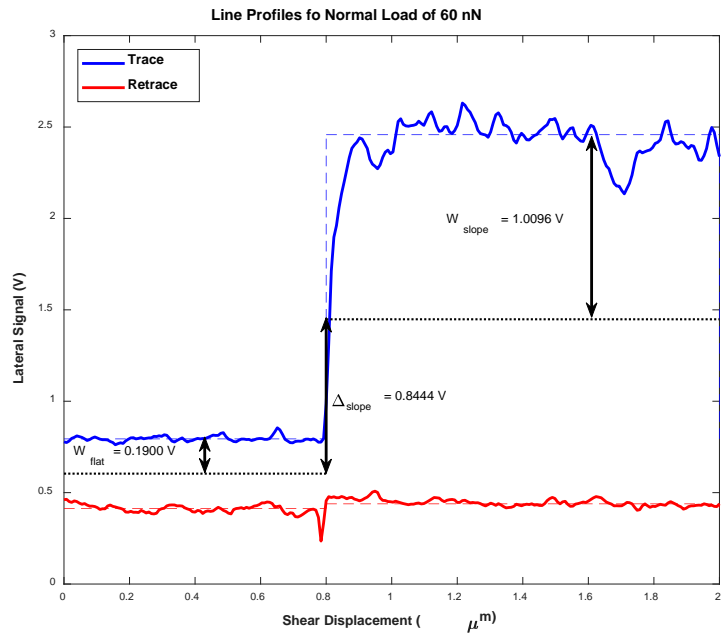
Figure 3.5. Friction loop and calculated lateral force calibration parameters for one scan line at two different normal loads

Figure 3.6 showed the calculated calibration parameters for seven different scan lines for different Deflection SetPoint (V) (1.888, 2.518, 2.833, 3.147, 3.462, 3.777, 4.091, 4.406, 4.721, 5.350, and 5.665). These SetPoints are associated with 11 corresponding normal loads (30 nN, 40 nN, 45 nN, 50 nN, 55 nN, 60 nN, 65 nN, 70 nN, 75 nN, 85 nN, and 90 nN). Then, a linear fit to scattered data for each W and Δ are calculated, and the slopes $\Delta' \equiv \frac{d\Delta}{dL}$ and $W' \equiv \frac{dW}{dL}$. L in these equations is the Deflection SetPoint. Ogletree et al. (1996) assumed that there is a linear relationship between W and applied normal load and Δ and applied normal load, so the impact of any dc offset in the lateral force sensor and adhesion force are eliminated.

The two slopes Δ' and W' are calculated as follows (Ogletree et al., 1996):

$$\left(\frac{\alpha}{InvOLS * K}\right)\Delta'_o = \Delta' = \frac{(1 + \mu^2)\sin\theta\cos\theta}{\cos^2\theta - \mu^2\sin^2\theta} \tag{3.12}$$

$$\left(\frac{\alpha}{InvOLS * K}\right)W'_o = W' = \frac{\mu}{\cos^2\theta - \mu^2\sin^2\theta} \tag{3.13}$$

where α is the lateral force calibration factor, $InvOLS$ is the inverse optical lever sensitivity in $\frac{nm}{V}$, K is the normal spring constant of the probe, μ is the friction coefficient of the standard sample, θ is the angle of the sloping section of the standard sample, and the subscript o corresponds to the values in the Voltage. Using the ratio of equation (3.12) and (3.13), it is possible to find the friction coefficient between the tip and sample surface by solving the following equation (3.14):

$$\mu + \frac{1}{\mu} = \frac{2\Delta'_o}{W'_o \sin 2\theta} \tag{3.14}$$

After calculating the tip-surface friction coefficient, it is possible to calculate α from the equations for W' and Δ'. Table 3 shows the information of linear fits to the recorded calibrated data (the scattered data which is shown in Figure 8). Rearranging the equation 3.14 results in a quadratic equation (eq. 3.15). Solving this quadratic equation, We find two values for friction coefficient (μ): $\mu = 0.3621, 2.7614$. The $\mu = 0.3621$ is the acceptable value.

$$W_o' \sin 2\theta\, \mu^2 - 2\Delta_o'\mu + W_o' \sin 2\theta = 0 \tag{3.15}$$
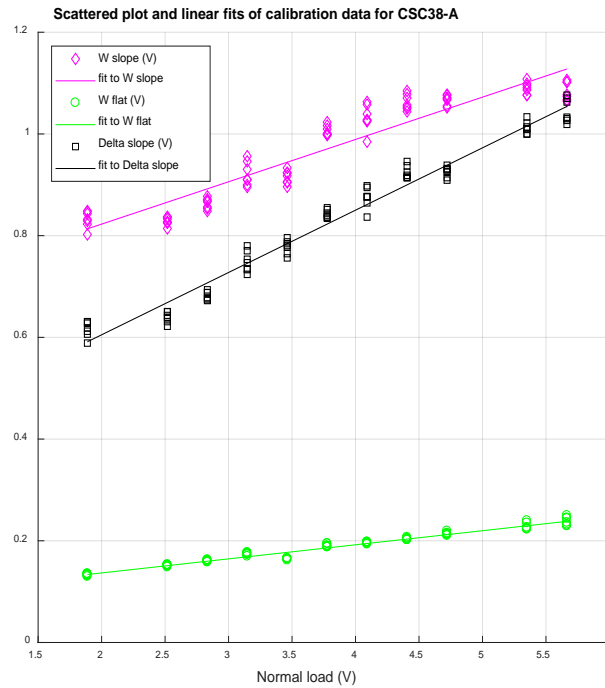
Figure 3.6 Scattered plot and linear fits to the calibration parameters (W_{slope} and W_{flat} are the W for the slope section, and flat section, respectively. Δ_{slope} is the Δ for the slope section)

Chapter 4:

Investigating the mechanical properties of the shale organic matter in nanoscale using AFM

4.1 Results of SEM/EDS analyses

SEM and EDS analyses were conducted on the Bakken Shale samples to find the OM regions on the sample. Figure 4.1 shows the SEM images of the Bakken Shale sample in the backscattered electron (BSE) detection mode. In both Figure 4.1-a and -b, the OM is identified. Figure 4.2 shows the EDS elemental mapping in the same area as Figure 4.1. Figure 4.3 indicates the comparison of the EDS spectra of OM and inorganic constituent minerals. The EDS spectra of point one (Figure 4.3b) shows that carbon is the dominant element in the dark ellipsoid area of the sample. The EDS spectra of points two (Figure 4.3c) and point 6 (Figure 4.3g) show that pyrite is the dominant constituent mineral at these points. The EDS spectra of point three (Figure 4.3d) points out that feldspar is the dominant phase at this point. The EDS spectra of points four (Figure 4.3e) and point 5 (Figure 4.3f) exhibits that clay minerals are the dominant constituent mineral at these points.
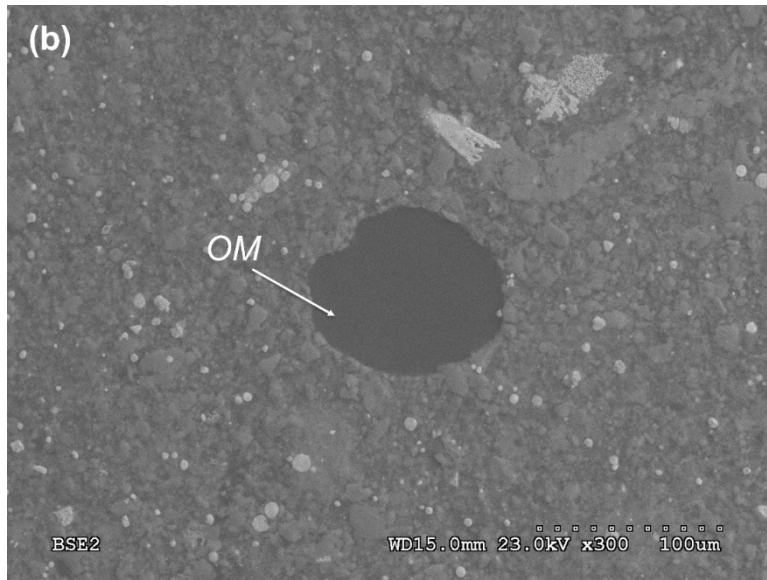
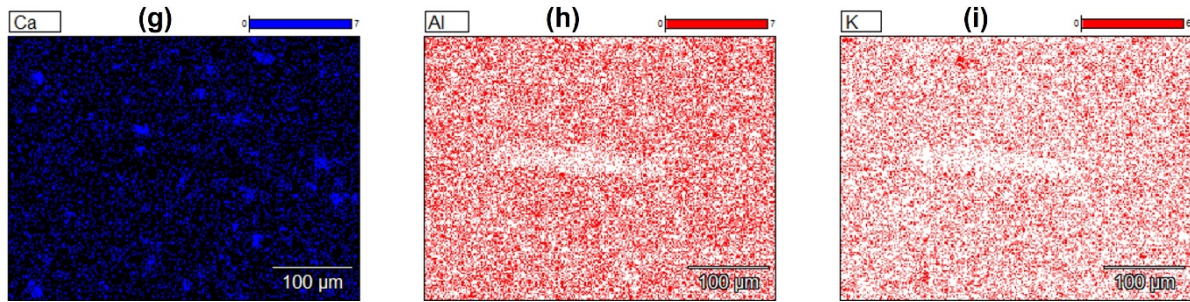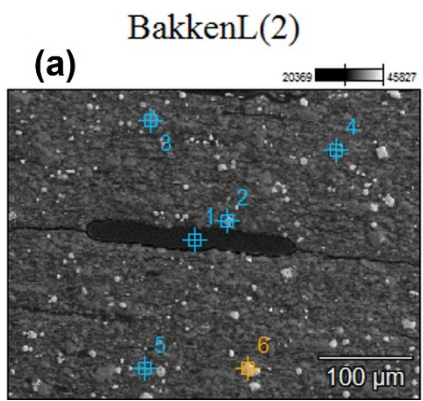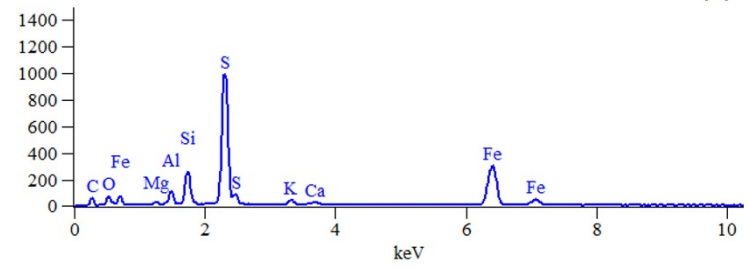Figure 4.1. SEM images of the Bakken Shale sample in the BSE mode
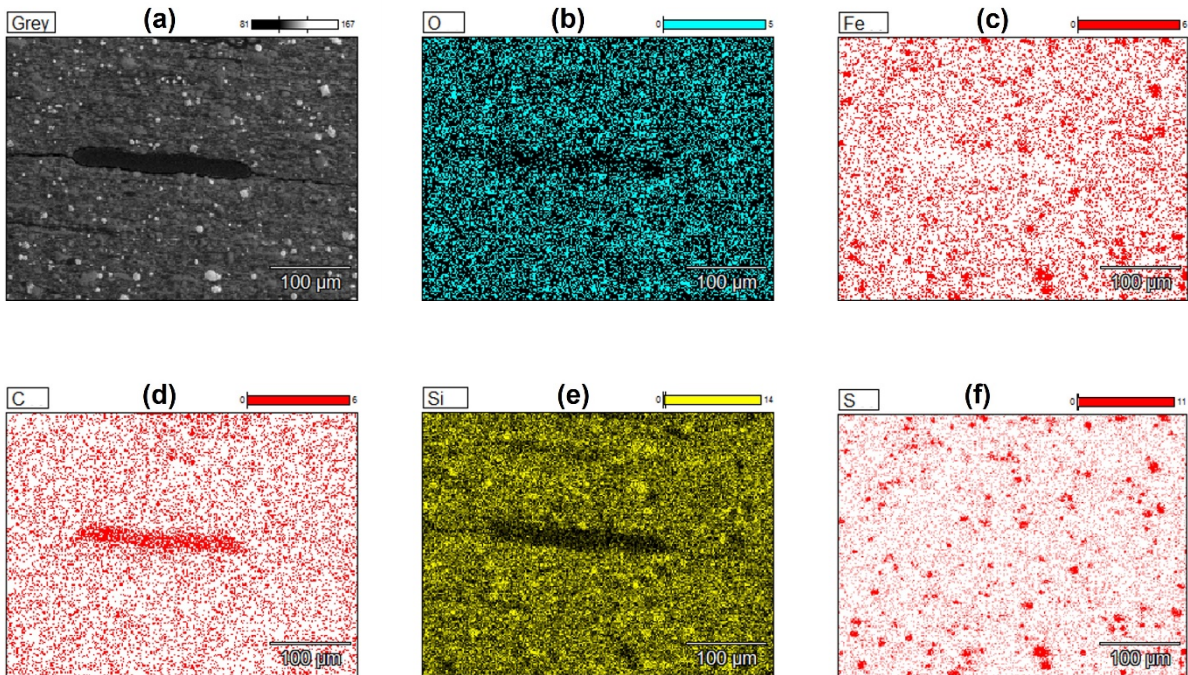
Figure 4.2. EDS elemental mapping in the areas of interest: (a) original SEM in BSE mode, (b) oxygen, (c) iron, (d) carbon, (e) silica, (f) sulfur, (g) calcium, (h) aluminum, and (i) potassium.

BakkenL(2)
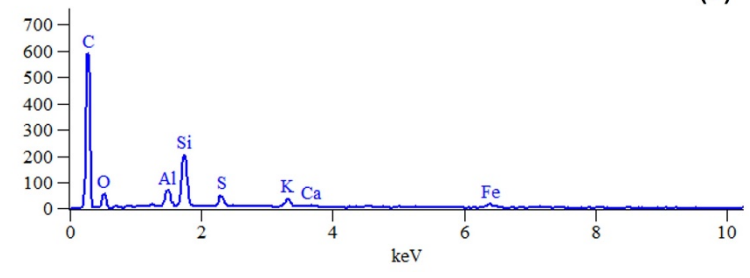
(a)

(b) Full scale counts: 589   BakkenL(2)_pt1
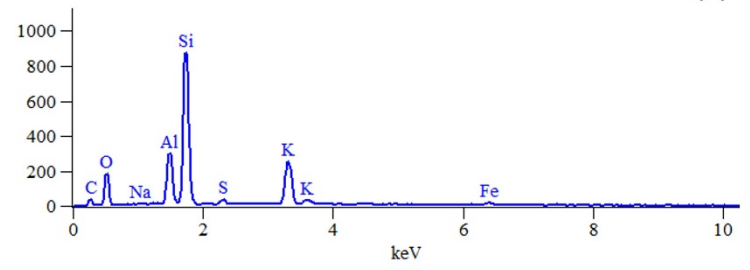
(c) Full scale counts: 989   BakkenL(2)_pt2

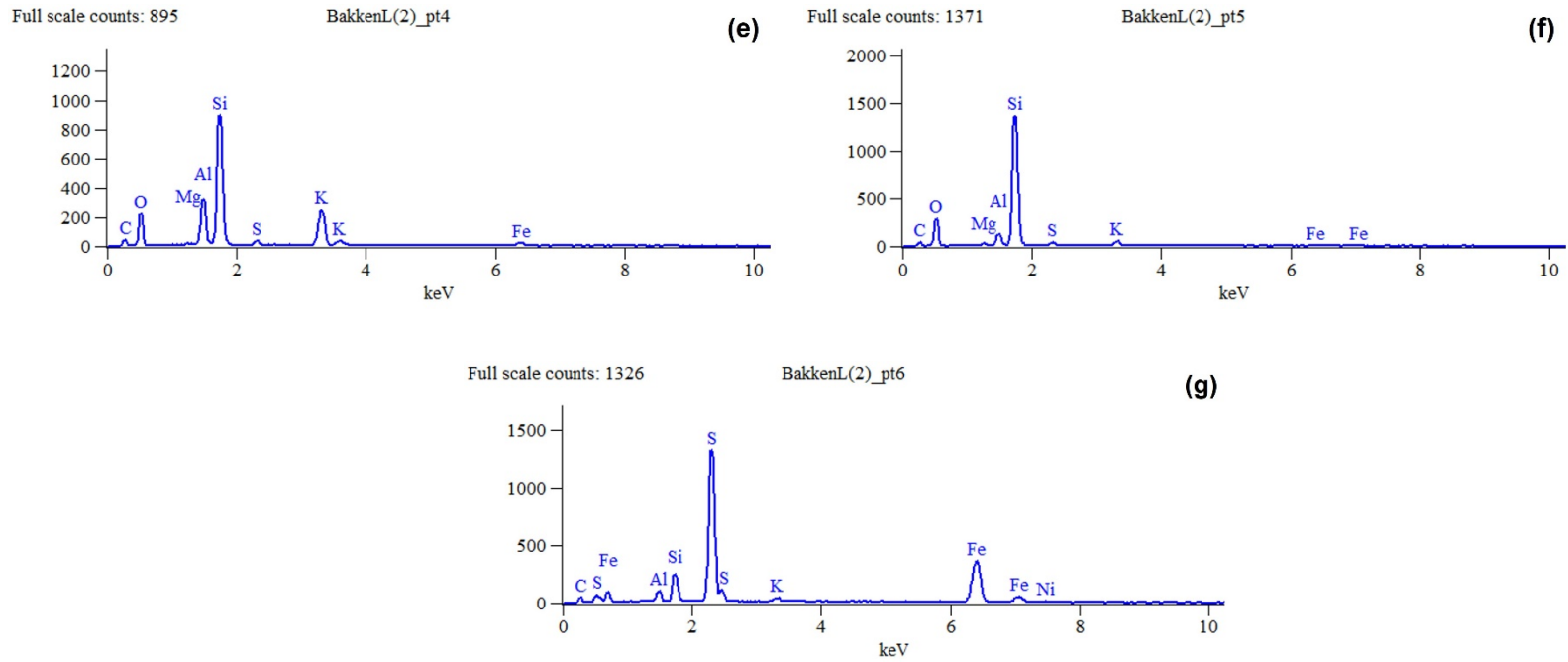(d) Full scale counts: 873   BakkenL(2)_pt3

Figure 4.3. EDS spectra of OM and inorganic constituent minerals at areas of interest; (a) backscattered image of the area of interest and location of different measurement points, (b-g) EDS spectra of six different points, and point one (b) is OM and five other points (c-g) are inorganic constituent minerals.

4.2. Results of Force-Distance curve tests

Figure 4.4 shows the surface topography of area of interest within OM (top) and their surface topography in 3D (bottom). The location of measured F-D curves is shown in Figure 4.4a and c. The Young's modulus of OM is measured using the Hertz and Oliver-Pharr contact model.
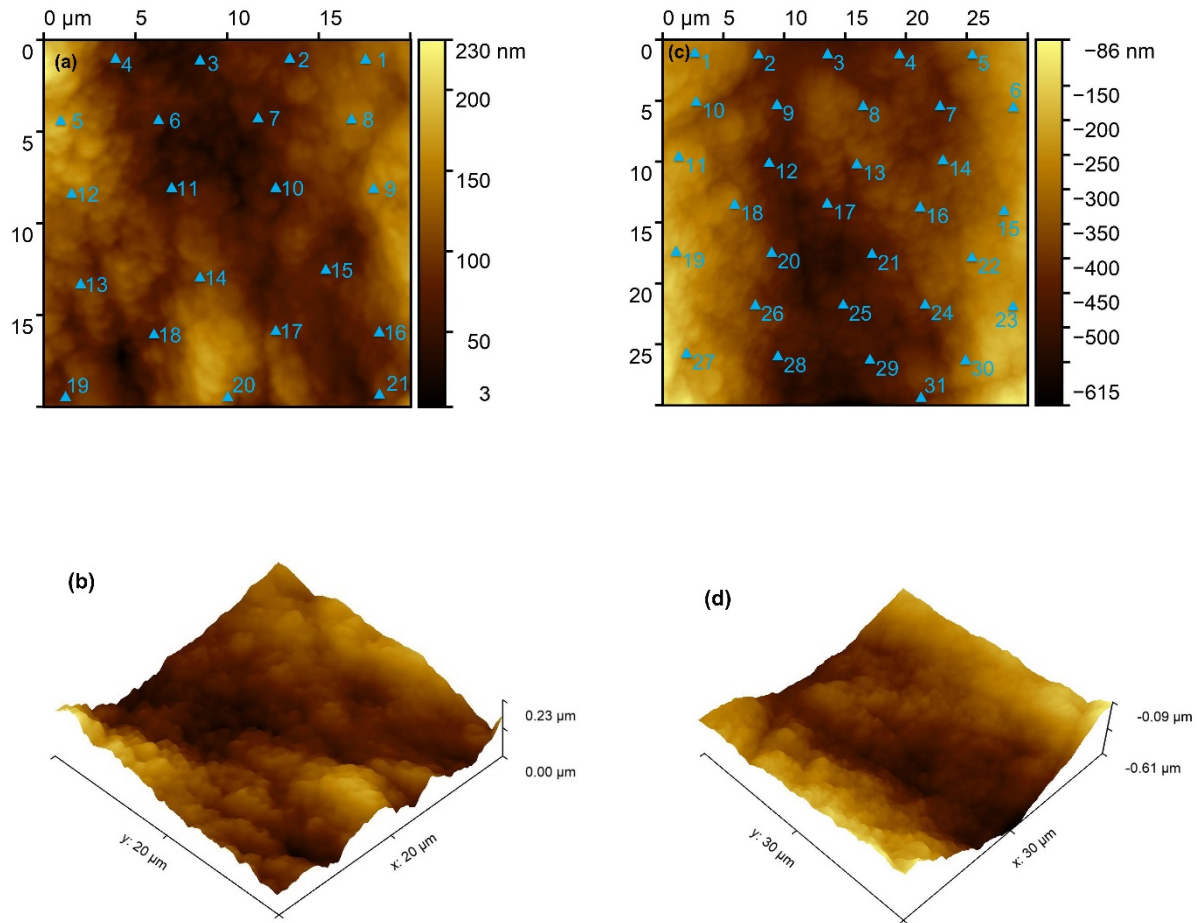

Figure 4.4 Surface topography of areas of interest within OM (top) and their surface topography in 3D (bottom).
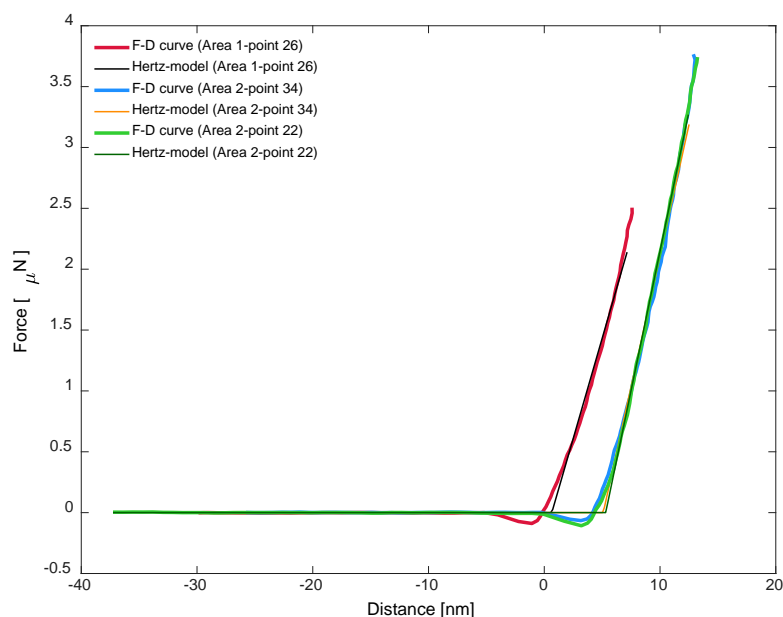
Figure 4.5 Force-Distance curve experiments at three different locations of the OM and their fitted Hertz-model

The measured Young's modulus (E) from the fitted Hertz-model is in the range of $1.5 - 4.5 \, GPa$, which is in the same range as the previously published works in the literature (Eliyahu et al., 2015; Emmanuel et al., 2016a; Li et al., 2018b). The histogram of the measured Young's modulus of OM is shown in Figure 4.6. The histogram shows two mechanical phases in the measured Young's modulus. Phase one has Young's modulus of less than 5 GPa or slightly higher than 5 GPa, and phase two has Young's modulus of 10 GPa or higher. Phases one and two are most likely related to bitumen and kerogen, respectively.
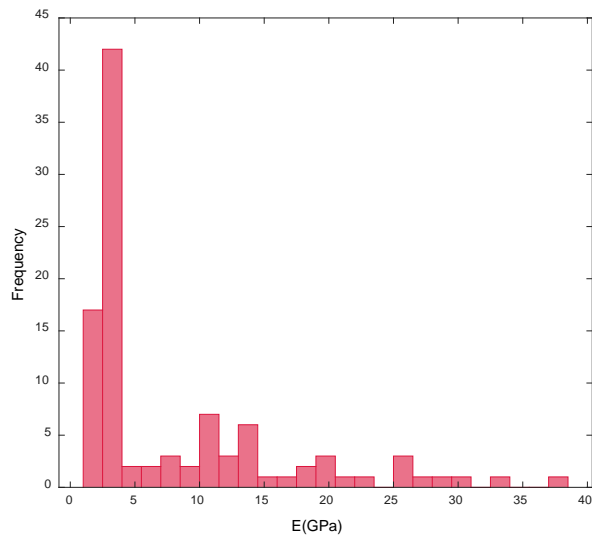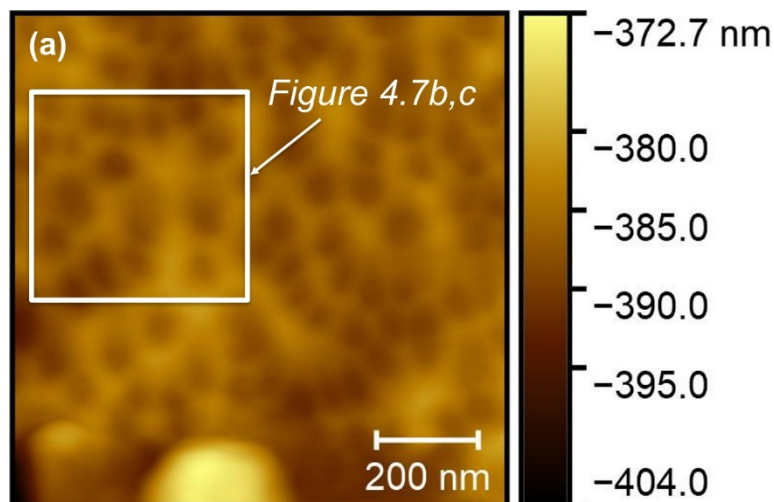
Figure 4.6 Histogram of the measured Young's modulus of OM

4.3. Results of LFM experiments

Figure 4.7a shows the surface topography of OM for an area of $(960 \times 960 \ nm^2)$ in 2D, and Figures 4.7b-c present the surface topography in the smaller region $(450 \times 450 \ nm^2)$ within Figure 4.7a. The surface topography does change just roughly 10 nm in the region with an area of $(450 \times 450 \ nm^2)$.
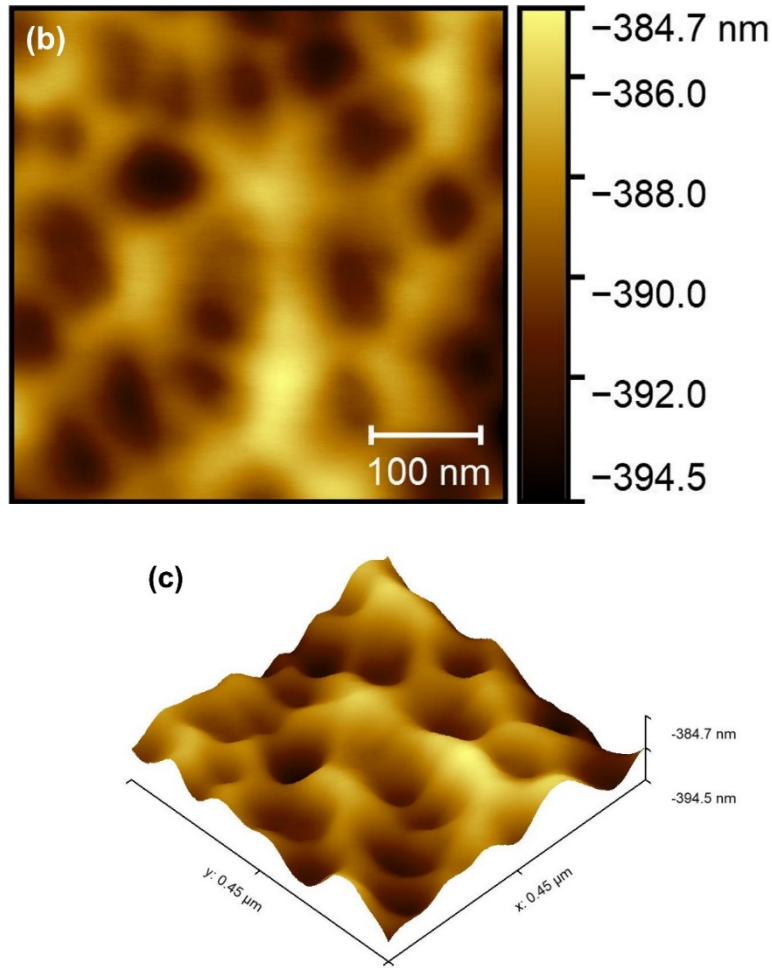
Figure 4.7 (a) A surface topography of the OM in 2D for an area of $(960 \times 960 \ nm^2)$, (b, and c) A surface topography of OM in the smaller region $(450 \times 450 \ nm^2)$ within the fig. 4.7(a). Figure 4.7b, and c are in 2D and 3D, respectively

LFM measurements were conducted over a range of applied loads varying from 9.6 nN to 68.3 nN. Two exemplary friction loops, measured under applied loads of 9.6 nN and 68.3 nN are shown in Figure 4.8, which shows that the lateral force (friction force) is increasing roughly as a function of increasingly applied load. Different number of friction loops were conducted for each applied load. The applied loads, F_l, and their corresponding number of friction loops, n, are as follows: $9.6 \ nN \ (345)$, $15.5 \ nN \ (322)$, $22.8 \ nN \ (299)$, $34.1 \ nN \ (309)$, $45.5 \ nN \ (260)$,

56.9 nN (338), 68.3 nN (328). There was no 'stick-slip' motion being observed, but some local 'stick' events were observed.
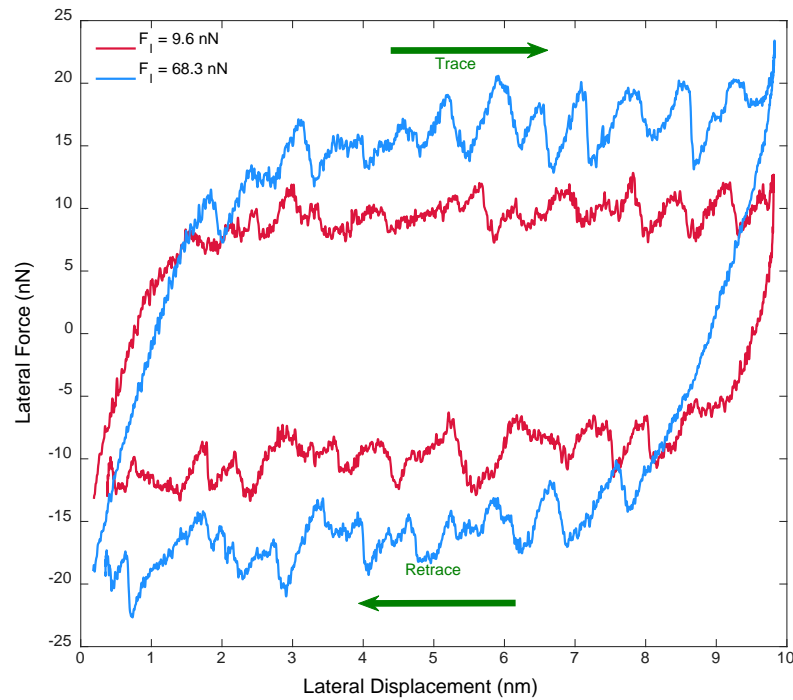

Figure 4.8 Friction loops acquired on OM under applied loads of 9.6 nN and 68.3 nN. In this graph the forward scan direction (trace) and backward scan direction (retrace) are shown.

The load-dependency of friction was investigated and is shown in Figure 4.9. The red curve is the result of the Hertz-plus offset model and the circles with error bars are the average of the measured friction force under each applied load and the magnitude of change in measured friction force.
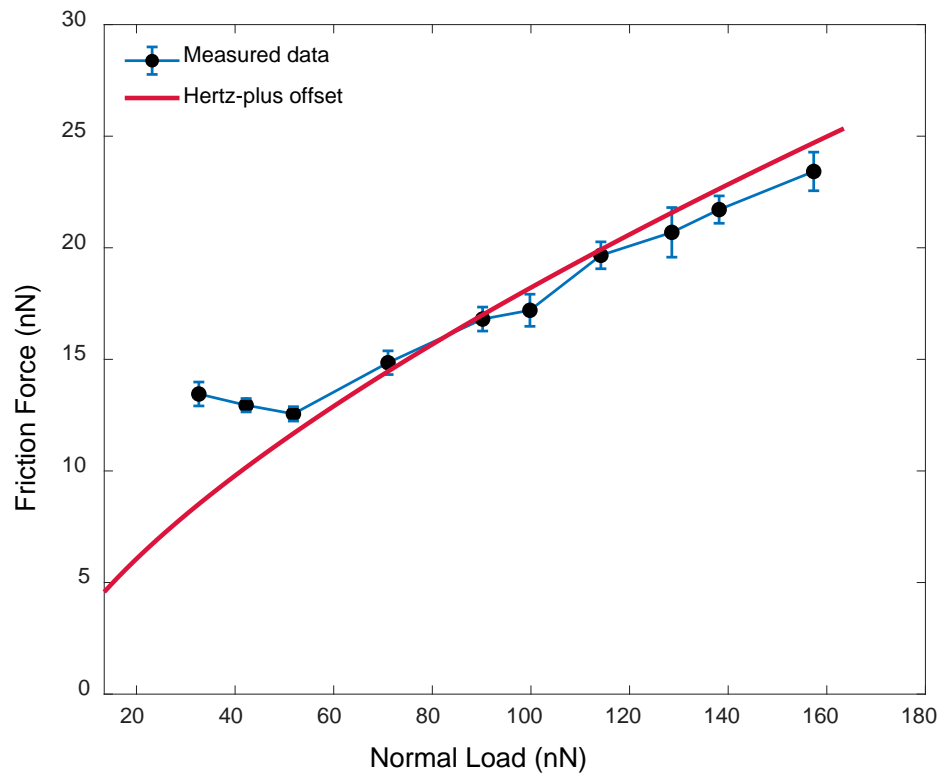
Figure 4.9 Load-dependent friction, with normal force representing the combination of applied load and adhesion force.

Chapter 5:

Quantitative studies of shale pore structure using AFM and image processing

5.1 Quantitative analyses of pores

The pores must be identified before their quantitative analyses. The *Grains* module of Gwyddion software has different methods to obtain the pore distribution including the Threshold method, Edge Detection method, Segmentation method, Otsu's method and Watershed method. The *Invert Height* function was used to mark the pores (Zhao et al., 2019). The main principal in the watershed method is that the water flows to a region with a local minimum potential. The following steps explain the process of pore evaluation using this method: (1) the water drops all over the surface of the sample; (2) if the water drop is not at a local minimum, it flows along the steepest path to minimize its potential energy; and (3) finally, the following geometrical properties of the pores are measured including pore size, plane porosity, pore surface, are and pore volume, which is assessed by the volume of water flowed to the local minimums (Zhao et al., 2019).

5.2 Results

5.2.1 Results from SEM image analyses

SEM analyses was performed on Bossier and Haynesville Shale sample (Figures 5.1-5.2). The pore diameter and area were measured using ImageJ software, which is an open-source software provided by the National Institute of Health (NIH). An analysis the SEM images shows that the pores are mainly with the *nm-* and *µm-* regime. Loucks et al. (2012) introduced a descriptive classification scheme of the matrix-related pores in shale: interparticle pores (pores between crystals and mineral particles), intraparticle pores (pores within particles), and OM pores. All of these pore types are observed in the SEM images of our shale samples. Figure 5.1 shows the SEM analyses of Bossier Shale sample. Intraparticle pores and fractures are observed in Figure 5.1a, and the diameter of these intraparticle pores are between 80 nm and 210 nm. Observed intraparticle

pores in Figure 5.1b are narrower than the ones in Figure 5.1a. Many slit-like pores and a region of porous OM are observed in this figure as well. The diameters of OM pores are approximately about 10 nm to 150 nm (Figure 5.1c). Figure 5.1d shows intraparticle pores, whose diameters are approximately about 100-–160 nm. Bubble-like pores, slit-like pores, and pyrite framboids are also observed in Figure 5.1e. The diameters of bubble-like pores are roughly 80–180 nm (Figure 5.1f). The openings of slit-like pores are about 20–60 nm and a few pores with openings close to 100 nm (Figure 5.1f).
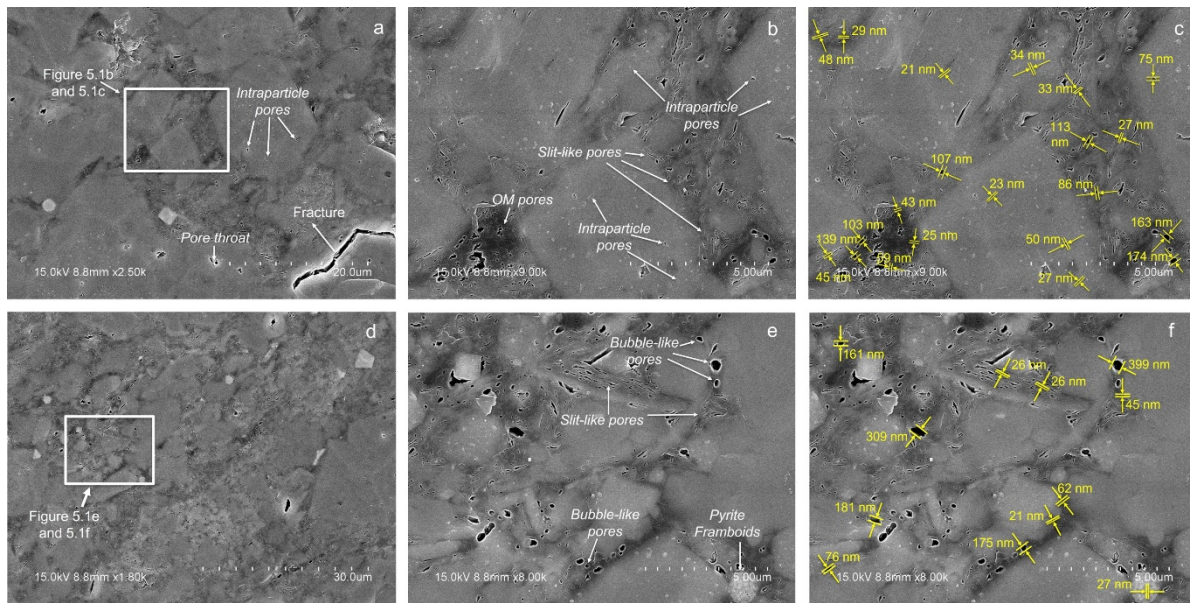

Figure 5.1. SEM images for a Bossier Shale sample; (a) wider region of the 5.1b and c images, fractures, intraparticle pores, and pore throat; (b) intraparticle pores, OM pores, and slit-like pores; (c) showing some of the measured pore diameters; (d) wider region of 5.1e and f, and intraparticle pores; (e) bubble-like pores, slit-like pores, and pyrite framboids; (f) showing some of the measured pore diameters.

Figure 5.2 shows the SEM analyses of the Haynesville Shale sample. Intraparticle pores and fractures are observed in Figure 5.2a, and diameters of intraparticle pores are about 40–70 nm.

Figure 5.2b shows pore throats, bubble-like pores, and slit-like pores. The openings of pore throats and slit-like pores are about 20–110 nm, and 20–70 nm, respectively (Figure 5.2c). The bubble-like pores have an opening about 50–200 nm (Figure 5.2c). Figure 5.2d shows the fractures, pyrite framboids, and intraparticle pores, whose openings are about 130–350 nm. Intraparticle and interparticle pores, slit-like pores, and pore throats are observed in Figure 5.2e and 5.2g. The openings of interparticle and intraparticle pores are about 100–130 nm and 40–80 nm, respectively (Figure 5.2f). Moreover, slit-like pores, and pore throats have an opening of 20–70 nm, and 80–180 nm, respectively. Pyrite framboids and fractures are observable in Figure 5.2h. Figure 5.2i also shows slit-like pores, and intraparticle pores, and their opening are about 30–90 nm, and 50–90 nm, respectively (Figure 5.2j). Figures 5.2k and 5.2l present more detailed information about the existing pore throats and OM pores between pyrite framboids.
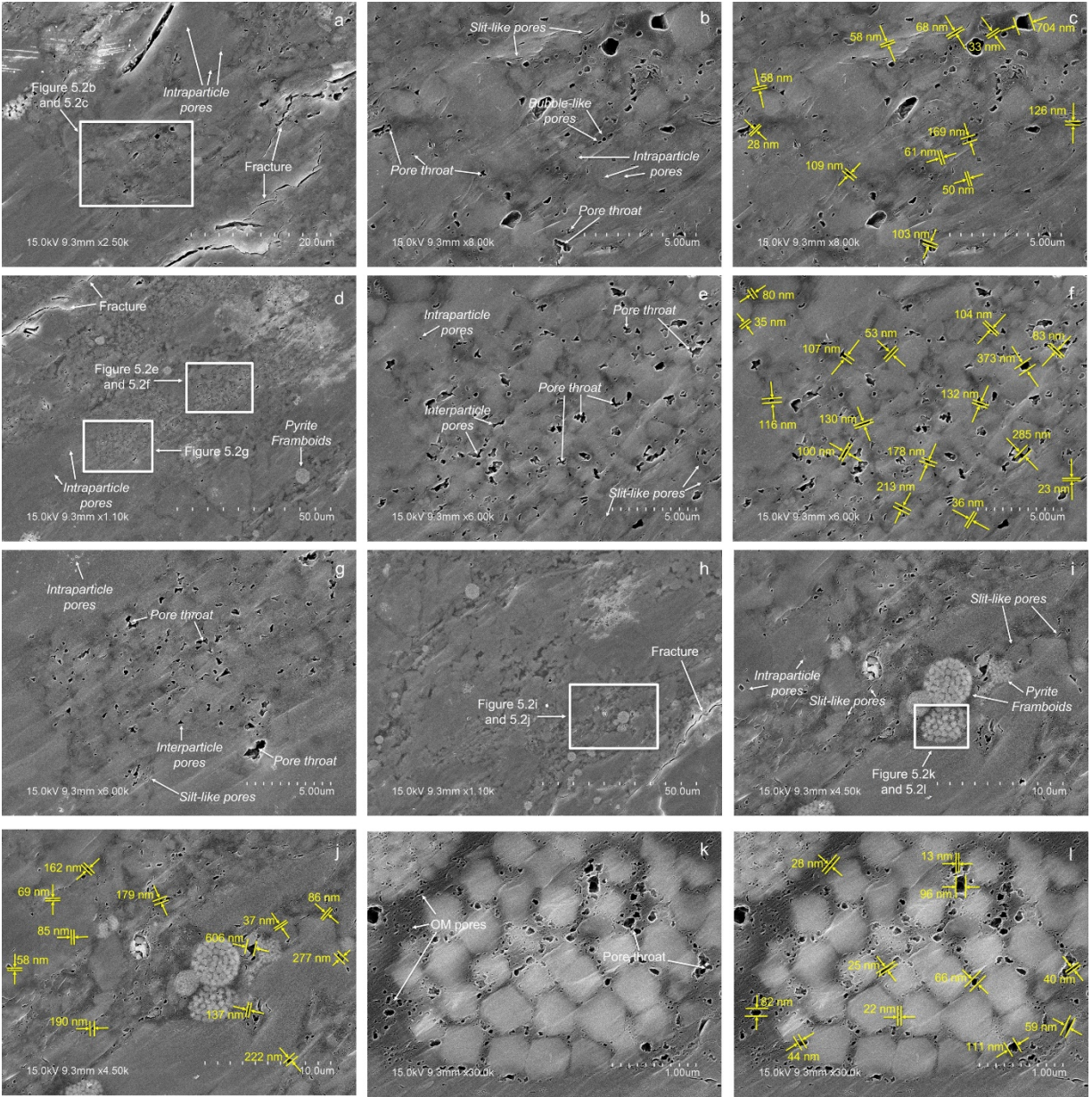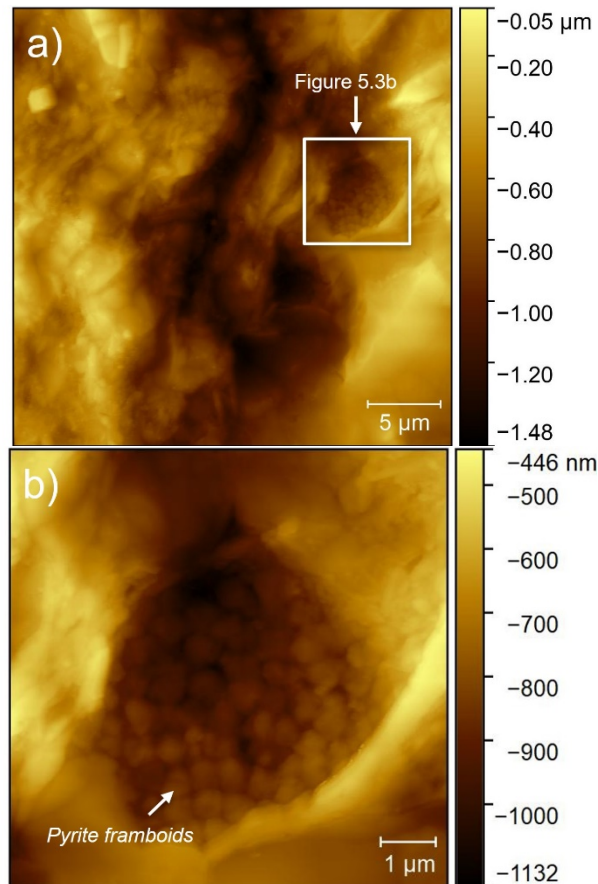
Figure 5.2. SEM images for a Haynesville Shale sample; (a) wider region of the 2b and 2c images, fractures, intraparticle pores; (b) intraparticle pores, pore throats, and slit-like pores; (c) some of the measured pore diameters; (d) wider region of 5.2e,f and g, fractures, and intraparticle pores; (e) intraparticle pores, slit-like pores, and pore throats; (f) some of the measured pore diameters; (g) intraparticle pores, pore throats, interparticle pores, and slit-like

pores; (h) wider region of 2h and 2i, and fractures (i) wider region of 2j and 2k, intraparticle

pores, slit-like pores, and pyrite framboids; (j) some of the measured pore diameters; (k) pyrite

framboids, OM pores, and pore throat; and (l)some of the measured pore diameters.

5.2.2 Results from AFM analyses

The surface morphology of the samples was identified by the AFM experiments, where the

color bar in the 2-D maps shows the height difference (Figures 5.3-5.7). Pyrite framboids (Figure

5.3b), and bubble-like pores (Figure 5.3d) are detected. Four topography profiles are presented for

Bossier Shale sample (Figure 5.4c-f) and Haynesville Shale sample (Figure 5.5c-f). The pores were

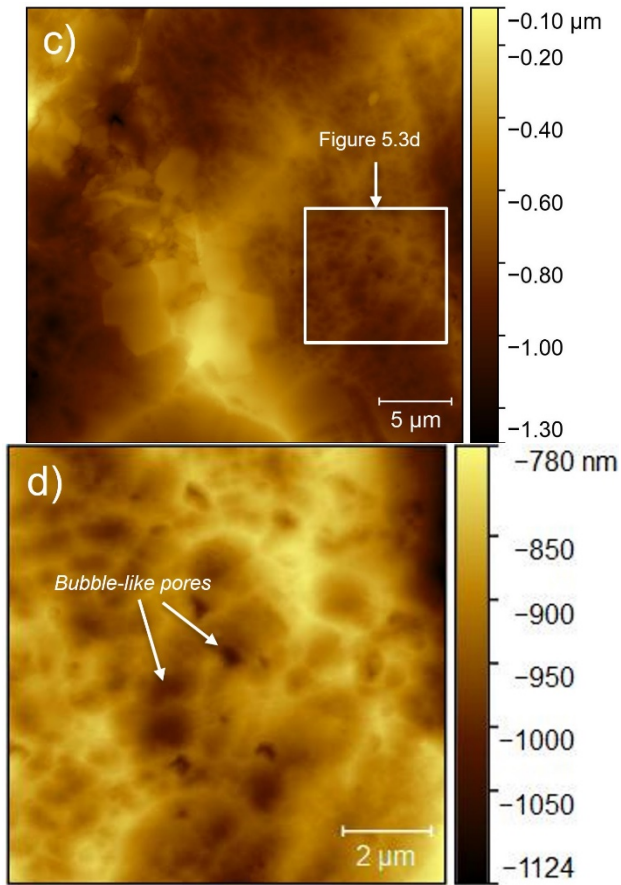identified using the watershed method for Bossier Shale (Figure 5.6a-d), and Haynesville Shale

(Figure 5.7a-d).

Figure 5.3. AFM images for Bossier (4a-b) and Haynesville (4c-d) Shale samples, where (a) and (c) are wider region of the 4b and 4c. Pyrite framboids are observed in 4b and bubble-like pores are found in 4d.

In Figures 5a and 6a, the chromaticity in the two-dimensional surface topography maps shows the height of the surface. The three-dimensional maps are shown in Figures 5b and 6b. A comparison of the topography profiles of Bossier and Haynesville Shale samples shows that surface height changes more in Bossier Shale than Haynesville Shale.

a)

b)

c)
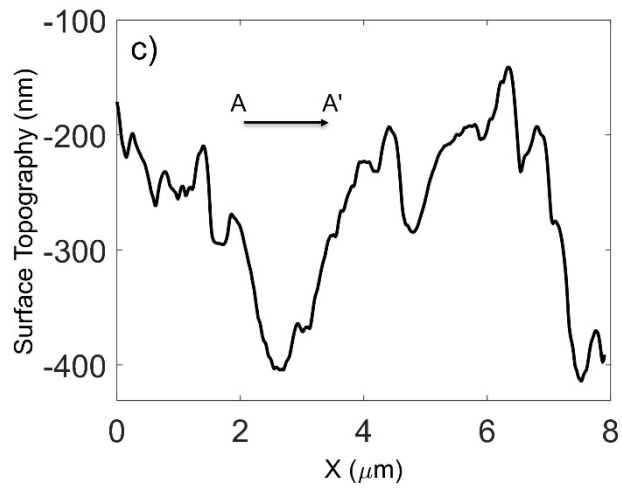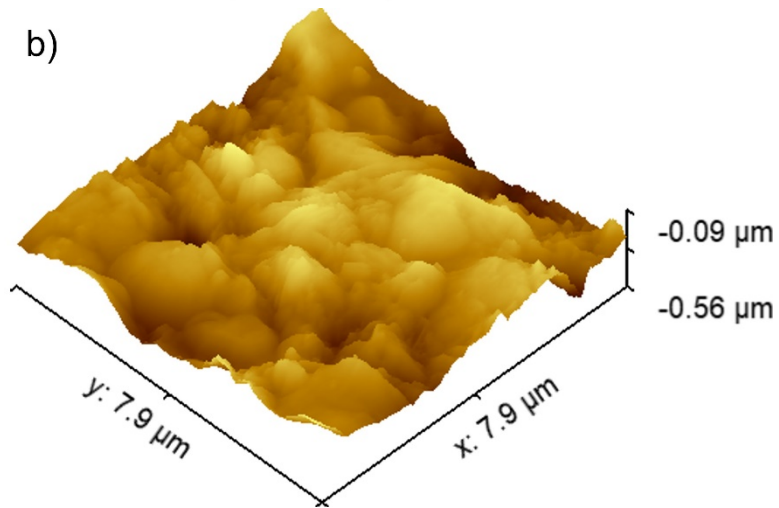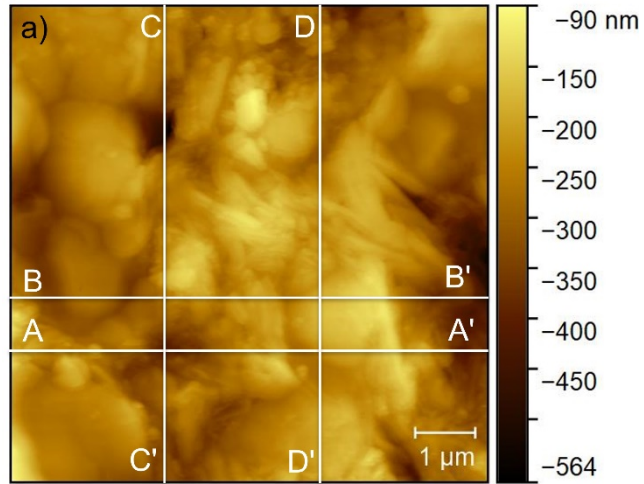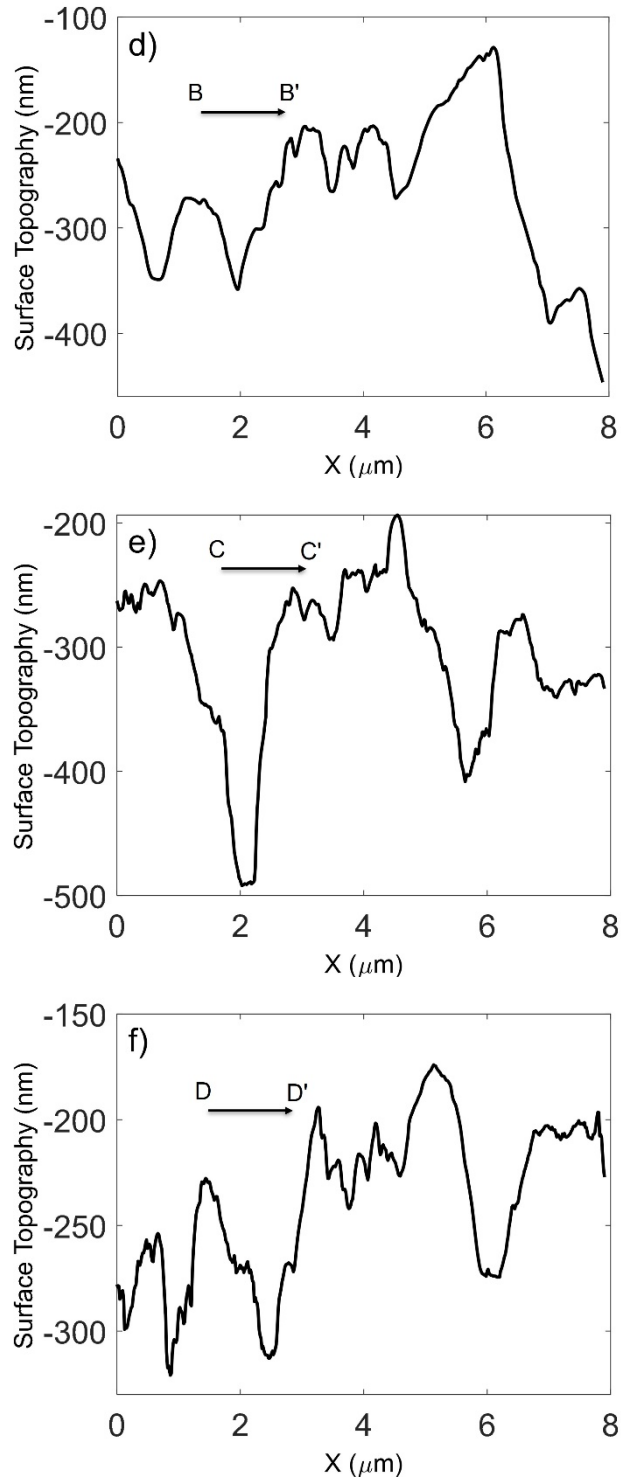
Figure 5.4. AFM images and section analyses for a Bossier Shale sample: (a) 2-D and 3-D images (5.4a, and 5.4b); (5.4c-f) section analyses of 2-D image along four different profiles
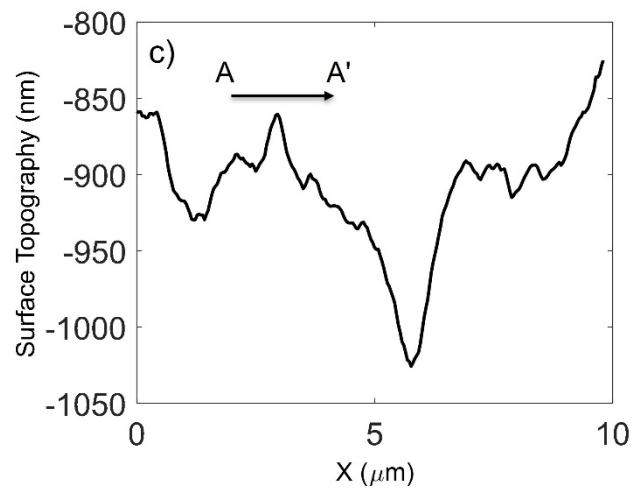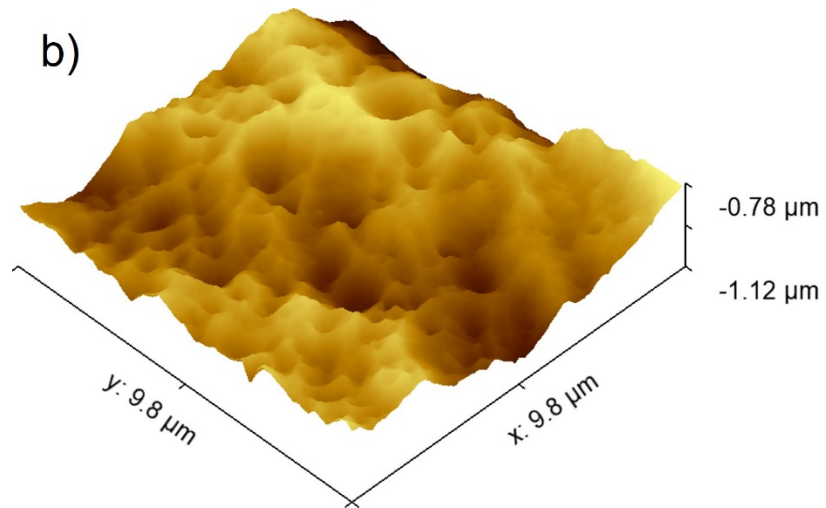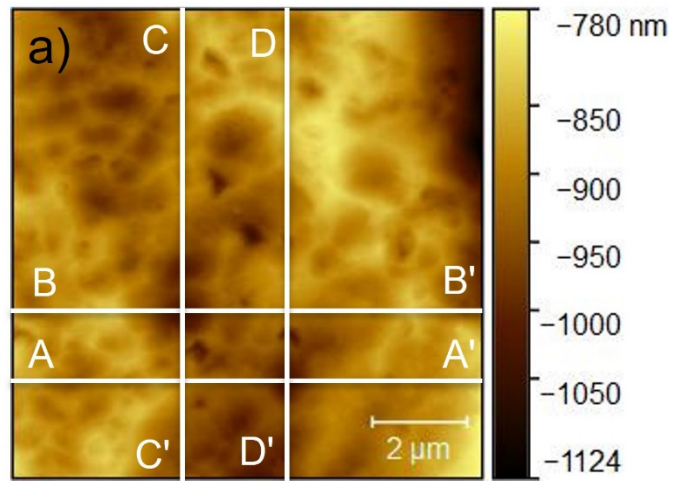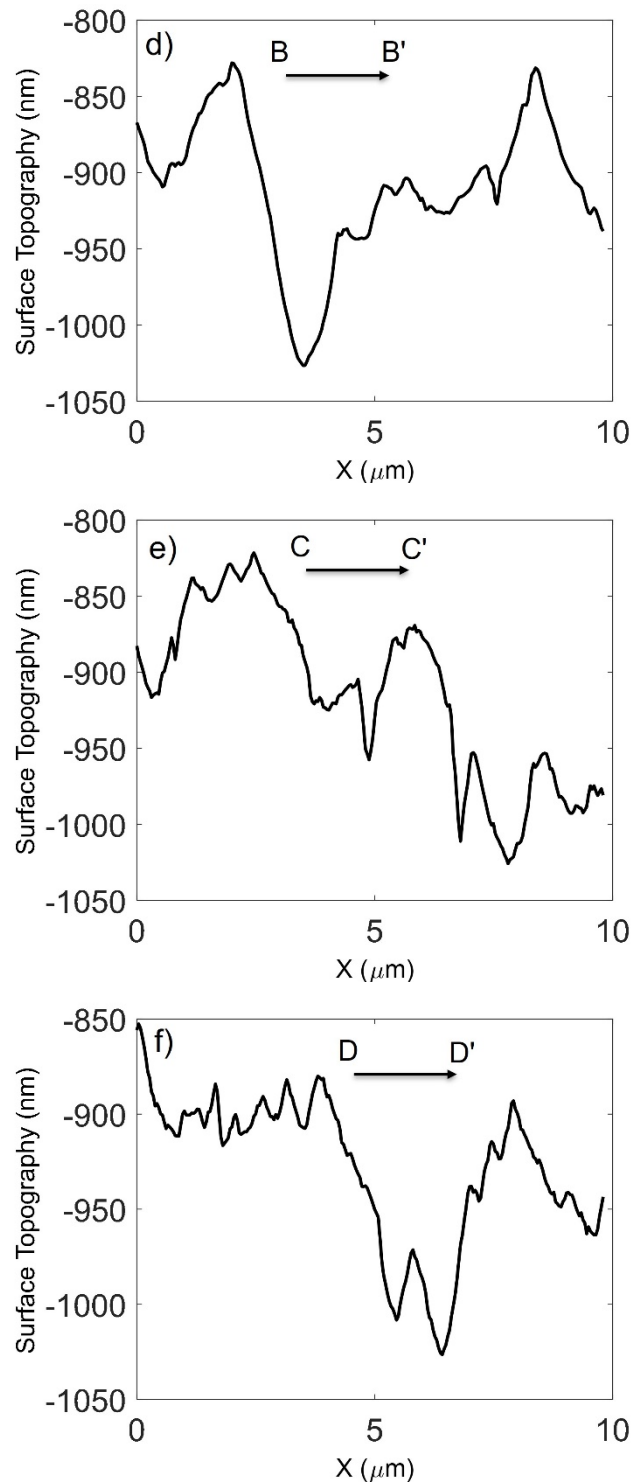
Figure 5.5. AFM images and section analyses for Haynesville Shale sample: (a) 2-D and 3-D

images (5.5a, and 5.5b); (5.5c-f) section analyses of 2-D image along four different profiles

Figure 5.6 shows the identified pores in Bossier Shale sample, and different types of pores are identified including slit-like pores, pore throats, intra-particle pores. Figure 5.7 shows the identified pores in Haynesville Shale sample, and different types of identified pores are slit-like pores, intra-particle pores, pore throats, and bubble-like pores.
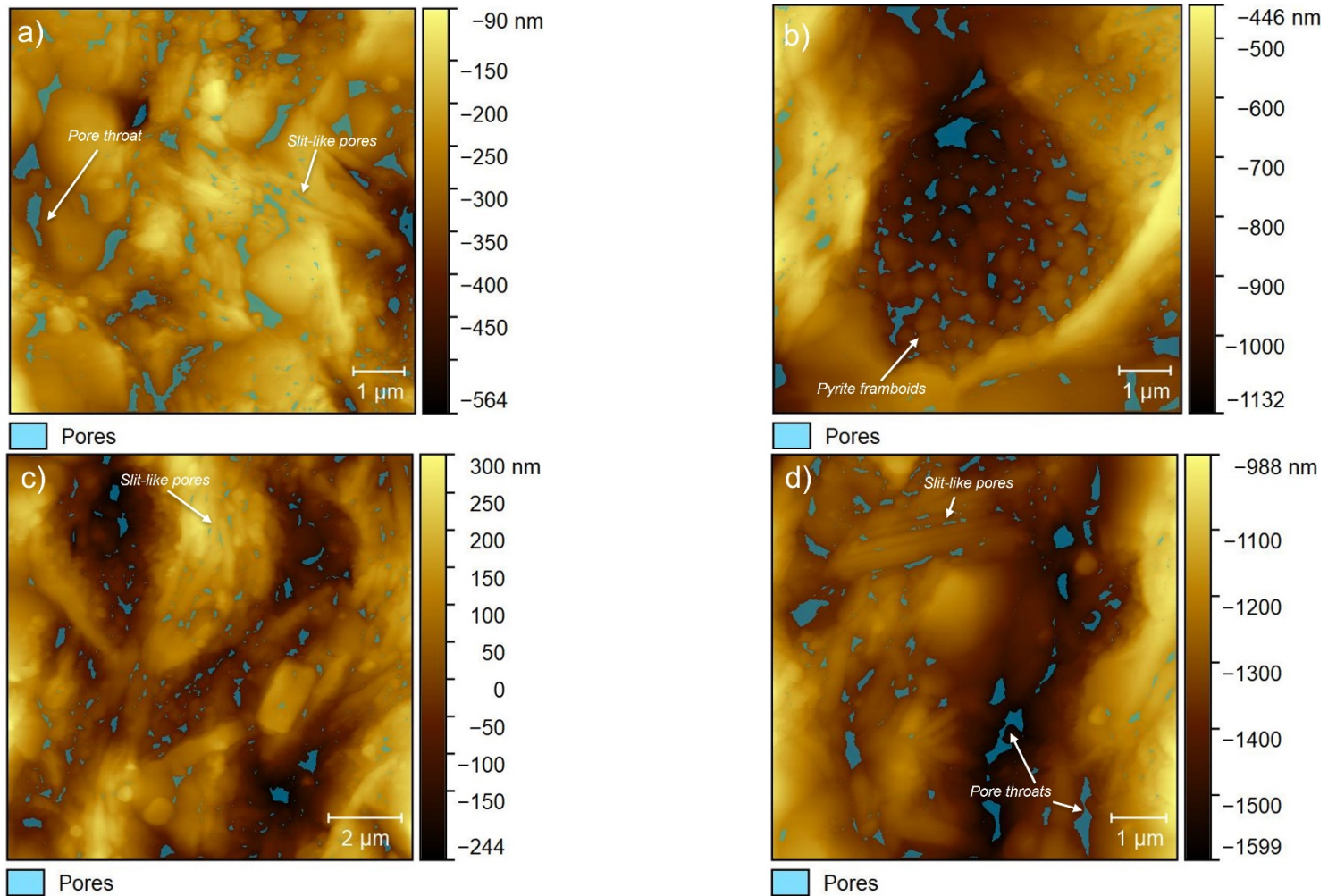
Figure 5.6. Pores marked by the watershed method for Bossier Shale sample with slit-like pores and pore throats (5.6a, 5.6c, and 5.6d) as well as pyrite framboids (5.6b).
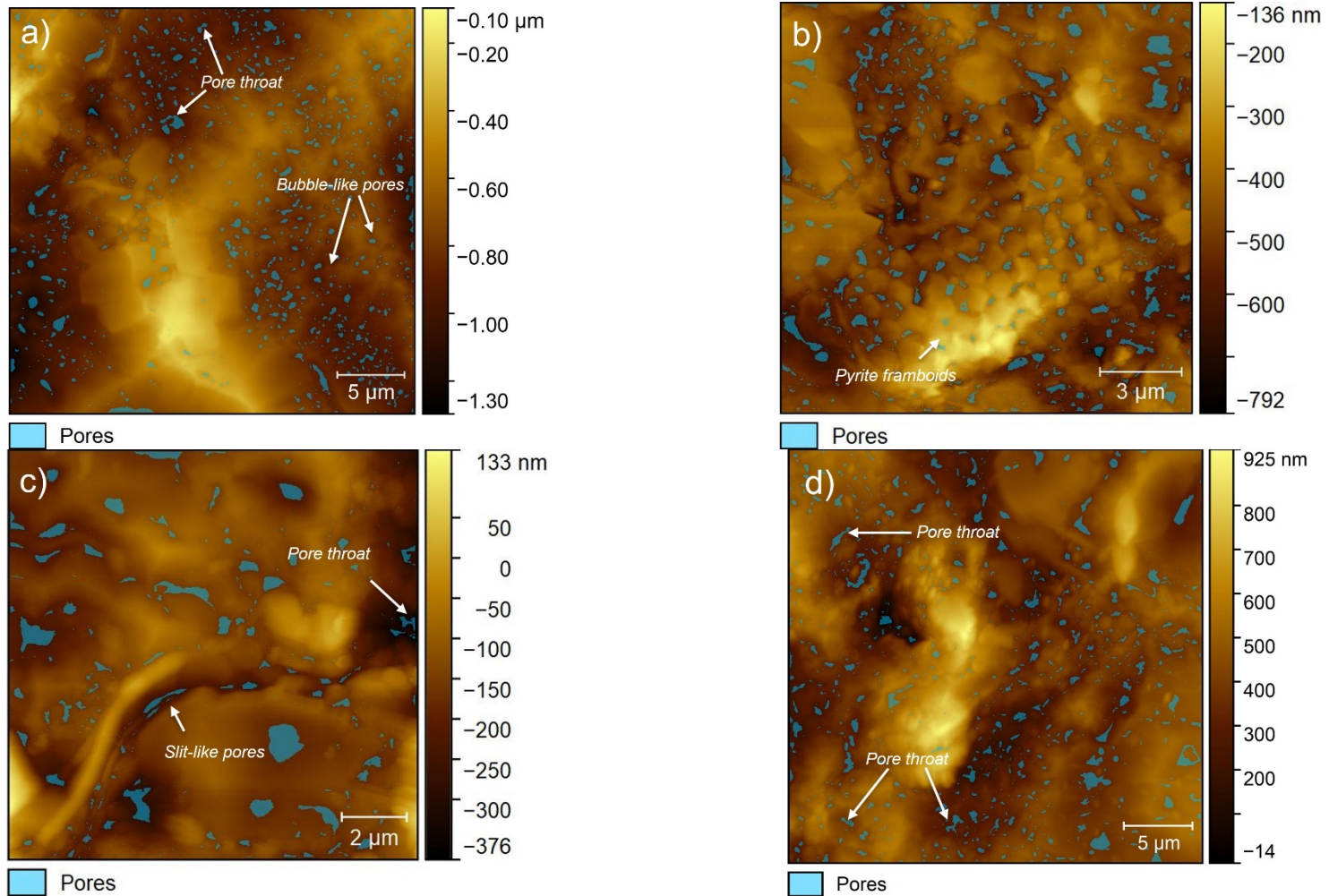
Figure 5.7. Pores marked by the watershed method for Haynesville Shale sample, with pore throats (5.7a, 5.7c, and 5.7d), slit-like pores (5.7c), bubble-like pores (5.7a), and pyrite framboids (5.7b).

5.3 Discussion

Statistical analyses were conducted on the measured diameter (D) and projected area (A) of the pores, and the best fitted distribution were found for each data. Figure 5.8 shows both the histogram and probability density function (pdf) of the best fitted distribution to all the measured pore diameters in the Bossier (Figure 5.8a-b) and Haynesville (Figure 5.8c-d) Shale samples. This figure shows the statistical analyses for measurements with both SEM (Figure 5.8a and -c) and AFM (Figure 5.8b and d). From the histograms, the pore diameters are rightly skewed. The best fitted distribution is a Lognormal distribution ($LN(\mu, \sigma)$), where μ and σ are the mean and standard deviation of the natural logarithm of the measured pore diameters, respectively. For the measured pore diameters with SEM images, the μ and σ for the Bossier Shale sample are 3.4050 and 0.5768, respectively. the corresponding values of μ and σ for the Haynesville Shale sample are 4.0761 and 0.8198.
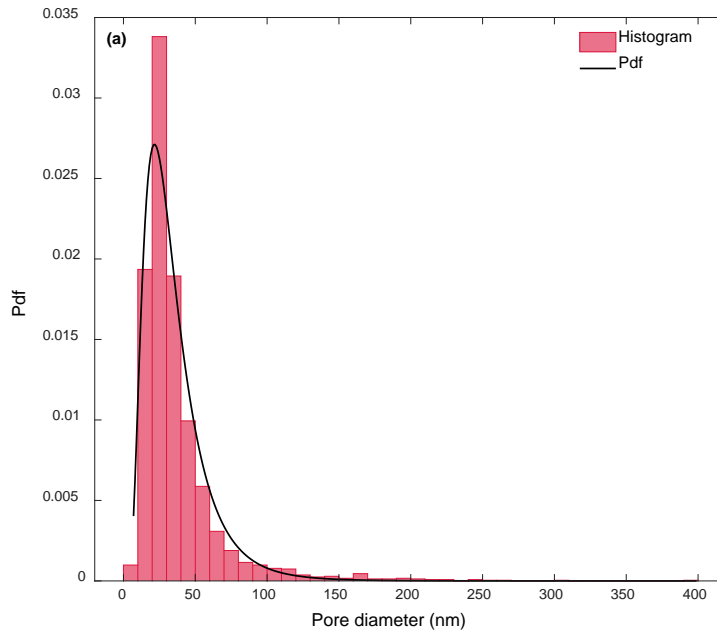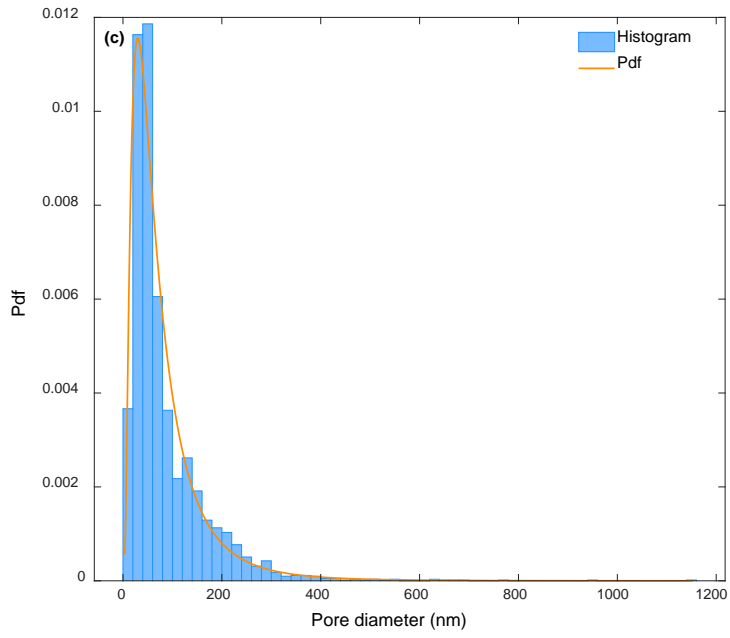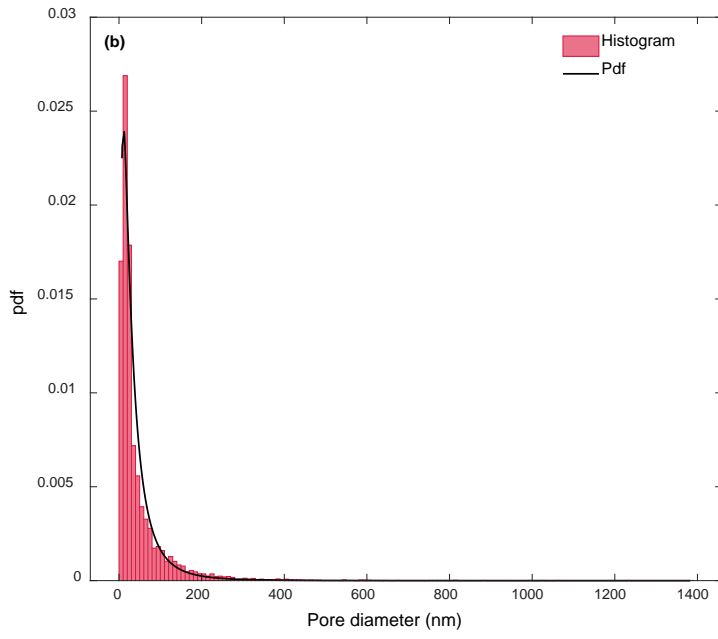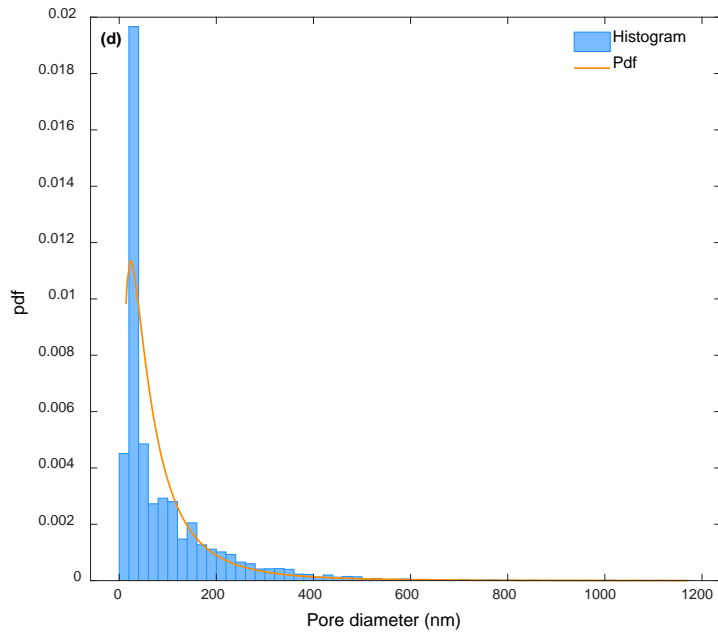
Figure 5.8. Histogram and probability density function (pdf) for Bossier (a-b) and Haynesville (cd) Shale samples: (a) and (c) are measured with SEM, while (b) and (d) are measured with AFM.
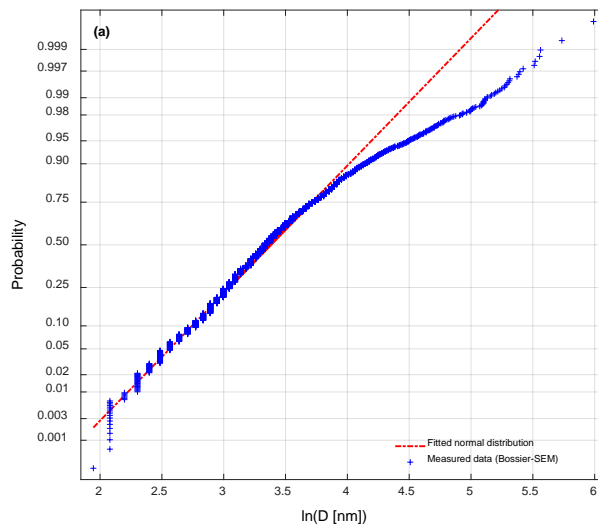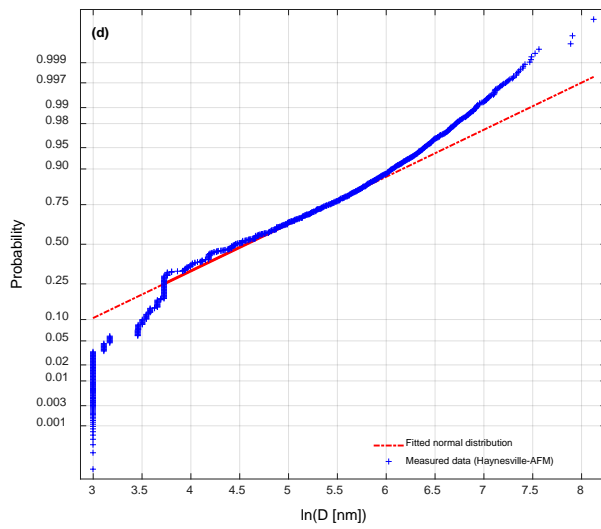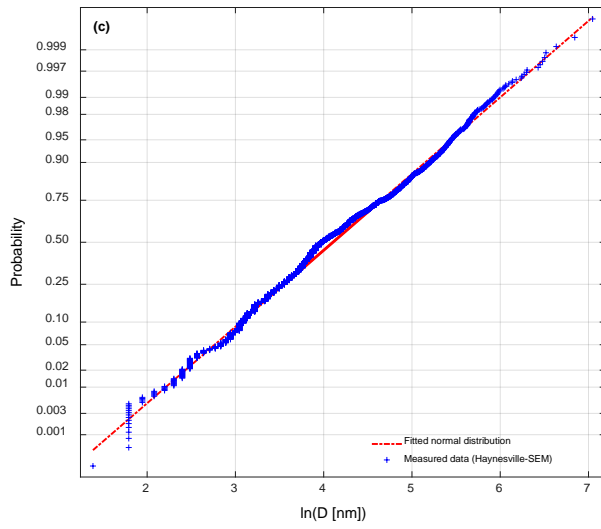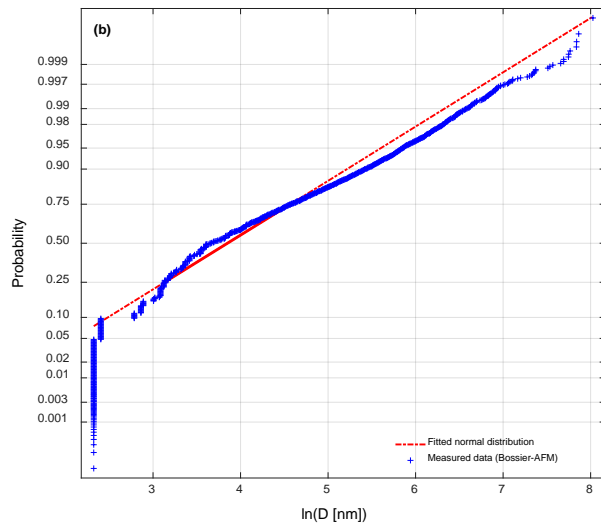
Figure 5.9. Normal probability plot for the measured pore diameters for Bossier (a-b) and Haynesville (c-d) Shale samples: (a) and (c) are measured with SEM while (b) and (d) are measured with AFM.

Comparing the histogram and the pdf of the fitted lognormal distribution shows that the lognormal distribution is fitted to the measured pore diameter of the Haynesville Shale more than the Bossier Shale (Figure 5.8a and c). Figure 5.9 shows the normal probability plot of the natural logarithm of the measured pore diameters for the Bossier Shale (Figure 5.9a-b) and Haynesville Shale (Figure 5.9c-d) samples. These normal probability plots confirm that the measured pore diameters of the Haynesville Shale sample follows more a log-normal distribution than the Bossier Shale sample.

88
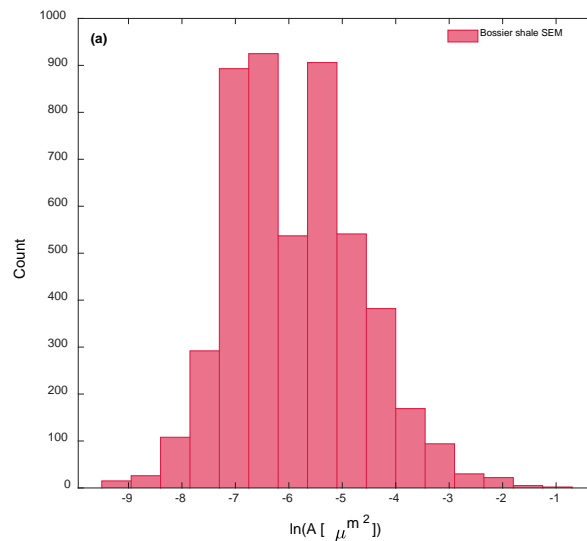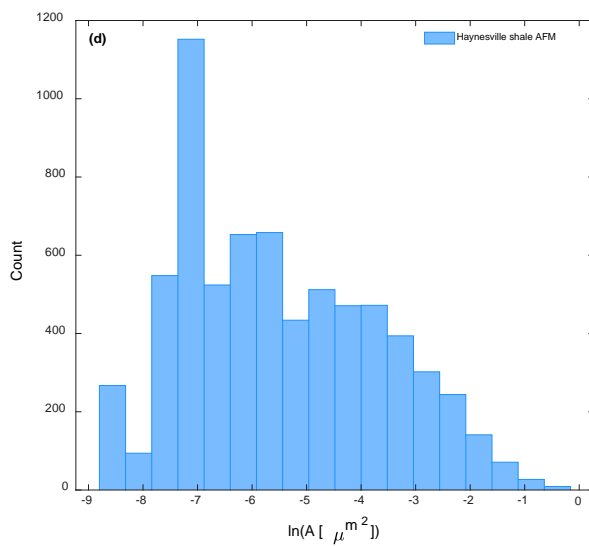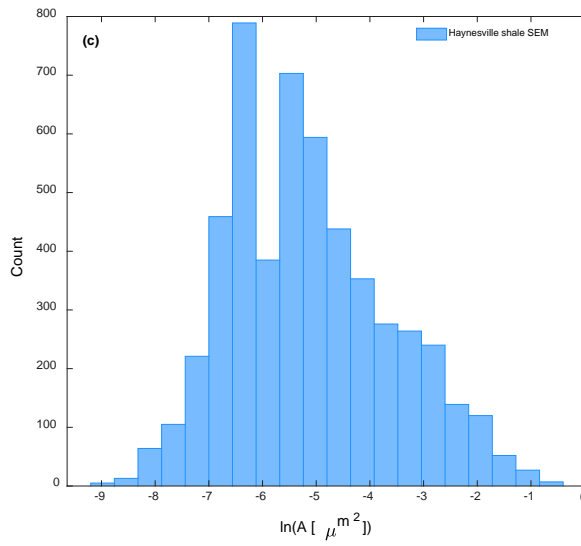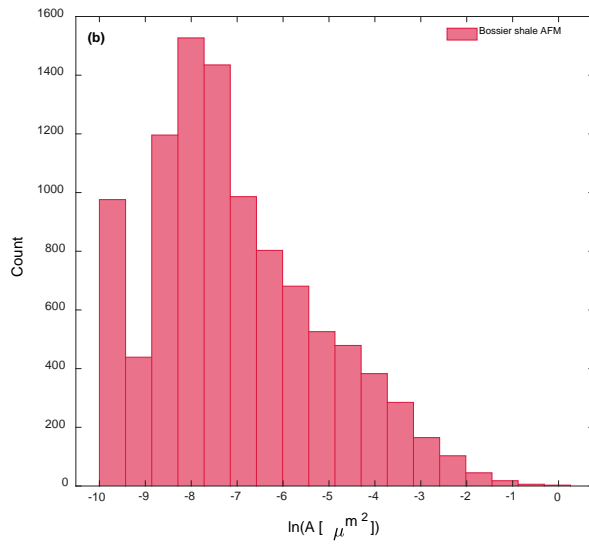
Figure 5.10. Histogram of the $ln(A \, [\mu m^2])$, where A is the measured projected area for Bossier

(a-b) and Haynesville (c-d) Shale samples: (a) and (c) are measured with SEM, while (b) and

(d) are measured with AFM.

Figure 5.10 shows the histogram of natural logarithm of the measured projection areas

$ln(A \, [\mu m^2])$ in Bossier (Figure 5.10a-b), and Haynesville Shale samples (Figure 5.10c-d). This

figure shows the statistical analysis for measurements with both SEM (Figure 5.10a and c) and

AFM (Figure 5.10b and d). From the histograms it is clear that $ln(A)$ from SEM measurements

(Figure 5.10a and c) has a near-normal distribution for both Bossier and Haynesville Shale

samples, so the projected area from SEM measurements has roughly a log-normal distribution. On

the other hand, the histogram of $ln(A)$ from AFM measurements (Figure 5.10b and d) are still

rightly skewed. The μ and σ for the Bossier Shale sample are 5.5976 and 1.1091; as a comparison,

the μ and σ for the Haynesville shale sample are -5.1240 and 1.5024.
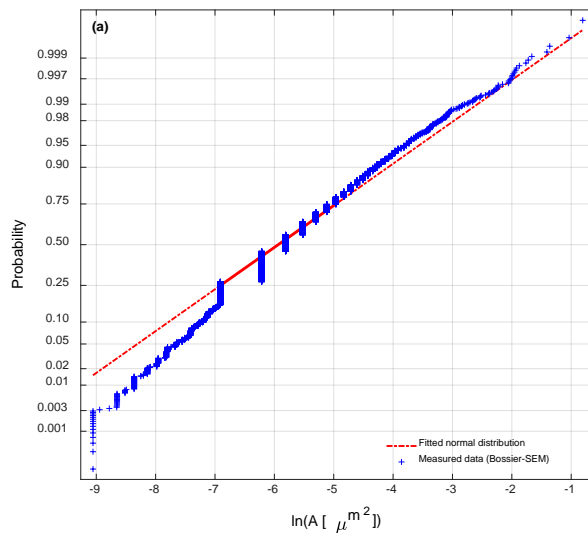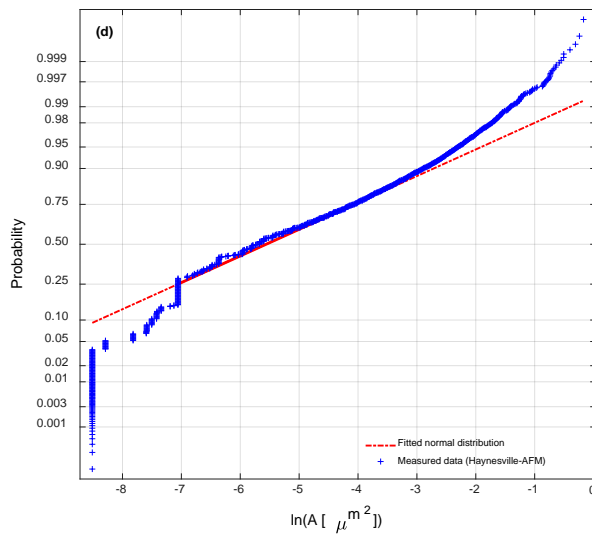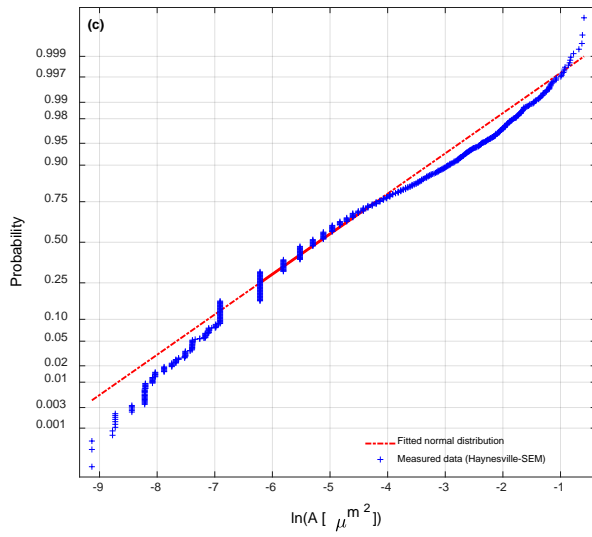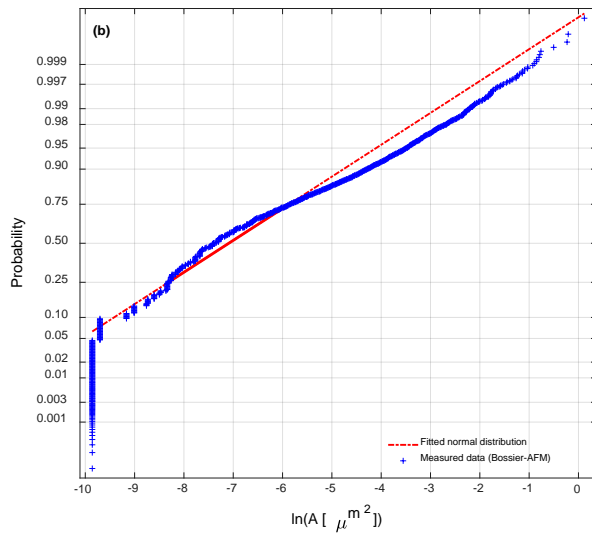
Figure 5.11. Normal probability plot for the $ln(A\ [\mu m^2])$ for Bossier (a, b) and Haynesville (c, d) Shale samples. Note that 5.11.(a) and (c) are measured with the SEM while 5.11. (b) and (d) are measured with AFM.

Figure 5.11 shows the normal probability plot of the natural logarithm of the measured projection areas for the Bossier Shale (Figure 5.11a-b) and Haynesville Shale (Figure 5.11c-d) samples. These normal probability plots of the SEM measurements (Figures 5.11a and c) confirm that the best fitted distribution to measured projected areas with SEM is a log-normal distribution. On the other hand, the normal probability plots of the AFM measurements (Figures 5.11b and d) confirms that the $ln(A\ [\mu m^2])$ for the AFM measurements are rightly skewed.

SEM observations of the Haynesville Shale samples show the presence of narrow slit-like pores (Figures 5.2b, e, and i), which is consistent with the results from Wang et al. (2021) on the same samples. Wang et al. (2021) conducted the physisorption isotherm classification on the Haynesville Shale samples and inferred that narrow slit-like pores existed in the Haynesville Shale samples. From both SEM and AFM measurements, most of the measured pores have a diameter of roughly less than 50 nm (Figure 5.8), which is also consistent with the findings of Wang et al. (2021).

Chapter 6: Conclusions

The first half of this dissertation discusses the current understanding of the major mechanical properties of OM-rich shales with respect to their chemical properties such as TOC content, maturity level, and mineralogy. The other important aspect of investigating the geomechanical properties is the experimental conditions such as temperature, or if the experiments were conducted under the *in situ* stress conditions. Nanoscale to microscale experiments on shale samples need a much smaller sample sizes compared to conventional and macroscale experiments, and this is a huge advantage. One main shortcoming of nanoindentation and AFM approaches is that both methods measure the mechanical properties very close to the sample surface; however, the constituents of OM-rich shales have small sizes in micrometer and nanometer. Nanoindentation- and AFM-based methods result in a classification of mechanical phases (each mechanical phase is the group of minerals/components that have the same mechanical property such as Young's modulus) in OM-rich shales: Group I for the softest components (Young's modulus of 0-25 GPa); 2) Group II for clay minerals with average Young's modulus of $\sim 29\ GPa$; Group III for isolated grains, which are mainly carbonate minerals, with average Young's modulus of $\sim 58\ GPa$; and Group IV for stiff minerals (mainly feldspars, quartz, and pyrite) with a mean value of Young's modulus of higher than $90\ GPa$. It is found that the OM is the most compliant compound in OM-rich shales. Furthermore, it is impossible to apply conventional experiments of rock mechanics (Uniaxial Compressive Strength test, Triaxial Compressive Strength test, etc.) on the OM which is embedded within shales. Overall, the Force-Distance curve, and LFM experiments on OM results the following:

1) The histogram shows two mechanical phases in the measured Young's modulus. Phase one has Young's modulus of less than 5 *GPa* or slightly higher than 5 *GPa*, and phase two has Young's modulus of 10 *GPa* or higher.

2) Although some local stick-slip events observed in experiments (Figure 4.8), no dominant stick-slip motion was observed.

3) There was a nonlinear relationship between the friction force and normal load, and the Hertz-plus offset model is the best theoretical model to investigate load-dependency of friction.

SEM observations of Haynesville Shale samples show an existence of narrow slit-like pores, which is consistent with the results from AFM measurements. Moreover, these observations are in agreement with the previously published work which classified the pore spaces of Haynesville Shale samples using physisorption isotherm classification. Both SEM and AFM measurements illustrate that most of the measured pores have a diameter of roughly less than 50 nm. The statistical analyses of the measured pore diameters of Haynesville and Bossier Shale samples find that the lognormal distribution is the best distribution, and data from Haynesville Shale sample is fitted to lognormal distribution better than Bossier Shale sample. The results from projected area measurements of Bossier Shale samples showed that lognormal distribution is roughly fitted to the SEM measurements, but the results from AFM measurements are still highly skewed to the right.

Based on the current findings of this research the following recommendations are made for improving the mechanical characterization and pore space characterization of OM rich shales:

1) Apply molecular simulation to simulate the lateral force microscopy experiment of OM and compare the findings of simulations with this research. This will provide more detailed analysis of frictional properties of OM.

2) Investigate the possibility of having the fractal behavior for pore space size.

References:

Abousleiman, Y. N., Hull, K. L., Han, Y., Al-Muntasheri, G., Hosemann, P., Parker, S., & Howard, C. B. (2016). The granular and polymer composite nature of kerogen-rich shale. *Acta Geotechnica*, *11*(3), 573–594. https://doi.org/10.1007/s11440-016-0435-y.

Ago, M., Jakes, J. E., & Rojas, O. J. (2013). Thermomechanical properties of lignin-based electrospun nanofibers and films reinforced with cellulose nanocrystals: A dynamic mechanical and nanoindentation study. *ACS Applied Materials & Interfaces*, *5*(22), 11768– 11776. https://doi.org/10.1021/am403451w.

Ahmadov, R. S. O. (2011). Microtextural, Elastic and Transport Properties of Source Rocks [Stanford University]. In *ProQuest Dissertations and Theses*. https://login.ezproxy.uta.edu/login?url=https://www.proquest.com/dissertations-theses/microtextural-elastic-transport-properties-source/docview/2454191154/se-2?accountid=7117.

Anovitz, L. M., & Cole, D. R. (2015). Characterization and analysis of porosity and pore structures. *Reviews in Mineralogy and Geochemistry*, *80*(1), 61–164. https://doi.org/10.2138/rmg.2015.80.04.

Anyanwu, J. 2015. Nano-Petrophysics Characterization of Bakken Formation of the Willison Basin, North Dakota. *Master's Thesis, the University of Texas at Arlington*, 77 pp.

Ashraf, W., & Tian, N. (2016). Nanoindentation assisted investigation on the viscoelastic behavior of carbonated cementitious matrix: Influence of loading function. *Construction and Building Materials*, *127*, 904–917. https://doi.org/https://doi.org/10.1016/j.conbuildmat.2016.10.021.

Bennett, K. C., Berla, L. A., Nix, W. D., & Borja, R. I. (2015). Instrumented nanoindentation and

3D mechanistic modeling of a shale at multiple scales. *Acta Geotechnica*, *10*(1), 1–14. https://doi.org/10.1007/s11440-014-0363-7.

Beuwer, M. A., Knopper, M. F., Albertazzi, L., van der Zwaag, D., Ellenbroek, W. G., Meijer, E. W., Prins, M. W. J., & Zijlstra, P. (2016). Mechanical properties of single supramolecular polymers from correlative AFM and fluorescence microscopy. *Polymer Chemistry*, *7*(47), 7260–7268. https://doi.org/https://doi.org/10.1039/c6py01656a.

Binnig, G., Quate, C. F., & Gerber, C. (1986). Atomic force microscope. *Physical Review Letters*, *56*(9), 930–933. https://doi.org/10.1103/PhysRevLett.56.930

Binnig, G., Rohrer, H., Gerber, C., & Weibel, E. (1982). Surface studies by scanning tunneling microscopy. *Physical Review Letters*, *49*(1), 57–61. https://doi.org/10.1103/PhysRevLett.49.57.

Cai, T., Feng, Z., & Zhou, D. (2018). Multi-scale characteristics of coal structure by x-ray computed tomography (x-ray CT), scanning electron microscope (SEM) and mercury intrusion porosimetry (MIP) . In *AIP advances* (Vol. 8, Issue 2, pp. 25312–25324). Amer Inst Physics . https://doi.org/10.1063/1.5021699.

Cao, T., Song, Z., Wang, S., Cao, X., Li, Y., & Xia, J. (2015). Characterizing the pore structure in the Silurian and Permian shales of the Sichuan Basin, China. *Marine and Petroleum Geology*, *61*, 140–150. https://doi.org/https://doi.org/10.1016/j.marpetgeo.2014.12.007.

Castagna, J. P., Batzle, M. L., & Eastwood, R. L. (1985). Relationships between compressional-wave and shear-wave velocities in clastic silicate rocks. *Geophysics*, *50*(4), 571–581. https://doi.org/10.1190/1.1441933.

Chen, Q., Zhang, J., Tang, X., Li, W., & Li, Z. (2016). Relationship between pore type and pore

size of marine shale: An example from the Sinian–Cambrian formation, upper Yangtze region, South China. *International Journal of Coal Geology*, *158*, 13–28. https://doi.org/https://doi.org/10.1016/j.coal.2016.03.001.

Chen, S., Li, X., Chen, S., Wang, Y., Gong, Z., & Zhang, Y. (2021). A new application of atomic force microscopy in the characterization of pore structure and pore contribution in shale gas reservoirs. *Journal of Natural Gas Science and Engineering*, *88*, 103802. https://doi.org/https://doi.org/10.1016/j.jngse.2021.103802.

Chen, S., Tao, S., Tang, D., Xu, H., Li, S., Zhao, J., Jiang, Q., & Yang, H. (2017). Pore structure characterization of different rank coals using N_2 and CO_2 adsorption and its effect on CH_4 adsorption capacity: A case in Panguan Syncline, Western Guizhou, China. *Energy & Fuels*, *31*(6), 6034–6044. https://doi.org/10.1021/acs.energyfuels.7b00675.

Cheng, Y.-T., Li, Z., & Cheng, C.-M. (2002). Scaling relationships for indentation measurements. *Philosophical Magazine A*, *82*(10), 1821–1829. https://doi.org/10.1080/01418610208235693.

Clarkson, C. R., Freeman, M., He, L., Agamalian, M., Melnichenko, Y. B., Mastalerz, M., Bustin, R. M., Radliński, A. P., & Blach, T. P. (2012). Characterization of tight gas reservoir pore structure using USANS/SANS and gas adsorption analysis. *Fuel*, *95*, 371–385. https://doi.org/https://doi.org/10.1016/j.fuel.2011.12.010.

Clarkson, C. R., Jensen, J. L., & Chipperfield, S. (2012). Unconventional gas reservoir evaluation: What do we have to consider? *Journal of Natural Gas Science and Engineering*, *8*, 9–33. https://doi.org/https://doi.org/10.1016/j.jngse.2012.01.001.

Clarkson, C. R., Solano, N., Bustin, R. M., Bustin, A. M. M., Chalmers, G. R. L., He, L.,

Melnichenko, Y. B., Radliński, A. P., & Blach, T. P. (2013). Pore structure characterization of North American shale gas reservoirs using USANS/SANS, gas adsorption, and mercury intrusion. *Fuel*, *103*, 606–616. https://doi.org/https://doi.org/10.1016/j.fuel.2012.06.119.

Constantinides, G., Ravi Chandran, K. S., Ulm, F.-J., & Van Vliet, K. J. (2006). Grid indentation analysis of composite microstructure and mechanics: Principles and validation. *Materials Science and Engineering: A*, *430*(1), 189–202. https://doi.org/https://doi.org/10.1016/j.msea.2006.05.125.

Cornet, F. H. (2015). *Elements of Crustal Geomechanics*. Cambridge University Press. https://doi.org/DOI: 10.1017/CBO9781139034050.

Curtis, M. E., Sondergeld, C. H., Ambrose, R. J., & Rai, C. S. (2012). Microstructural investigation of gas shales in two and three dimensions using nanometer-scale resolution imaging. *AAPG Bulletin*, *96*(4), 665–677. https://doi.org/10.1306/08151110188.

Dazzi, A., Glotin, F., & Carminati, R. (2010). Theory of infrared nanospectroscopy by photothermal induced resonance. *Journal of Applied Physics*, *107*(12), 124519. https://doi.org/10.1063/1.3429214.

Dazzi, A., & Prater, C. B. (2017). AFM-IR: Technology and applications in nanoscale infrared spectroscopy and chemical imaging. *Chemical Reviews*, *117*(7), 5146–5173. https://doi.org/10.1021/acs.chemrev.6b00448.

Dazzi, A., Prater, C. B., Hu, Q., Chase, D. B., Rabolt, J. F., & Marcott, C. (2012). AFM-IR: Combining atomic force microscopy and infrared spectroscopy for nanoscale chemical characterization. *Applied Spectroscopy*, *66*(12), 1365–1384. https://doi.org/10.1366/12-06804.

Deirieh, A., Ortega, J. A., Ulm, F.-J., & Abousleiman, Y. (2012). Nanochemomechanical assessment of shale: a coupled WDS-indentation analysis. *Acta Geotechnica*, *7*(4), 271–295. https://doi.org/10.1007/s11440-012-0185-4.

Dewhurst, D. N., Siggins, A. F., Sarout, J., Raven, M. D., & Nordgård-Bolås, H. M. (2011). Geomechanical and ultrasonic characterization of a Norwegian Sea shale. *Geophysics*, *76*(3), WA101–WA111. https://doi.org/10.1190/1.3569599.

Di Maio, D., & Roberts, S. G. (2005). Measuring fracture toughness of coatings using focused-ion-beam-machined microbeams. *Journal of Materials Research*, *20*(2), 299–302. https://doi.org/DOI: 10.1557/JMR.2005.0048.

Dufrêne, Y. F., Ando, T., Garcia, R., Alsteens, D., Martinez-Martin, D., Engel, A., Gerber, C., & Müller, D. J. (2017). Imaging modes of atomic force microscopy for application in molecular and cell biology. *Nature Nanotechnology*, *12*(4), 295–307. https://doi.org/10.1038/nnano.2017.45.

Eichmann, S. L., Jacobi, D., Haque, M. H., & Burnham, N. A. (2018). Non-destructive investigations of thermal maturity and mechanical properties of source rocks. *Journal of Petroleum Geology*, *41*(4), 421–446. https://doi.org/10.1111/jpg.12715.

Eissa, E. A., & Kazi, A. (1988). Relation between static and dynamic Young's moduli of rocks. *International Journal of Rock Mechanics and Mining Sciences & Geomechanics Abstracts*, *25*(6), 479–482. https://doi.org/https://doi.org/10.1016/0148-9062(88)90987-4.

Eliyahu, M., Emmanuel, S., Day-Stirrat, R. J., & Macaulay, C. I. (2015). Mechanical properties of organic matter in shales mapped at the nanometer scale. *Marine and Petroleum Geology*, *59*, 294–304. https://doi.org/https://doi.org/10.1016/j.marpetgeo.2014.09.007.

Emmanuel, S., Eliyahu, M., Day-Stirrat, R. J., Hofmann, R., & Macaulay, C. I. (2016a). Impact of thermal maturation on nano-scale elastic properties of organic matter in shales. *Marine and Petroleum Geology*, *70*, 175–184. https://doi.org/https://doi.org/10.1016/j.marpetgeo.2015.12.001.

Emmanuel, S., Eliyahu, M., Day-Stirrat, R. J., Hofmann, R., & Macaulay, C. I. (2016b). Softening of organic matter in shales at reservoir temperatures. *Petroleum Geoscience*, *23*(2), 262–269. https://doi.org/10.1144/petgeo2016-035.

Erdman, N., & Drenzek, N. (2013). Integrated Preparation and Imaging Techniques for the Microstructural and Geochemical Characterization of Shale by Scanning Electron Microscopy. In W. K. Camp, E. Diaz, & B. Wawak (Eds.), *Electron Microscopy of Shale Hydrocarbon Reservoirs* (Vol. 102, p. 0). American Association of Petroleum Geologists. https://doi.org/10.1306/13391700M1023581.

Fam, M. A., Dusseault, M. B., & Fooks, J. C. (2003). Drilling in mudrocks: rock behavior issues. *Journal of Petroleum Science and Engineering*, *38*(3), 155–166. https://doi.org/https://doi.org/10.1016/S0920-4105(03)00029-9.

Frazer, D., Abad, M. D., Krumwiede, D., Back, C. A., Khalifa, H. E., Deck, C. P., & Hosemann, P. (2015). Localized mechanical property assessment of SiC/SiC composite materials. *Composites Part A: Applied Science and Manufacturing*, *70*, 93–101. https://doi.org/https://doi.org/10.1016/j.compositesa.2014.11.008.

Gao, Z., & Hu, Q. (2016). Wettability of Mississippian Barnett Shale samples at different depths: Investigations from directional spontaneous imbibition. *AAPG Bulletin*, *100*(1), 101–114. https://doi.org/10.1306/09141514095.

Ghorbal, A., Grisotto, F., Charlier, J., Palacin, S., Goyer, C., Demaille, C., & Ammar, B. B. (2013). Nano-electrochemistry and nano-electrografting with an original combined AFM-SECM. *Nanomaterials*, 3(2), 303–316. https://doi.org/10.3390/nano3020303.

Groen, J. C., Peffer, L. A. A., & Pérez-Ramírez, J. (2003). Pore size determination in modified micro- and mesoporous materials. Pitfalls and limitations in gas adsorption data analysis. *Microporous and Mesoporous Materials*, *60*(1), 1–17. https://doi.org/https://doi.org/10.1016/S1387-1811(03)00339-1.

Guo, H. M., Liu, H. W., Wang, Y. L., Gao, H. J., Gong, Y., Jiang, H. Y., & Wang, W. Q. (2004). Surface structures of dl-valine and l-alanine crystals observed by atomic force microscopy at a molecular resolution. *Surface Science*, *552*(1), 70–76. https://doi.org/https://doi.org/10.1016/j.susc.2003.12.049.

Han, D., Nur, A., & Morgan, D. (1986). Effects of porosity and clay content on wave velocities in sandstones. *Geophysics*, *51*(11), 2093–2107. https://doi.org/10.1190/1.1442062.

Han, J., Zhu, H., Lu, Y., Yang, S., Yang, M., Shi, E., & Qi, Y. (2022). Microstructural Analysis of Organic-Rich Shales: Insights from an Electron Microscopic Study by Application of FIBSEM and TEM. *Nanomaterials*, 12(23), 4135. https://doi.org/10.3390/nano12234135

Handy, L. L. (1960). Determination of effective capillary pressures for porous media from imbibition data. *Transactions of the AIME*, *219*(01), 75–80. https://doi.org/10.2118/1361-G.

Heath, J. E., Dewers, T. A., McPherson, B. J. O. L., Petrusak, R., Chidsey Jr., T. C., Rinehart, A. J., & Mozley, P. S. (2011). Pore networks in continental and marine mudstones: Characteristics and controls on sealing behavior. *Geosphere*, *7*(2), 429–454. https://doi.org/10.1130/GES00619.1.

Hertz, H. (1882). Über die berührung fester elastischer Körper, *Journal für die reine und angewandte Mathematik* 92, pp.156-171. (For English version, see: Hertz, H., 1896. On the contact of elastic solids, In: *Miscellaneous Papers, Chapter V, pp.146-162.* by Hertz, H. and Lenard P., translated by Jones, D. E. and Schott G.A., London: Macmillan.)

Hu, M. Q., Persoff, P., & Wang, J. S. Y. (2001). Laboratory measurement of water imbibition into low-permeability welded tuff. *Journal of Hydrology*, *242*(1), 64–78. https://doi.org/https://doi.org/10.1016/S0022-1694(00)00388-7.

Hu, Q., Ewing, R. P., & Dultz, S. (2012). Low pore connectivity in natural rock. *Journal of Contaminant Hydrology*, *133*, 76–83. https://doi.org/https://doi.org/10.1016/j.jconhyd.2012.03.006.

Hu, Q., Zhang, Y., Meng, X., Li, Z., Xie, Z., & Li, M. (2017). Characterization of micro-nano pore networks in shale oil reservoirs of Paleogene Shahejie Formation in Dongying Sag of Bohai Bay Basin, East China. *Petroleum Exploration and Development*, *44*(5), 720–730. https://doi.org/https://doi.org/10.1016/S1876-3804(17)30083-6.

Huang, J., Cavanaugh, T., & Nur, B. (2013). An Introduction to SEM Operational Principles and Geologic Applications for Shale Hydrocarbon Reservoirs. In W. K. Camp, E. Diaz, & B. Wawak (Eds.), *Electron Microscopy of Shale Hydrocarbon Reservoirs* (Vol. 102, p. 0). American Association of Petroleum Geologists. https://doi.org/10.1306/13391699M1023580.

Hunt, A., Ewing, R., & Ghanbarian, B. (2014). *Percolation Theory for Flow in Porous Media* (3rd ed. 20). Springer International Publishing. https://doi.org/10.1007/978-3-319-03771-4.

Ilgen, A. G., Heath, J. E., Akkutlu, I. Y., Bryndzia, L. T., Cole, D. R., Kharaka, Y. K., Kneafsey,

T. J., Milliken, K. L., Pyrak-Nolte, L. J., & Suarez-Rivera, R. (2017). Shales at all scales: Exploring coupled processes in mudrocks. *Earth-Science Reviews*, *166*, 132–152. https://doi.org/https://doi.org/10.1016/j.earscirev.2016.12.013.

Javadpour, F., Moravvej Farshi, M., & Amrein, M. (2012). Atomic-force microscopy: a new tool for gas-shale characterization. *Journal of Canadian Petroleum Technology, 51*(04), 236-243. https://doi.org/10.2118/161015-PA

Jiao, K., Yao, S., Zhang, K., Hu, W., & Cao, J. (2018). The evolution of nanopores and surface roughness in naturally matured coals in South China: An atomic force microscopy and image processing study. *Fuel*, *234*, 1123–1131. https://doi.org/10.1016/j.fuel.2018.07.102.

Ju, Y., Huang, C., Sun, Y., Wan, Q., Lu, X., Lu, S., He, H., Wang, X., Zou, C., Wu, J., Liu, H., Shao, L., Wu, X., Chao, H., Liu, Q., Qiu, J., Wang, M., Cai, J., Wang, G., & Sun, Y. (2017). Nanogeosciences: Research history, current status, and development trends . *Journal of Nanoscience and Nanotechnology,* 17(9), 5930–5965. Amer Scientific Publishers . https://doi.org/10.1166/jnn.2017.14436.

Ju, Y., Sun, Y., Tan, J., Bu, H., Han, K., Li, X., & Fang, L. (2018). The composition, pore structure characterization and deformation mechanism of coal-bearing shales from tectonically altered coalfields in eastern China. *Fuel*, *234*, 626–642. https://doi.org/https://doi.org/10.1016/j.fuel.2018.06.116.

Khanikaev, A. B., Arju, N., Fan, Z., Purtseladze, D., Lu, F., Lee, J., Sarriugarte, P., Schnell, M., Hillenbrand, R., Belkin, M. A., & Shvets, G. (2016). Experimental demonstration of the microscopic origin of circular dichroism in two-dimensional metamaterials. *Nature Communications*, *7*(1), 12045. https://doi.org/10.1038/ncomms12045.

Khatibi, S., Ostadhassan, M., Tuschel, D., Gentzis, T., Bubach, B., & Carvajal-Ortiz, H. (2018). Raman spectroscopy to study thermal maturity and elastic modulus of kerogen. *International Journal of Coal Geology*, *185*, 103–118. https://doi.org/https://doi.org/10.1016/j.coal.2017.11.008.

Kibria, M. G., Hu, Q., Liu, H., Zhang, Y., & Kang, J. (2018). Pore structure, wettability, and spontaneous imbibition of Woodford Shale, Permian Basin, West Texas. *Marine and Petroleum Geology*, *91*, 735–748. https://doi.org/https://doi.org/10.1016/j.marpetgeo.2018.02.001.

Kim, K., Ji, S. H., Park, B. S., & Yun, J. S. (2018). High surface area flexible zeolite fibers based on a core-shell structure by a polymer surface wet etching process. *Materials & Design*, *158*, 98–105. https://doi.org/https://doi.org/10.1016/j.matdes.2018.08.010.

Kumar, R., Bhargava, K., Choudhury, D. (2017). Correlations of uniaxial compressive strength of rock mass with conventional strength properties through random number generation. *International Journal of Geomechanics*, *17*(2), 6016021. https://doi.org/10.1061/(ASCE)GM.1943-5622.0000716.

Kumar, V., Curtis, M. E., Gupta, N., Sondergeld, C. H., & Rai, C. S. (2012). Estimation of Elastic Properties of Organic Matter in Woodford Shale Through Nanoindentation Measurements. In *SPE Canadian Unconventional Resources Conference* (p. 11). Society of Petroleum Engineers. https://doi.org/10.2118/162778-MS.

Li, C., Ostadhassan, M., Gentzis, T., Kong, L., Carvajal-Ortiz, H., & Bubach, B. (2018a). Nanomechanical characterization of organic matter in the Bakken formation by microscopy-based method. *Marine and Petroleum Geology*, *96*, 128–138.

https://doi.org/https://doi.org/10.1016/j.marpetgeo.2018.05.019.

Li, C., Ostadhassan, M., Guo, S., Gentzis, T., & Kong, L. (2018b). Application of PeakForce tapping mode of atomic force microscope to characterize nanomechanical properties of organic matter of the Bakken Shale. *Fuel*, *233*, 894–910. https://doi.org/https://doi.org/10.1016/j.fuel.2018.06.021.

Li, Chunxiao, Ostadhassan, M., Abarghani, A., Fogden, A., & Kong, L. (2019). Multi-scale evaluation of mechanical properties of the Bakken shale. *Journal of Materials Science*, *54*(3), 2133–2151. https://doi.org/10.1007/s10853-018-2946-4.

Li, J., Yin, J., Zhang, Y., Lu, S., Wang, W., Li, J., Chen, F., & Meng, Y. (2015). A comparison of experimental methods for describing shale pore features — A case study in the Bohai Bay Basin of eastern China. *International Journal of Coal Geology*, *152*, 39–49. https://doi.org/https://doi.org/10.1016/j.coal.2015.10.009.

Li, M., Dang, D., Liu, L., Xi, N., & Wang, Y. (2017). Imaging and force recognition of single molecular behaviors using Atomic Force Microscopy. *Sensors*, 17(11. https://doi.org/10.3390/s17010200.

Li, Q., Zhang, T., Pan, Y., Ciacchi, L. C., Xu, B., & Wei, G. (2016). AFM-based force spectroscopy for bioimaging and biosensing. *RSC Advances*, *6*(16), 12893–12912. https://doi.org/10.1039/C5RA22841G.

Li, Y., Tang, D., Elsworth, D., & Xu, H. (2014). Characterization of coalbed methane reservoirs at multiple length scales: A cross-section from Southeastern Ordos Basin, China. *Energy & Fuels*, *28*(9), 5587–5595. https://doi.org/10.1021/ef500449s.

Li, Y., Tang, D., Xu, H., Meng, Y., & Li, J. (2014). Experimental research on coal permeability:

The roles of effective stress and gas slippage. *Journal of Natural Gas Science and Engineering*, *21*, 481–488. https://doi.org/https://doi.org/10.1016/j.jngse.2014.09.004.

Li, Y., Wang, Z., Pan, Z., Niu, X., Yu, Y., & Meng, S. (2019). Pore structure and its fractal dimensions of transitional shale: A cross-section from east margin of the Ordos Basin, China. *Fuel*, *241*, 417–431. https://doi.org/https://doi.org/10.1016/j.fuel.2018.12.066.

Li, Y., Zhang, C., Tang, D., Gan, Q., Niu, X., Wang, K., & Shen, R. (2017). Coal pore size distributions controlled by the coalification process: An experimental study of coals from the Junggar, Ordos and Qinshui basins in China. *Fuel*, *206*, 352–363. https://doi.org/https://doi.org/10.1016/j.fuel.2017.06.028.

Liu, F., & Borja, R. I. (2013). Extended finite element framework for fault rupture dynamics including bulk plasticity. *International Journal for Numerical and Analytical Methods in Geomechanics*, *37*(18), 3087–3111. https://doi.org/10.1002/nag.2179.

Liu, J., Jiang, X., Huang, X., & Wu, S. (2010). Morphological characterization of super fine pulverized coal particle. Part 2. AFM investigation of single coal particle. *Fuel*, *89*(12), 3884–3891. https://doi.org/https://doi.org/10.1016/j.fuel.2010.07.001.

Liu, K., Ostadhassan, M., & Bubach, B. (2016). Applications of nano-indentation methods to estimate nanoscale mechanical properties of shale reservoir rocks. *Journal of Natural Gas Science and Engineering*, *35*, 1310–1319. https://doi.org/https://doi.org/10.1016/j.jngse.2016.09.068.

Liu, K., Ostadhassan, M., Bubach, B., Dietrich, R., & Rasouli, V. (2018a). Nano-dynamic mechanical analysis (nano-DMA) of creep behavior of shales: Bakken case study. *Journal of Materials Science*, *53*(6), 4417–4432. https://doi.org/10.1007/s10853-017-1821-z.

Liu, K., Ostadhassan, M., & Bubach, B. (2018b). Application of nanoindentation to characterize creep behavior of oil shales. *Journal of Petroleum Science and Engineering*, *167*, 729–736. https://doi.org/https://doi.org/10.1016/j.petrol.2018.04.055.

Liu, Z., Zhang, Z., Choi, S. K., & Lu, Y. (2018). Surface properties and pore structure of antrachite, bituminous coal and lignite. *Energies,* 11(6). https://doi.org/10.3390/en11061502.

Loucks, R. G., Reed, R. M., Ruppel, S. C., & Hammes, U. (2012). Spectrum of pore types and networks in mudrocks and a descriptive classification for matrix-related mudrock pores. *AAPG Bulletin*, *96*(6), 1071–1098. https://doi.org/10.1306/08171111061..

Loucks, R. G., Reed, R. M., Ruppel, S. C., & Jarvie, D. M. (2009). Morphology, genesis, and distribution of nanometer-scale pores in siliceous mudstones of the Mississippian Barnett Shale. *Journal of Sedimentary Research*, *79*(12), 848–861. https://doi.org/10.2110/jsr.2009.092.

Loucks, R., & Reed, R. (2014). Scanning-electron-microscope petrographic evidence for distinguishing organic matter pores associated with depositional organic matter versus migrated organic matter in mudrocks. *GCAGS Journal*, *3*, 51–60.

Lu, A., Kiefer, A., Schmidt, W., & Schüth, F. (2004). Synthesis of polyacrylonitrile-based ordered mesoporous carbon with tunable pore structures. *Chemistry of Materials*, *16*(1), 100–103. https://doi.org/10.1021/cm031095h.

Mavko, G., Mukerji, T., & Dvorkin, J. (2009). *The Rock Physics Handbook: Tools for Seismic Analysis of Porous Media* (2nd ed.). Cambridge University Press. https://doi.org/DOI: 10.1017/CBO9780511626753.

Melnichenko, Y. B. (2016). *Small-Angle Scattering from Confined and Interfacial Fluids:*

Applications to Energy Storage and Environmental Science. Springer International Publishing, Switzerland.

Ogletree, D. F., Carpick, R. W., & Salmeron, M. (1996). Calibration of frictional forces in atomic force microscopy. *Review of Scientific Instruments*, *67*(9), 3298–3306. https://doi.org/10.1063/1.1147411.

Oliver, W. C., & Pharr, G. M. (1992). An improved technique for determining hardness and elastic modulus using load and displacement sensing indentation experiments. *Journal of Materials Research*, *7*(6), 1564–1583. https://doi.org/DOI: 10.1557/JMR.1992.1564.

Oliver, W. C., & Pharr, G. M. (2004). Measurement of hardness and elastic modulus by instrumented indentation: Advances in understanding and refinements to methodology. *Journal of Materials Research*, *19*(1), 3–20. https://doi.org/DOI: 10.1557/jmr.2004.19.1.3.

Ougier-Simonin, A., Renard, F., Boehm, C., & Vidal-Gilbert, S. (2016). Microfracturing and microporosity in shales. *Earth-Science Reviews*, *162*, 198–226. https://doi.org/https://doi.org/10.1016/j.earscirev.2016.09.006.

Qin, N., Zhang, S., Jiang, J., Corder, S. G., Qian, Z., Zhou, Z., Lee, W., Liu, K., Wang, X., Li, X., Shi, Z., Mao, Y., Bechtel, H. A., Martin, M. C., Xia, X., Marelli, B., Kaplan, D. L., Omenetto, F. G., Liu, M., & Tao, T. H. (2016). Nanoscale probing of electron-regulated structural transitions in silk proteins by near-field IR imaging and nano-spectroscopy. *Nature Communications*, *7*(1), 13079. https://doi.org/10.1038/ncomms13079.

Resende, L., & Martin, J. B. (1985). Formulation of Drucker-Prager Cap Model. *Journal of Engineering Mechanics*, *111*(7), 855–881. https://doi.org/10.1061/(ASCE)0733-9399(1985)111:7(855).

Rief, M., Gautel, M., Oesterhelt, F., Fernandez, J. M., & Gaub, H. E. (1997). Reversible unfolding of individual titin immunoglobulin domains by AFM. *Science*, *276*(5315), 1109–1112. https://doi.org/10.1126/science.276.5315.1109.

Schwiedrzik, J., Raghavan, R., Bürki, A., LeNader, V., Wolfram, U., Michler, J., & Zysset, P. (2014). In situ micropillar compression reveals superior strength and ductility but an absence of damage in lamellar bone. *Nature Materials*, *13*(7), 740–747. https://doi.org/10.1038/nmat3959.

Shi, X., Jiang, S., Yang, L., Tang, M., & Xiao, D. (2020). Modeling the viscoelasticity of shale by nanoindentation creep tests. *International Journal of Rock Mechanics and Mining Sciences*, *127*, 104210. https://doi.org/https://doi.org/10.1016/j.ijrmms.2020.104210.

Silin, D., & Kneafsey, T. J. (2012). Shale gas: Nanometer-scale observations and well modelling. *Journal of Canadian Petroleum Technology*, *51*(06), 464–475. https://doi.org/10.2118/149489-PA.

Simmons, G., & Wang, H. (1971). *Single Crystal Elastic Constants and Calculated Aggregate Properties: A Handbook*. M.I.T. Press. https://books.google.com/books?id=bPwtz_JztBEC.

Slim, M., Abedi, S., Bryndzia, L. T., & Ulm, F. J. (2019). Role of organic matter on nanoscale and microscale creep properties of source rocks. *Journal of Engineering Mechanics*, *145*(1), 4018121. https://doi.org/10.1061/(ASCE)EM.1943-7889.0001538.

Sondergeld, C. H., Newsham, K. E., Comisky, J. T., Rice, M. C., & Rai, C. S. (2010). *Petrophysical Considerations in Evaluating and Producing Shale Gas Resources*. https://doi.org/10.2118/131768-MS.

Sone, H., & Zoback, M. D. (2013). Mechanical properties of shale-gas reservoir rocks — Part 1:

Static and dynamic elastic properties and anisotropy. *Geophysics*, *78*(5), D381–D392. https://doi.org/10.1190/geo2013-0050.1.

Tao, S., Zhao, X., Tang, D., Deng, C., Meng, Q., & Cui, Y. (2018). A model for characterizing the continuous distribution of gas storing space in low-rank coals. *Fuel*, *233*, 552–557. https://doi.org/https://doi.org/10.1016/j.fuel.2018.06.085.

Tian, S., Dong, X., Wang, T., Zhang, R., Zhang, P., Sheng, M., Cheng, S., Zhao, H., Fei, L., Street, J., Chen, Y., & Xu, Q. (2018). Surface properties of organic kerogen in continental and marine shale. *Langmuir*, *34*(46), 13882–13887. https://doi.org/10.1021/acs.langmuir.8b03151.

Tian, S., Wang, T., Li, G., Sheng, M., & Zhang, P. (2019). Nanoscale surface properties of organic matter and clay minerals in shale. *Langmuir*, *35*(17), 5711–5718. https://doi.org/10.1021/acs.langmuir.9b00157.

Tian, S., Zhang, P., Sheng, M., Wang, T., Tang, J., & Xiao, L. (2020). Modification of microscopic properties of shale by carbonic acid treatment: Implications for CO_2-based fracturing in shale formations. *Energy & Fuels*, *34*(3), 3458–3466. https://doi.org/10.1021/acs.energyfuels.9b03772.

Ulm, F.-J., & Abousleiman, Y. (2006). The nanogranular nature of shale. *Acta Geotechnica*, *1*(2), 77–88. https://doi.org/10.1007/s11440-006-0009-5.

Ulm, F.-J., Vandamme, M., Bobko, C., Alberto Ortega, J., Tai, K., & Ortiz, C. (2007). Statistical indentation techniques for hydrated nanocomposites: Concrete, bone, and shale. *Journal of the American Ceramic Society*, *90*(9), 2677–2692. https://doi.org/10.1111/j.1551-2916.2007.02012.x.

Vandamme, M., & Ulm, F.-J. (2013). Nanoindentation investigation of creep properties of calcium

silicate hydrates. *Cement and Concrete Research*, *52*, 38–52. https://doi.org/https://doi.org/10.1016/j.cemconres.2013.05.006.

Varenberg, M., Etsion, I., & Halperin, G. (2003). An improved wedge calibration method for lateral force in atomic force microscopy. *Review of Scientific Instruments*, *74*(7), 3362–3367. https://doi.org/10.1063/1.1584082.

Wang, Q.M. 2019. Nano-petrophysics study of Haynesville Shale, East Texas, USA. *Master's Thesis, the University of Texas at Arlington*, 109 pp.

Wang, Q., Zhou, W., Hu, Q., Xu, H., Meendsen, F., Shu, Y., & Qiao, H. (2021). Pore geometry characteristics and fluid–rock interaction in the Haynesville Shale, East Texas, United States. *Energy & Fuels*, *35*(1), 237–250. https://doi.org/10.1021/acs.energyfuels.0c02423.

Wang, Z., Wang, H., & Cates, M. E. (2001). Effective elastic properties of solid clays. *Geophysics*, *66*(2), 428–440. https://doi.org/10.1190/1.1444934.

Webb, P A, Orr, C., & Corporation, M. I. (1997). *Analytical Methods in Fine Particle Technology*. Micromeritics Instrument Corporation. https://books.google.com/books?id=bchQAAAAYAAJ.

Webb, Paul A. (2001). *An introduction to the physical characterization of materials by mercury intrusion porosimetry with emphasis on reduction and presentation of experimental data*. Micromeritics Instrument Corp, Norcross, Georgia.

Wilkinson, T. M., Zargari, S., Prasad, M., & Packard, C. E. (2015). Optimizing nano-dynamic mechanical analysis for high-resolution, elastic modulus mapping in organic-rich shales. *Journal of Materials Science*, *50*(3), 1041–1049. https://doi.org/10.1007/s10853-014-8682-5.

Wu, T., & Firoozabadi, A. (2020a). Mechanical properties and failure envelope of kerogen matrix by molecular dynamics simulations. *The Journal of Physical Chemistry C*, *124*(4), 2289– 2294. https://doi.org/10.1021/acs.jpcc.9b09639.

Wu, T., & Firoozabadi, A. (2020b). Fracture toughness and surface energy density of kerogen by molecular dynamics simulations in tensile failure. *The Journal of Physical Chemistry C*, *124*(29), 15895–15901. https://doi.org/10.1021/acs.jpcc.0c03158.

Yang, J., Hatcherian, J., Hackley, P. C., & Pomerantz, A. E. (2017). Nanoscale geochemical and geomechanical characterization of organic matter in shale. *Nature Communications*, *8*(1), 2179. https://doi.org/10.1038/s41467-017-02254-0.

Zargari, S., Prasad, M., Mba, K. C., & Mattson, E. D. (2013). Organic maturity, elastic properties, and textural characteristics of self resourcing reservoirs. *Geophysics*, *78*(4), D223–D235. https://doi.org/10.1190/geo2012-0431.1.

Zargari, S., Wilkinson, T. M., Packard, C. E., & Prasad, M. (2016). Effect of thermal maturity on elastic properties of kerogen. *Geophysics*, *81*(2), M1–M6. https://doi.org/10.1190/geo2015-0194.1.

Zeng, G., Dirscherl, K., & Garnæs, J. (2018). Toward accurate quantitative elasticity mapping of rigid nanomaterials by atomic force microscopy: Effect of acquisition frequency, loading dorce, and tip geometry. *Nanomaterials*, *8*(8), 616. https://doi.org/10.3390/nano8080616.

Zhang, L., Ju, Y., Hosoi, A., & Fujimoto, A. (2012). Measurement of electrical properties of materials under the oxide layer by microwave-AFM probe. *Microsystem Technologies*, *18*(11), 1917–1922. https://doi.org/10.1007/s00542-012-1512-2.

Zhang, Y., Barber, T. J., Hu, Q., Bleuel, M., & El-Sobky, H. F. (2019). Complementary neutron

scattering, mercury intrusion and SEM imaging approaches to micro- and nano-pore structure characterization of tight rocks: A case study of the Bakken shale. *International Journal of Coal Geology*, *212*, 103252. https://doi.org/https://doi.org/10.1016/j.coal.2019.103252.

Zhao, J., Zhang, D., Wu, T., Tang, H., Xuan, Q., Jiang, Z., & Dai, C. (2019). Multiscale approach for mechanical characterization of rrganic-rich shale and its application. *International Journal of Geomechanics*, *19*(1), 4018180. https://doi.org/10.1061/(ASCE)GM.1943-5622.0001281.

Zhao, S., Li, Y., Wang, Y., Ma, Z., & Huang, X. (2019). Quantitative study on coal and shale pore structure and surface roughness based on atomic force microscopy and image processing. *Fuel*, *244*, 78–90. https://doi.org/https://doi.org/10.1016/j.fuel.2019.02.001.

Zhou, S., Liu, D., Cai, Y., Karpyn, Z., & Yao, Y. (2018). Comparative analysis of nanopore structure and its effect on methane adsorption capacity of Southern Junggar coalfield coals by gas adsorption and FIB-SEM tomography. *Microporous and Mesoporous Materials*, *272*, 117–128. https://doi.org/https://doi.org/10.1016/j.micromeso.2018.06.027.

Zhou, S., Liu, D., Cai, Y., & Yao, Y. (2016). Gas sorption and flow capabilities of lignite, subbituminous and high-volatile bituminous coals in the Southern Junggar Basin, NW China. *Journal of Natural Gas Science and Engineering*, *34*, 6–21. https://doi.org/https://doi.org/10.1016/j.jngse.2016.06.039.

Zhu, H., Ju, Y., Lu, W., Han, K., Qi, Y., Neupane, B., Sun, Y., Cai, J., Xu, T., Huang, C., & Han, Y. (2017). The characteristics and evolution of micro-nano scale pores in shales and coals . *Journal of Nanoscience and Nanotechnology,* 17(9), 6124–6138. American Scientific Publishers. https://doi.org/10.1166/jnn.2017.14529.

Zhu, H., Ju, Y., Qi, Y., Huang, C., & Zhang, L. (2018). Impact of tectonism on pore type and pore structure evolution in organic-rich shale: Implications for gas storage and migration pathways in naturally deformed rocks. *Fuel*, *228*, 272–289. https://doi.org/https://doi.org/10.1016/j.fuel.2018.04.137.